Faculdade de Engenharia da Universidade do Porto

Master's in mechanical engineering

Interface boundary mechanical resistance analysis in FFF multi-material parts

Lucas Manuel Almeida Lopes

Supervisor: Prof. Dr. Fernando Jorge Lino Alves
Co-Supervisor: Prof Dr. Guilherme Barra
Co-Supervisor: Prof Dr. Leonardo Santana

Porto, 2024

(Blank Page)

Abstract

The manufacturing industry has been transformed by FFF (Fused Filament Fabrication), which provides exceptional design flexibility, personalization options, and affordability. While polylactic acid (PLA) and polyacrylonitrile_butadiene_styrene (ABS) remain popular materials, thermoplastic polyurethane (TPU) is favorite for specific applications including sensors, phone cases and medical braces. Additionally, the incorporation of carbonaceous fillers, such as conductive carbon black (CB) in the TPU can increase its electrical conductivity in several orders of magnitude without compromising mechanical performance. Given the use of electronics in day-to-day life the creation of protective structures for EMI (Electromagnetic Interference) has become of the upmost importance. The design of FFF multi-material honeycomb structured parts with conductive and non-conductive polymer multi-layers have been developed in this sense to improve the EMI shielding effectiveness, providing protection via an absorption-reflection mechanism. Optimization of printing parameters is a key factor to produce mechanically sound multi-material parts. In this thesis, the mechanical resistance of the boundary interface layer in multi-material TPU-CB/TPU samples was studied to verify the applicability of this combination for EMI shielding. A preliminary calibration study was executed to achieve a first optimal parametrization for the two filaments. It was seen that the printability of TPU and CB/TPU was subpar, erratic, and unpredictable. The flexibility of the filaments leads to clogging and buckling, particularly when switching the materials in the printer head. Both the materials were also characterized via a FTIR and MEV analysis. The analysis was clear in demonstrating the difference in composition of the specimens and the presence of impurities in both feedstock materials that give color to the filaments. A parametric study was performed to determine the optimal printing configuration based on the print quality and interface strength of multi-material specimens pull-out test specimens. The high surface quality of the printed parts and interface strength were highly correlated between each other and highly dependent on parameters including nozzle temperature, infill speed and bed temperature. Higher nozzle temperatures and lower infill speeds achieved the best results. As a case study, an EMI shielding case was designed with alternate layers of TPU and CB/TPU, with use of the honeycomb pattern. The experimental tests were validated based on the capacity of the case to block external signals (telecommunication frequency bands) directed at a mobile phone positioned in its interior. It was concluded that FFF multi-material parts composed with TPU and CB/TPU have good interface adhesion if the printing configuration is greatly optimized.

Keywords: Boundary Interface, FFF, Multi-material

(Blank Page)

Resumo

A indústria de fabrico foi transformada pelo processo FFF (Fabricação por Filamentos Fundidos), que proporciona flexibilidade de design, opções de personalização e acessibilidade de custos. Embora o ácido polilático (PLA) e o poliacrilonitril_butadieno_estireno (ABS) continuem a ser dos materiais mais populares, o poliuretano termoplastico (TPU) é o preferido para aplicações específicas, como sensores, capas para telemóveis e aparelhos médicos. Além disso, a incorporação de cargas carbonáceas, como o CB (*Carbon Black*) permite aumentar a condutividade elétrica sem comprometer o desempenho mecânico do material. Dada a grande utilização da eletrónica no quotidiano, a criação de estruturas de proteção contra EMI (Interferência Eletromagnética) tornou-se da maior importância. O design das peças estruturadas em favo de mel multimateriais FFF com multicamadas intercaladas de material isolante e condutor foi desenvolvido neste sentido para aumentar a eficiência de blindagem eletromagnética , cuja proteção se dá através de um mecanismo de absorção-reflexão. A parametrização correta de impressão de peças multi-material é imperativa para garantir integridade mecânica. Nesta tese, estudou-se a resistência mecânica da camada de interface em amostras multimateriais de TPU-CB/TPU para verificar a aplicabilidade desta combinação para blindagem EMI. Foi executado um estudo preliminar de calibração para alcançar uma primeira parametrização ideal para os dois filamentos. Verificou-se que a capacidade de impressão de TPU e CB/TPU era abaixo da média, errática e imprevisível. A flexibilidade dos filamentos leva ao entupimento e enrolamento no cabeçote da impressora, principalmente ao realizar a transição entre materias. Ambos os materiais também foram caracterizados por meio de análise FTIR e MEV de segmentos de filamentos. A análise foi clara ao demonstrar a diferença na composição dos provetes e a presença de impurezas em ambas as matérias-primas que dão cor aos filamentos. Foir realizado um estudo paramétrico foi realizado para determinar a configuração de impressão ideal com base na qualidade de impressão e na resistência da interface de amostras de teste de extração de amostras multi-materiais. A elevada qualidade superficial das peças impressas e a resistência da interface estão altamente correlacionadas entre si e muito dependentes de parâmetros como temperatura do bico, velocidade de enchimento e temperatura da cama de impressão. Temperaturas mais altas do bico e velocidades de enchimento mais baixas alcançaram os melhores resultados. Como caso de estudo, foi projetada uma caixa de blindagem EMI com camadas alternadas de TPU e CB/TPU, com uso de uma estrutura em favo. Os testes experimentais foram validados com base na capacidade da caixa bloquear sinais externos (bandas de frequência telecomunicações) direcionados a um telemóvel posicionado no interior da mesma. Concluiu-se que as peças multimateriais FFF compostas por TPU e CB/TPU apresentam boa adesão na interface se a configuração de impressão for adequadamente otimizada.

Palavras-Chave: Boundary Interface, FFF, Multi-material

(Blank Page)

Acknowledgments

Expresso a minha gratidão ao Professor Jorge Lino pela oportunidade de explorar o tema da impressão 3D. A sua disponibilidade, acompanhamento e fornecimento de recursos foram essenciais para o sucesso deste projeto.

Quero expressar um agradecimento muito especial ao Professor Guilherme Barra pelo seu apoio inabalável em todas as fases do processo, aconselhamento valioso e a sua assistência nas atividades relacionadas à minha dissertação. Agradeço também pela motivação contínua que ele me proporcionou para me tornar não apenas um melhor aluno, mas também uma melhor pessoa. A sua companhia e ouvido amigo em todas as nossas conversas foram verdadeiramente apreciados. Muito obrigado por tudo.

Um grande agradecimento ao Dr. Leonardo Santana pela sua orientação fundamental na definição do rumo do projeto, sua assistência constante, boa disposição e contribuição crucial ao longo de todo o processo.

Agradeço a todos os meus colegas do LDPS. À Ana Pais um grande obrigado pela ajuda essencial nas fases iniciais do projeto e a sua preocupação em apoiar aqueles ao seu redor. Ao Nuno, Francisca, Jorge e Telma pelas sugestões e momentos de relaxamento proporcionados.

Expresso a minha gratidão à Dna. Emília Soares do Departamento de Engenharia Mecânica pela sua generosidade em ceder o equipamento necessário para a análise microscópica e pela realização das operações de corte dos bicos. O seu apoio e simpatia foram fundamentais. Agradeço à Dra. Beatriz Graça do Instituto de Ciência e Inovação em Engenharia Mecânica e Engenharia Industrial (INEGI) pelo acompanhamento nos ensaios de FTIR.

(Blank Page)

“Don´t you lock up something
That you wanted to see fly
Hands are for shaking
No, not tying”

Chris Cornell

(Blank Page)

Index

List of Figures

List of Tables

Abbreviations and Symbols

ABS	polyAcrylonitrile Butadiene Styrene
AM	Additive Manufacturing
CAD	Computer Aided Design
CB	Carbon Black
CEMUP	*Centro de Materiais da Universidade do Porto*
CNT	Carbon Nanotubes
CPC	Conductive Polymer Composite
CV	Variation Coeficient
DEMec	*Departamento de Engenharia Mecânica*
EMI	Electromagnetic Interference
FDM	Fused Deposition Molding
FFF	Fused Filament Fabrication
FM	Flexural Modulus
FTIR	Fourier-transform infrared spectroscopy
FEUP	*Faculdade de Engenharia da Universidade do Porto*
GR	Graphene
HMAMs	Honeycomb Microwave Absorbing Materials
INEGI	*Instituto de Ciência e Inovação em Engenharia Mecânica e Engenharia Industrial*
LDPS	*Laboratório de Desenvolvimento de Produtos e Serviços*
PC	Polycarbonate
PCL	Polycaprolactone
PEEK	Poly Ether Ether Ketone
PETG	Polyethylene Glycol Terephthalate
PLA	Polylactic Acid
PP	Polypropylene
PPy	Polypyrrole
PVC	Polyvinyl Chloride

SE	Shielding Effectiveness
SEM	Scanning Eletron Microscopy
TPU	Thermoplastic Polyurethane
UTS	Ultimate Tensile Strength
3D	Three Dimensional

List of Symbols

Tg	Glass Transition Temperature

1. Introduction

Recent advances in Additive Manufacturing have made it possible to incorporate this technology in different stages of the product development process, from creating the prototype to producing the end product. Contrary to material subtracting forms of manufacturing, AM allows for greater complexity and freedom in the design to create novelty solutions for very specific applications in various fields like medicine, automotive, and electronics.

Fused Filament Fabrication (FFF) is a particular process of AM characterized by the relative low cost, easiness of handling and low print times in comparison to the other similar technologies, used generally to produce single or multi-polymeric components. The existence of various “open source” software available for the creation of printable models and the wide range of feedstock material commercially available for FFF have made it very popular for product developers, engineers, and enthusiasts. Polylactic acid (PLA) and polyacrylonitrile_butadiene_styrene (ABS) are common filaments used in FFF, due to their exceptional relationship between printability and physical properties. Commercially available filaments comprising polycarbonate (PC), polycaprolactone (PCL), polyethylene glycol terephthalate (PETG), polypropylene (PP), thermoplastic polyurethane (TPU) and other thermoplastics have also been used to produce components through FFF for several applications.

Recent advances in this area have allowed the use of high-performance polymer filaments, including electrically conductive polymer composites (CPCs). These materials are composed of an insulating polymer matrix, generally in a higher volume fraction, and a dispersed phase of a conductive filler. Due to their extraordinary physical properties, carbon-based conductive fillers such as carbon nanotubes (CNT), conductive carbon black (CB) and graphene (GR) have been incorporated into insulating polymer matrices to produce CPCs filaments. Nowadays, commercially available conductive filaments based on PLA, TPU, ABS and other thermoplastics matrices filled with carbonaceous materials have already been employed to produce functional components for several technological applications, such as mechanical and chemical sensors, electrical circuits, and electromagnetic shielding applications (Kim, 2020).

One of the challenges in developing CPCs products through FFF is to achieve a good balance of their functional properties and printing quality. The presence of defects that arise during FFF generally reduce the mechanical, thermal, magnetic, and electrical properties of the 3D printed products when compared to those manufactured through conventional polymer molding processes. To overcome these drawbacks, research groups have prepared conductive filaments by modifying or using two or more conductive fillers to be incorporated

into an insulating polymer matrix. Optimization of 3D printing parameters, geometric modeling building and multi-material layers products have been also extensively used for manufacturing 3D printed products with improved functional properties.

With the growing presence of electronics in daily life, more and more research has been conducted in the sense of determining the effects that these devices can cause. The waves emitted by these products are known to generate EMI (Electromagnetic Interference), producing harmful effects to other electronics and humans. Therefore, there is a large interest in developing EMI shielding components based on CPCs using FFF. 3D printed multi-material sandwich structures produced by sequencing alternate layers of conductive and non-conductive polymer filaments have been shown to be a good configuration for mechanical integrity and considerable electromagnetic attenuation by absorption-reflection mechanism of the insulating and conductive phase, respectively.

The combination of two filaments with the same polymer matrix and different composition formulation can be applied to these instances. However, when manufacturing with two different feedstock filaments using a single head extruder, the interface boundary created by the deposition of both materials layers is a critical aspect which has shown to largely affect the properties of the component. Although some studies have already demonstrated the potential use of FFF to produce multilayered structures for EMI shielding application, to the best of the authors´ knowledge, none of them have investigated the influence of the printing parameters on the adhesion between the different polymer layers and physical properties of the printed product. The optimization of pattern combinations can produce 3D printed parts with good quality to prevent a decrease in mechanical, electrical, and electromagnetic properties of the 3D printed sample (Schmitz et al., 2018)(Schmitz et al., 2023).

In light of the current state of research in this theme, the aim of this thesis was to investigate the influence of printing parameters on the geometrical boundary interface and mechanical adhesion of different polymer layers of 3D printed multi-material parts produced by FFF. For this purpose, commercial filaments based on neat TPU and TPU filled with conductive filler were chosen to produce 3D printed parts by FFF due to their mechanical properties, oil chemical resistance, abrasion resistance, electrical properties and highly elastic flexibility which allows its use in different technological applications. Furthermore, the possibility of producing sandwich structures through multi-material printing of honeycomb patterned layers of conductive and non-conductive TPU is explored for microwave absorption performance enhancement.

1.1 Objectives

1.1.1 Main Objectives

The purpose of the work is to analyze the mechanical adhesion between layers of multi-material FFF printed parts, more specifically between layers of natural TPU and CB/TPU by varying the printing parameters and performing mechanical peeling tests.

1.1.2 Specific Objectives

The specific objectives of the dissertation can be detailed as such:

- Calibration of a Prusa i3 MK3 FFF 3D printer.
- Calibration of the printing parameters for TPU and TPU/CB filaments via fabrication of cubic parts and further validation trough dimensional and mass measurement analysis.
- Parametric study of printing parameters on boundary interface adhesion by fabrication of samples with varying the parametrization.
- Performing a visual and mechanical evaluation of the samples and comparing the results to the ones of samples printed in the defined standard via a statistical analysis.
- Analyzing the microstructure of calibration cubes and samples with extreme parametrization via optical and electronic microscopy.
- Analyzing the relationship between the inner surface damage of used nozzles and the printing quality of the samples.
- Printing of honeycomb multi-material structures composed of TPU and TPU/CB.

2. State of the Art

Additive Manufacturing technologies are good options compared with the traditionally employed processing techniques since its advantages include easy design changes without building new molds and the ability to build complex and customizable structures (Schmitz et al., 2023).

Amongst the various 3D printing technologies, Material Extrusion of Fused Filament Fabrication (FFF) was initially developed by Scott Crump and patented as FDM (Fused Deposition Modeling). A considerable advantage of FFF is its relatively overall cost, a variety of easy to use commercial filament and the available and straightforward open-source software's to design and control the manufacturing. For these reasons, FFF is one of the most popular and affordable 3D printing techniques in academia, industry, and enthusiasts, providing a lot of development in the matter given the high interest (Schmitz et al., 2023) (Schmitz et al., 2018) (Manganiello et al., 2019).

FFF is an easily adjustable way of processing thermoplastics to produce low porosity parts, crucial in producing structural components. It is known to have, however, poor surface quality and roughness compared to compression and injection molding. This can be attenuated by using different nozzle diameters and layer heights to produce thinner and more accurate features. This results in a trade-off between optimal mechanical and dimensional characteristics and production feasibility, resulting in longer print times. (Bates et al., 2016).

FFF technique involves the filament being driven to the extrusion nozzle, passing through a heating block to reach the required melting temperature. The stable pressure and constant moving speed of the filament through the nozzle results in a uniform extrusion of the filament that bonds to the below bed of already deposited material, becoming solid again by cooling, as shown in Figure 1 (Abilgaziyev et al., n.d.).

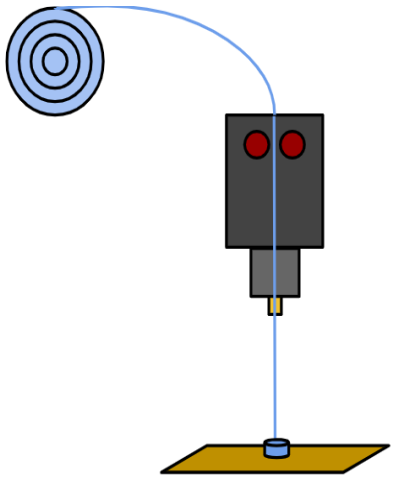

Figure 1 - Illustrative scheme of the FFF 3D printer.

The nozzle (Figure 2), typically made of brass, is coupled to the heating block, usually made of aluminum. A thermistor is fixed inside this heated block to measure its temperature and provides regulatory feedback to keep the temperature of the hot end in a suitable working range (Krishnanand et al., 2020).

Figure 2 - Brass nozzle for FFF printer.

FFF printers' extrusion heads are composed of various components with the goal of driving, heating, and extruding the material filament, as illustrated in Figure 3. The extrusion head can be segmented into the cold and the hot end. The former is connected to the latter and has two purposes, first to block the heat transfer from the hot end to the upper part of the extruder and, second to maintain the sufficient distance between pre-heated filament and molten filament, restricting the former to the heating block only. The cold end incorporates fins, the cooling fan and the extrusion driver, the mechanism responsible for conducting the filament to the hot end via gears or splines actuated by a stepper motor capable of precise and controlled rotation of the shaft (Krishnanand et al., 2020).

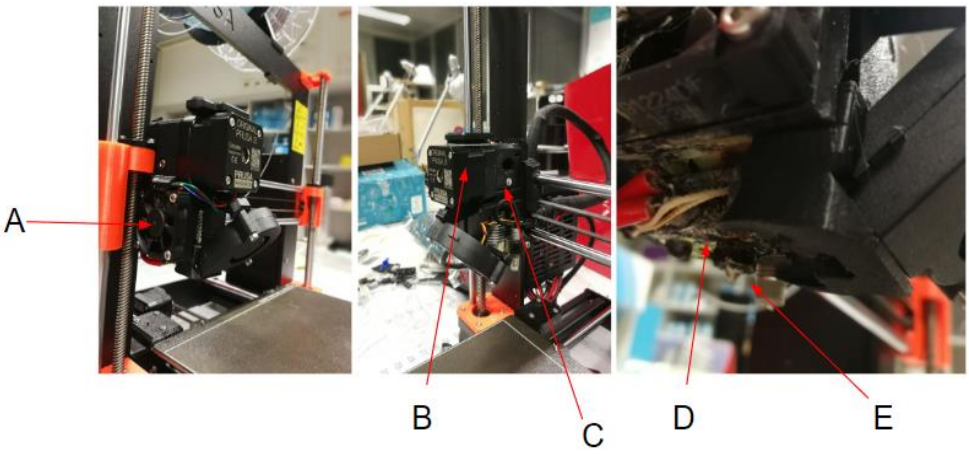

Figure 3 - Some extrusion components: A - Fan; B - Stepper motor; C - Gears; D - Heating block; E - Nozzle.

Mainly thermoplastics such as PLA and ABS are used in this technology since their properties provide good quality of the printed parts. Other materials including thermoplastic elastomers, such as TPU, can be used to print parts with specific desired properties, although the use of these materials add a degree of difficulty to the printing process. The overall surface

finish and dimensional accuracy of FFF parts is not as good as for other 3D technologies (Krishnanand et al., 2020).

Some reasons for printing and poor quality in FFF printed parts can be uncovered by analyzing the inherent characteristics of FFF. For example, temperature derivative warps appear since there is a high enough temperature gradient between the deposited material and the printer bed. The printing configuration must be optimized by having the best possible relation between the extrusion temperature and the hot bed temperature. This is something that can vary from the structure and properties of the material and even the geometry of the part. This, however, does not apply only to temperature related defects. A great effort has been made to optimize the printing parameters in order to improve quality and physical properties of printed parts (Krishnanand et al., 2020).

3D printing in general and FFF leaves parts with voids and porosity, which are large contributors to the mechanical anisotropy and geometry errors in printed products. According to Lin et al. (2020) 3D printed products exhibited as much as up to 73 % in strength compared to injection and compression molding counterparts.

2.1 FFF Polymeric Parts

Mechanical properties of FFF printed parts are largely dependent on the thermal mechanisms during the printing process. The polymer is heated up to melting temperatures and then deposited when the crystallization phase occurs, followed by a glass transition phase in which the material goes from elastic to brittle and then final shrinkage from cooldown to room temperature. Similar to what is known about injection and compression molding of polymers, where temperature can change the micro-morphology in crystallization by crosslinking, FFF printed polymers are very sensitive to this parameter as well, i.e., to nozzle and bed temperature. Extrusion velocity and layer height are also key parameters in FFF printed polymeric parts (Kechagias et al., 2021) (Lin et al., 2020)(Gumus et al., 2022a).

Research has been conducted on the mechanical and tribological properties of FFF printed polymer parts summarizing findings in the available literature regarding the optimization of printing parameters to ensure that the performance of these components is up to standard. Nordin Mohamad Norani et al. (2021) report interesting results regarding the 3D printing using thermoplastics polymers:

- An ABS blend specimen with YXZ orientation and 0 ° raster angle (Figure 4) had highest fracture strain and ultimate strength when compared with XYZ, YXZ, XZY, ZXY configurations and 0°, 45°/45°, 45° and 90° raster angles (**FFF**) (Balderrama-Armendariz et al., 2018);

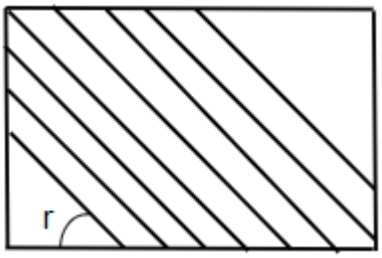

Figure 4 - Raster angle - r.

- PEEK specimens were reported to have "optimal tensile properties at a printing speed of 60 mm/s, layer thickness of 0.2 mm, temperature of 370°C and filling ratio of 40%", with tensile strength of 40 MPa, Young's modulus of 522.9 MPa, and elongation at 14.3% (**FFF**) (X. Deng et al., 2018);

- Epoxy resin blended with graphite/talc micro fillers for 15 minutes at a constant speed of 1200 rpm and an applied load of 100 N demonstrated a significant reduction by ~63% (0.103 to 0.276) in the friction coefficient (COF) and a 34% increment in wear resistance in comparison to pure epoxy bearing balls under dry conditions (Rathaur et al., 2020)**;**

- Using uniaxial and oblique impact configurations to test the response of PU and epoxy it was seen that at a high strain rate, the COF of both polymers was inversely proportional to pressure. For PU and epoxy, respectively, values of 0.11 and 0.26 under maximum pressure (Sable et al., 2020)**.**

Nordin Mohamad Norani et al. (2021) concluded that a minimum layer thickness, zero orientation, maximum raster angle and width, and negative air gap provide the highest mechanical strength. The polymer's own high strength will then be invaluable if low adhesion, plastic deformation, buckling, and weak inter-layering occur. Although 3D-printed polymers have anisotropic porosity behaviors, their elastic behavior is superior to their absorption capacity.

Furthermore, in terms of tribological properties, under specific sliding conditions, 3D-printed polymers exhibit low friction and wear because of increased contact area, plastic deformation, and breaks in asperities. Further research also shows that relatively high nozzle temperatures and lower printing speeds are optimal for printing PLA and ABS (Nordin Mohamad Norani et al., 2021) (Gumus et al., 2022a) (Lin et al., 2020)**.**

Many works reported in the literature demonstrated that printing parameters such as the build orientation, raster angle, and layer thickness are the most important and critical parameters regarding to mechanical properties of FFF-processed polymer materials. On the other hand, the extruder temperature and printing speed are among the settings that are more dependent on the filament type. Pratama et al. (2021) have also observed significant influence of the raster angle, raster width, layer thickness, the infill percentage, extrusion temperature and build orientation on the strength of FFF-processed PLA and flexural strength (FS) of FFF-processed ABS. The authors also referenced bibliography reporting that the combination of crisscross (45°/-45°) raster angle and negative air gap (
Figure 5) resulted in a printed ABS with a higher UTS than that with the unidirectional raster angle. According to the authors a horizontal build orientation should be applied during the printing process to have the highest compressive strength value for FFF printed ABS.

Lin et al. (2020) have also demonstrated the great influence of the printing parameters on the properties of the FFF printed parts.

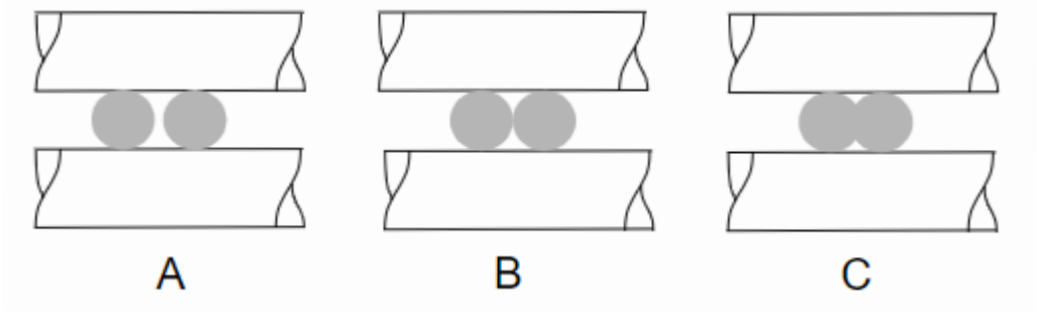

Figure 5 - Types of air gap: A - Positive air gap; B - Neutral air gap; C - Negative air gap.”

2.1.1 Reinforcement Strategies for FFF parts

Instead of new technological solutions to overcome FFF limitations or the parameters optimization, post-processing can improve the quality of the printed components. Pratama et al. (2021) reported a brief overview of some strategies to improve the mechanical properties of 3D printed polymer composite parts. Table 1 summarizes the effect of different reinforcement methods on the mechanical properties of polymer composite parts manufactured by FFF.

Table 1 - Reinforcement processes applicable to FFF.

Name	Processing Method	Results achieved
SFR (short fiber reinforcement).	The filaments are produced through a blend of polymer and short fibers, such as carbons fibers, glass fibers and graphene, prior to the extrusion and a refining process.	● Able to increase the mechanical properties such as the ultimate strength (UTS) of the composite: reported increase (UTS) of **85%** in FFF-processed ABS reinforced by short carbon fiber. ● Can deteriorate the strength in specific cases: material embrittlement in FFF-processed ABS/PA6 because of glass fiber addition, as indicated by the **decreased** value of the material elongation-at-break from **220 to 10%.**
CFR (continuous fiber reinforcement).	The fiber is added during the printing process. The blend occurs in the extrusion head when the two distinct pathways for the polymer and fiber meet near the nozzle, often conical. Carbon, flax, glass, and Kevlar fibers are common in this application.	● Increase of UTS and elastic modulus of FFF-processed PLA by **435% and 599%,** respectively, by the addition of carbon fibers via this process. Studies show also that UTS of PLA with CFR **increases with fiber content**, for instance. ● One disadvantage of CFR is the occurrence of fiber breakage due to the curved "U" geometry of the inlet where the fiber passes through, that **prohibits the use of a negative air gap**, usually a **wanted** parameter definition to produce **good results**.

PAR (powder addition reinforcement).	Consists in the addition of powder particles to the polymer matrix in the extrusion process, to produce a filament that is already reinforced prior to printing. The variance in results can be attributed to defects such as gaps and voids present due to uneven distribution of the powders in the matrix and nozzle clogging. Overall, similar to the SFR method, appropriate choice of base material, filler and filler concentration is crucial since results are not all positive.	● **Positive**: increase in tensile and flexural strength in ABS/PA6 and ABS parts. ● **Negative:** overall embrittlement of some specimens.
VA-FFF (Vibration-Assisted FFF)	Consists in the introduction of a vibrating-extrusion head or nozzle. This would make sure of a more even distribution of the material, reduce porosities, and improve the mechanical properties of the final product. The limited studies done on this subject and the so far described limitations have made this method not widely used.	● Positive results include the reduction in the total porosity of short carbon fiber-reinforced ABS (SCFR-ABS) parts **from 13 to 10%**, and the improvement of its fracture strength, tensile strength, and strain-at-break **by >10%** in this material. ● Distortion of part dimensions and the rougher or wavy surfaces of printed parts are reported.
Annealing heat treatment	Annealing heat treatment has also been used as a possible solution to the problem of non-uniform cooling rates in the printed part. This treatment would allow a better bond quality of the printed material, reduce porosity, and therefore improve the mechanical properties. Despite its simplicity and low-cost operation, requiring only basically the use of an oven, studies on the matter show again conflicting results.	● Reported increase in tensile strength of FFF-processed PLA by **5%** once annealed at **160 °C for 30 s**. ● Reported **decrease** in the PLA's strength when annealing with temperatures from **60 to 120 °C for 30 to 120 min**. The recrystallization process in annealing can also **cause residual stresses** since the parts tend to bend.

The addition of fibers in various stages of the process has a great influence on the mechanical properties of the printed parts, although the effects are not always beneficial, depending on the materials and processing parameters used (Pratama et al., 2021).

2.1.2 Thermoplastic Polyurethane (TPU) in FFF

TPU is one of the most used 3D printing materials for making flexible parts. The elastomeric behavior of TPU is assigned to its chemical structure composed of soft polyester/polyether segments and isocyanate chains, as observed in Figure 6. TPU is highly regarded as a good solution for various recent applications in the field of engineering products manufactured by extrusion processes. For instance, using FFF to obtain TPU elastic and energy absorbent parts is appealing since the material is inherently flexible and has excellent impact and abrasion resistance properties. TPU is also used in many other technological applications, including in hospital beds, gel shoe orthotics, wearable monitor devices, bonded magnets, multi-axis force sensors, and heat capacitor. The viscoelastic properties of TPU allow for a deformation recovery under cyclical loading-unloading compression or tensile conditions, that make it suitable for these applications (Bruère et al., 2023)(Gumus et al., 2022a) (Nace et al., 2021) (Bates et al., 2016) (Bates et al., 2019) (Kechagias et al., 2021) (Lin et al., 2020).

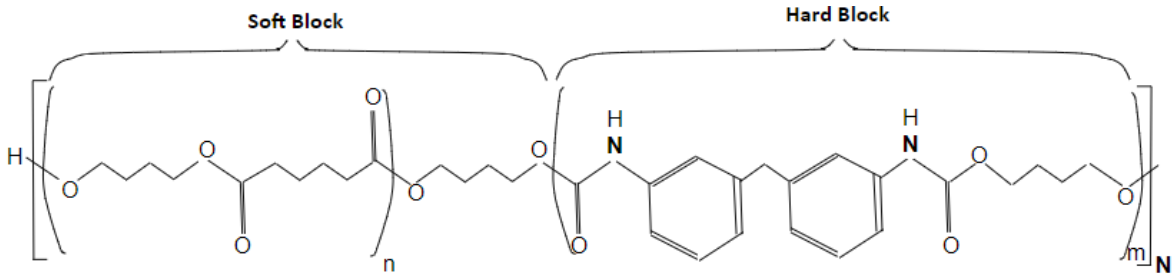

Figure 6 - Chemical structure of a TPU ester-based repeat unit.

TPU has been considered, for instance, as a possible replacement for viscoelastic polyurethane foams (**VPFs**), Figure 7, used in various comfort cushioning applications such as hospital or long-term care beds, wheelchair seating, office furniture, shoe sole inserts and aircraft and vehicle seating. They are able to conform to various shapes under loading conditions, which makes them suitable for human comfort applications (Nace et al., 2021).

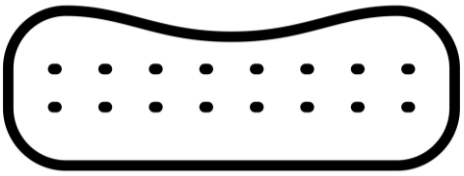

Figure 7 - Viscoelastic foam illustration.

When designing electronic components, 3D printed conductive polymer composites (**CPC's**) have the advantages of ease of shaping, low density, a wide range of electrical conductivity, and corrosion resistance. TPU displays a good affinity with fillers such as carbonaceous and metallic. Due to its functional properties, such as higher sensitivity and adjustable electrical properties, composites based on TPU, and conductive fillers can be used as electromechanical sensors. The four most common carbonaceous materials incorporated into TPU to create a flexible conductive material are as 0D, 1D, 2D, and 3D materials, conductive carbon black (CB), carbon nanotubes (CNT), graphene nanoplates (GNP), and branched carbon nanotubes to construct point-to-point, end-to-end, plane-to-plane, and three-dimensional conductive networks in the TPU matrix, respectively. The carbon black disperses well in the TPU matrix to form a robust, point-to-point conductive network, highly stretchable and sensitive, optimum for sensor applications. The addition of a conductive filler to the insulating matrix such as CB into the TPU matrix, provides adjustable electrical conductivity values, maintaining its softness, biocompatibility, and flexibility, applicable for example for knee joint prosthetics, as illustrated in Figure 8 (Kim, 2020) (Chen et al., 2021).

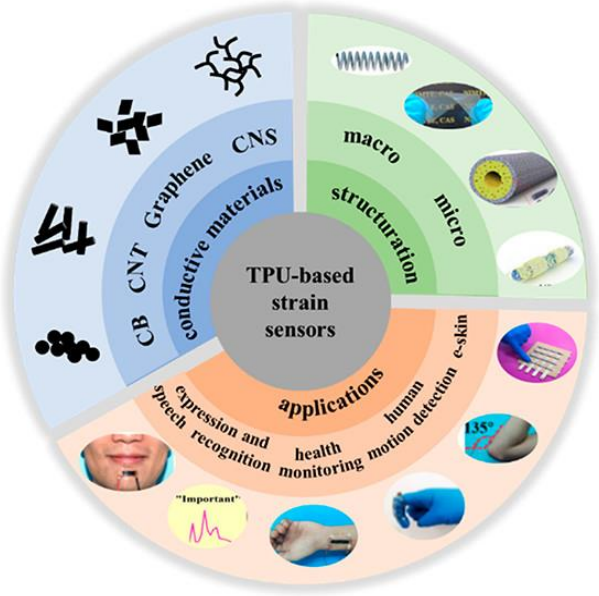

Figure 8 - TPU-based strain sensors diagram (Chen et al., 2021).

Kim (2020) reported that conductive TPU composites can be used for producing flexible 3D-printed electronic devices as single structures in a straightforward method. The authors have also demonstrated that for CB/TPU composites, the percolation threshold is in the range of 8–10 wt. % of carbon fillers.

The working mechanism in a piezoresistive sensor, one application for CB/TPU, involves a minimal electrical conductivity when the sensor is unloading, where the conductive particles are scattered in the insulating matrix. As a compressive force is applied, the flexible matrix will deform and the electrical conductivity will increase due to the coming together of the conductive particles, the tunneling resistance mechanism. During cyclic loading, hysteresis curves can be observed due to the polymer viscoelasticity and interaction of the insulating matrix and conductive filler. The article reported that, while limited to well defined conductive filler concentration (composites with 6 wt. % of CB-PPy, for instance), FFF is indeed a promising fabrication method for flexible composites with good piezoresistive responses (Bertolini, Dul, Lopes Pereira, et al., 2021).

Despite the interest of this material as a candidate for the applications mentioned above, few research works have been conducted either regarding the mechanical characterization of TPU products produced by FFF, especially on the effects of interlayer and raster bonding, and between multi-material interlayer and raster bonding for special tailored technologies (Arifvianto et al., n.d.) (Lin et al., 2020).

When it comes to the printing process itself, the use of TPU is challenging. This filament tends to buckle and therefore makes extrusion irregular, and its control is very poor. Moisture is also an issue. Its sensitivity to it can even lead to printing stoppage due to the filament's previous exposure to it. A controlled and dry environment is therefore recommended to ensure the maintenance of the filament quality and good printing results (Bruère et al., 2023). Other research also found that manufacturing with TPU with CB as a filler is even more challenging in terms of repeatability. The filler content makes the TPU more brittle and disturbs the deposition of the strands, making it more irregular and discontinuous, compromising the overall properties and quality of the part. The percentage of filler used must be also chosen according to the desired mechanical properties, which again presents a compromise in the design of these components (Manganiello et al., 2019) (Kim, 2020).

2.1.2.1 TPU Part Properties and Parametrization

Expanding on the research available in the literature regarding the optimization of printing parameters for TPU parts' mechanical integrity, Nace et al. (2021) investigated the use of TPU to produce VPF's (Viscoelastic polyurethane foams). The authors produced 3D printed parts of TPU with different infill patterns, 2D and 3D, and observed an increase in stiffness and strength by the increase in the infill percentage. Promising results have been

observed especially for the use of load bearing flexible structures applications, for example with TPU 3D printed at 20% infill in a concentric pattern presenting a compression behavior close to VPFs (Figure 9). 3D printed parts produced at 215 °C and raster angle of 45° exhibits higher strength and toughness.

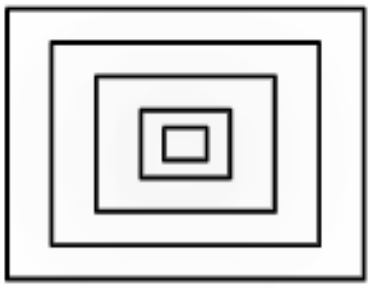

Figure 9 - Concentric infill pattern with ~20% density scheme.

Some studies highlighted the importance of air gap rather than raster angle and printing temperature on the tensile strength of TPU 3D printed parts (Arifvianto et al., n.d.)(Xiao & Gao, 2017) (Hohimer et al., 2017).

Arifvianto et al. (n.d.) have also investigated the influence of raster orientation, at temperatures from 190 °C to 230 °C on the tensile properties of 3D printed TPU parts. The best printing parameters to improve the mechanical properties were extrusion temperature of 200 °C and 0 ° raster angle unidirectional configuration.

Lin et al. (2020) studied the tensile and delamination strength between two adjacent beads (raster or strand) based on three laydown patterns in TPU samples. Lower nozzle height increases packing density and reduces internal voids of printed parts, enhancing tensile properties. According to the authors this behavior is attributed to the squeezing effect which promotes more molecular diffusion and increases bonding strength, as illustrated in Figure 10. A higher nozzle height will cause deterioration of the deposited bead shape and therefore less bonding effectiveness.

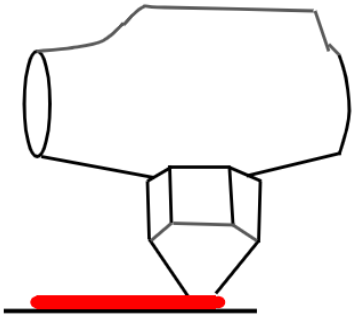

Figure 10 - Squeezing effect provided by lower nozzle height.

Rodríguez et al. (2021) performed a study to determine optimum configuration of printing parameters on TPU FilaFlex 82A by producing cubes and analyzing their visual aspect. It was reported that 0,1 mm layer height, 240 °C extrusion temperature, 20 mm/s extrusion speed and 100% fluidity are recommended to obtain good results.

Bruère et al. (2023) also executed a parametric study on 3D printed parts of TPU manufactured by FFF and reported that the alternation in infill orientation helps to keep the integrity of the print when analyzing tensile properties in contourless (without perimeter) specimens (Figure 11). It was observed that the addition of the contour to the samples decreased the influence of the infill orientation on the tensile strength of the specimens, reporting that this change improved the integrity of the structure and reduced delamination.

Figure 11 - A - Part with perimeter; B - Part without perimeter.

Considering what is known in the literature regarding the great dependence of FFF parts' quality on the parameters above mentioned, Gumus et al. (2022) have also observed an enhancement of the tensile properties with increasing nozzle temperatures (up to 255 °C). The authors attributed this behavior to dimensional accuracy, and higher infill percentages.

Desai et al. (2023) published a bibliography review, in which they state that the print's interlayer adhesion can be increased by lowering the printing speed and raising the printing temperature. Furthermore, increasing the infill density also could increase TPU print's compressive strength. Despite this it is reported that TPU has weak layer adhesion, possibly causing delamination where the layers separate, as illustrated in Figure 12.

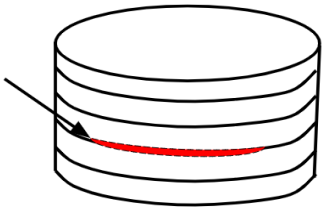

Figure 12 - Delamination between layers of a FFF part.

Considering dimensional accuracy, very important for medical and engineering applications, studies point to the feedstock material being the most critical parameter, followed by the layer thickness, with the latter being the most responsible for surface roughness. Garg et al. (2022) analyzed layer height, infill density and printing speed to determine their effects on dimensional accuracy, through an ANOVA method. They reported that layer height of 0,2 mm, infill density of 70%, and printing speed of 10 mm/s achieved good dimensional accuracy, and that layer height is the most important factor to the roughness. A layer height of 0,1 mm is recommended.

2.2 Multi-Material FFF

Different setups of FFF printers can be useful for tailored applications to improve process efficiency and add design possibilities.

The printing of multi-material components presents a technological challenge regarding FFF. Multi-material printing involves the printing of different filaments and materials successively to form a uniquely diverse product. The simultaneous use of color and material in typical printers is an impossibility, only reserved for multi-extruder head printers, printers that use a multi-colored filament, or previously blended filaments. In multi-material printing on a conventional FFF printer there is a necessary stoppage in the process in order to change the filament. This can negatively affect not only the quality of the printed part but characteristics like the interlayer adhesion, or the overall mechanical performance of the final product (Abilgaziyev et al., n.d.). Figure 13 shows some examples of multi-material parts of PLA manufactured by FFF.

Figure 13 - Multi-material parts manufactured by *Laboratório de Desenvolvimento de Produtos e Serviços* at *FEUP*.

Furthermore, the design and slicing of the part in the printing software must be done consciously since the division of the part in sections of different filaments is done only in the “z” axis, i.e., the extruding direction. This means that typical FFF components only present

variability in material and color between stacking planes of deposited material, never in the same plane. For this reason, novelty solutions have been studied to overcome this problem like the development of multi-nozzles printers that can be programmed to act simultaneously (Abilgaziyev et al., n.d.).

Multi-extruder models that can print more than three colors simultaneously already exist and are possible solutions for improving processability of multi-material parts. There is mention in the literature of a computationally verified preliminary design for what could be a possible future solution, able to print up to five different colors and materials at the same time, developed by Abilgaziyev et al. (n.d.). The configuration proposed has the hot-end extruder being driven by two stepper motors, which significantly reduces the bulkiness and weight of the hot-end and increases the printing speed, to separate the driving parts and assure the main weight is located at the fixed cold-end.

2.2.1 Multi-Material TPU-Based Parts

A lot of recent and state-of-the-art solutions for technological applications have been created through the application of multi-material configurations via printing FFF parts with various feedstock filaments. In terms of mechanical properties in multi-material specimens, while the printing parameters have a great impact for typical FFF parts, research regarding the bonding adhesion between layers of different materials is required. Manufacturing with diferent materials has limitations regarding the different physical properties of the materials, that affect mechanical integrity, and overall predictability when it comes to the final part's properties, functionality, and process repeatability (Brancewicz-Steinmetz et al., 2021) (Arifvianto et al., 2022) (de León et al., 2019) (Lopes et al., 2018).

One of the challenges that affects this growing field of exploration is the lack of consensus on how to perform evaluation of defining characteristics, such as interlayer bonding and adhesion in FFF. The high anisotropy derived from the printing layout of 3D printed samples requires use of nonstandard and one-time developed tests with different geometries and tools to assess the adhesion between layers and rasters. As stated before, TPU can be combined with numerous polymers and fillers to create novelty and tailored solutions for various products. de León et al. (2019) have demonstrated that the production of TPU/ABS blends, for instance, offered good interlayer adhesion and mechanical properties. In this case, however, only one filament is used in the printing process, made from the blend, which facilitates the overall processing and structural integrity.

More interestingly however, is the production of multi-material parts based on two feedstock filaments. Their adhesion can be studied by the printing parametrization or a via the macroscopic interlocking interface design. Considering also mechanical interlocking mechanisms to improve interface bonding in multi-material parts, a study conducted by

Ermolai et al. (2022) showed that for the PLA/TPU coupling, a T shape interface region (Figure 14) shows better results in terms of enhancing mechanical properties of the part when compared with other configurations.

Figure 14 - T-shape interface in a test specimen.

PLA/TPU combination is therefore of great interest, for instance, in the medicine field, to create a component that is functionally versatile. The PLA is added with TPU to increase its flexibility, wear resistance, and overall toughness, arriving at a compromise that provides better elastic modulus than just TPU and better tensile strain than neat PLA providing a solution for tailored applications (Brancewicz-Steinmetz et al., 2021) (Arifvianto et al., 2022).

The interface boundary between the layers of different materials is arguably the most important element in the processing of these components. Although some research has been done about interlayer adhesion of parts made by multi-material of TPU/PLA and TPU/ABS, etc., the analysis of bonding strength of layers produced by deposition of two different melted feedstock filaments, considering the time needed to replace the filaments in the extrusion head, is of interest. Figure 15 illustrates the stoppage time in multi-material printing. In this case, the properties of the materials and the printing parameters are more decisive to the end result. Also, the order in which the materials are printed is key in the production of multi-material parts (Brancewicz-Steinmetz et al., 2021) (Lopes et al., 2018).

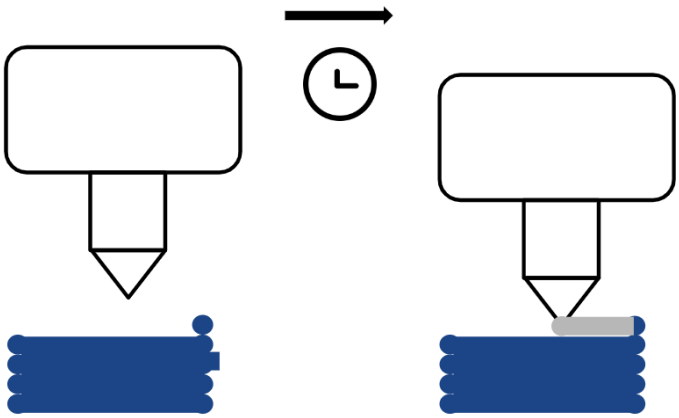

Figure 15 - Stoppage time in multi-material printing.

Lopes et al. (2018) described the influence of the interface boundary as having a severe negative effect on the mechanical performance of the part. The authors have highlighted a crucial factor related to the interruption to change filaments, which is the increased likelihood of the polymer drooling, as observed in polymer extrusion. This can have a detrimental impact on the consistency of the deposition process as the polymer stays longer in the nozzle during the pause, not regulated by the deposition rate as it typically would be in a continuous printing process. To mitigate this, it is necessary to adjust the retraction parameter during this phase of the process or avoid using the highest extrusion temperatures.

Brancewicz-Steinmetz et al. (2021) evaluated the adhesion of the multi-material parts via shear tests, as represented in Figure 16. The authors reported a great influence of printing order and surface pattern in adhesion strength, as well as the TPU plasticity in the results regarding shear strength and displacement of the samples. Shear strength and displacement increased in the TPU/PLA samples compared to the reversed samples. TPU isolated samples also showed lower surface roughness with no direct impact on adhesion. It was noted that printing on TPU is more stable and predictable than printing on PLA. This particular study, however, was not in alignment with other research reviewed by the authors that state that printing the TPU first produces a decrease in bonding strength. This suggests, again, that other printing parameters greatly affect the outcome of the work. Therefore, there should be special interest in their optimization to validate any interlayer bonding experiments.

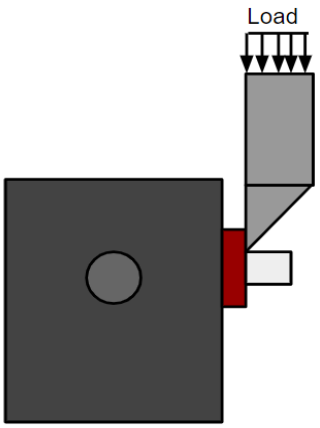

Figure 16 - Shear test for inter-layer bonding evaluation performed.

Arifvianto et al. (2022) derived similar conclusions from their work, stating that tensile strength and elastic modulus of the sandwich-structured PLA/TPU multi-material increased, while the fracture analysis pointed to a low compatibility between the two materials.

Furthermore, the formulation of the material can also impact the final part quality since, for example, the different thermal behavior of the materials can lead to distortions of the part when cooling, creating voids and poor dimensional accuracy. This means the selection of the materials to combine must also be appropriate. To sum up, the chemical compatibility of the materials is a must. A lack in chemical compatibility coupled with different physical properties, and the inherent challenges of the FFF multi-material printing can create a weak interface boundary (Lopes et al., 2018).

Lopes et al. (2018) analyzed the effect of the boundary interface in neat and zebra-crossing-like specimens for the same material and multi-material configurations (PLA, TPU and PET) (Figure 17). For neat material samples, the Young´s Modulus and tensile strength decreased in all cases except for TPU/TPU where there is no visible difference in the Young´s modulus in spite of a clear one observed in the tensile strength. For multi-material specimens the decrease was bigger, adding the chemical effect to the geometrical boundary effect.

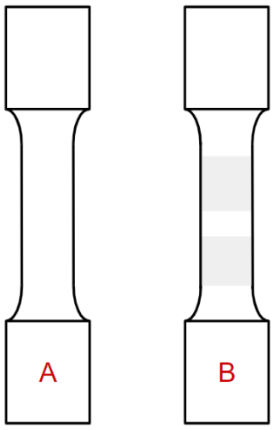

Figure 17 - Test specimens used: A - Neat specimen; B - Zebra crossing-like specimen.

2.3 Design of FFF Parts for EMI Shielding

Electromagnetic (EM) emission and interference between electronic sophisticated devices negatively affects them, in addition to causing harm to human health. Extensive research has been performed to design electromagnetic interference (EMI) shielding and microwave absorbing materials with a broadband EM energy absorbing capability. The magnitude of this issue is such that directives have been issued to regulate this matter (Schmitz et al., 2023) (Ecco et al., 2018).

The most common materials to be used as shielding were metals, due to their high electrical properties. However, besides having high density and being susceptible to corrosion, the shielding mechanism of metals is based on reflection (Figure 18), causing a second EM pollution that also disturbs the operation of other electronic devices. Electrically conductive polymer composites are a good alternative because of their lower density, low cost, ease of processing, and absorption dominated shielding mechanism (Schmitz et al., 2023) (Schmitz et al., 2021).

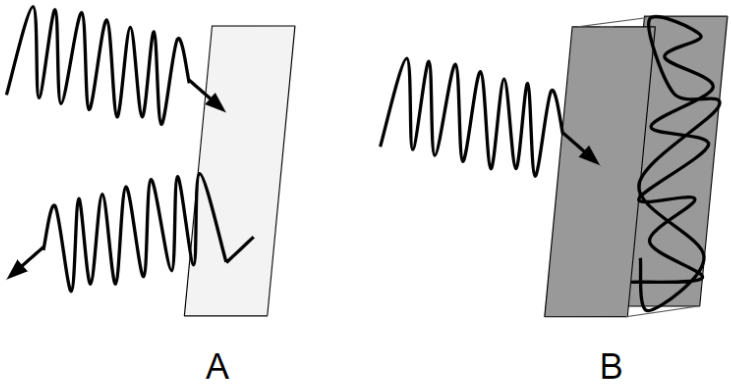

Figure 18 - A - EMI shielding in metals - reflection; B - EMI shielding in CPC's - absorption.

Electrically conductive composites based on carbonaceous nanofillers (carbon nanotubes, carbon black, graphene, etc.) have shown interesting results regarding the EMI shielding efficiency when combined with polymers like ABS and PLA. Traditional forming and processing routes for the design of these applications have been outshone in some respects by the possibilities that AM brings, especially using FFF. These configurations in conjunction with optimal printing parameters can provide great electromagnetic attenuations. Furthermore, the percentage of filler in the composite, used to provide conductive properties, also affects the processability of the material. In this sense, the good marriage between the value of filler content, the structural configuration of a part and the printing parameters is crucial. This makes the challenge of designing and producing FFF components for this application a difficult task (Schmitz et al., 2023) (Ecco et al., 2018).

(Schmitz et al., (2023) presented some configurations that have efficient EMI shielding properties:

- Porous nanoparticles such as metal–organic frameworks.
- Hollow nickel nanoparticles modified with reduced graphene oxide.
- Porous carbon nanorods.
- Porous structures of ferrite/polyaniline and polyimide.
- Foamed conducting composites constituted by thermoplastic and carbonaceous conducting fillers.

However, in some cases, a large amount of filler is necessary, thus increasing density and cost of the final product. In order to minimize these drawbacks, the development of hollow/porous structures has become of interest. In addition to minimizing the weight of the end product, the porous structures have the ability to efficiently reduce electromagnetic (EM) energy across a wide frequency spectrum by reflecting and dispersing the EM wave within the absorber. Honeycomb structures have become very popular regarding this matter (Schmitz et al., 2023).

FFF printing of honeycomb structures in flexible materials have been investigated for the purpose of creating energy, impact, and EMI absorbent properties to be used in many fields of technological and engineering applications. The high strength-to-weight ratio and the ability to alter the electric and magnetic response of the structure by changing its geometry make honeycomb sandwich composites a promising option for developing microwave absorbing structures (Schmitz et al., 2023) (Bates et al., 2016).

Regarding the honeycomb cellular structure, its working mechanism related to its compressive behavior is divided as follows: first linear elasticity moment where there is simple bending of the walls (Figure 19). This is followed by a plateau in deformation caused by the buckling of the cell walls together, which is the main mechanism responsible for the energy-absorbing properties of the structure. Finally, a maximum density of the component is reached, where the stiffness increases up to close to that of the material itself. Regarding the density of the honeycomb, the structure with the intermediate density is optimized for absorbing energy. The optimization of a uniform-density cellular structure is based on compression energy, which serves as a means of determining the energy absorption capability and effectiveness of the structure. Identifying this energy is one approach to quantify the efficiency of a cellular structure (Bates et al., 2016).

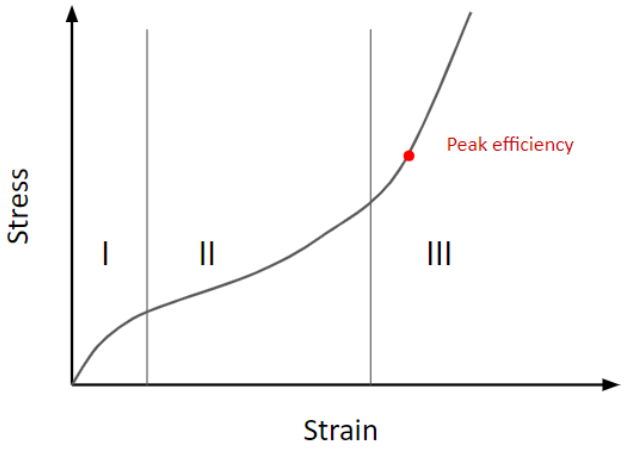

Figure 19 - Compressive behavior of cellular structures: I - First linear moment; II - Plateau in deformation; III - Densification.

Bates et al. (2016, 2019) analyzed TPU honeycomb cellular structures and reported that uniform density specimens of this combination achieved good results in terms of energy absorbing characteristics.

In structures containing honeycomb as core, surrounded by an insulating material, the top layer works as the matching one and its role is to allow the penetration of the EMW into the sandwich structure and, at the same time, trapping it inside the honeycomb layer to insure attenuation by internal reflection, Figure 20.

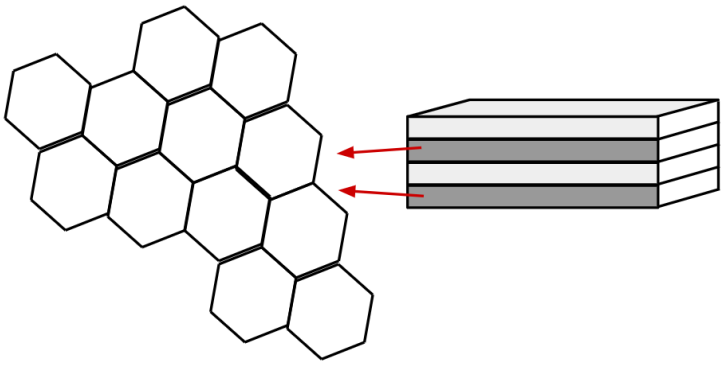

Figure 20 - Honeycomb Sandwich structures.

Past works have found a link between the multilayer impedance matching and the changing in thickness and number of layers, pore size and thickness of the honeycomb structure, in a honeycomb sandwich composite. It has been observed that for carbon-coated honeycomb microwave absorbing materials (HMAMs), the pore size and honeycomb thickness exerts a great influence on the absorption peaks frequency (Schmitz et al.,2021, 2023).

Schmitz et al. (2023) detailed some conclusions related to the bibliography on the subject matter presented in Table 2.

Table 2 - Bibliography reviewed on the topic of honeycomb structures for EMI SE.

(Li et al., 2020)	Conductive ABS honeycomb-based structured samples produced via FFF with smaller thickness showed better reflection loss (RL) responses, and the thickness had an inverse relation with the frequency. Also, smaller cell sizes tend to enhance the RL of the absorber, which was attributed to its denser pore structure.
(Laur et al., 2021)	Considering three different cell sizes on the RL of honeycomb samples made by FFF with conductive PLA, the RL peak shifted to higher frequencies with the decrease in cell size.

(Lv et al., 2022)	For honeycomb (PLA loaded with graphene nanoplatelets (GNP) and CNT hybrids) samples with straight, triangle, square, and honeycomb fill patterns, the best configuration regarding the EMI SE (Electromagnetic Shielding Efficiency) was the latter. They proceeded to investigate how the size of cells impacts the efficiency of EMW absorption and concluded that smaller cells yield superior results.

Another way to create a tailored application to optimize the energy absorption characteristics of a structure by FFF is energy grading the cellular configuration of a honeycomb pattern in different regions, for example with a convex grading. This solution has, generally, a better performance than uniform density hexagonal structures. Bates et al. (2019) evaluated the inclusion of density grading by having different sections of the cellular structure with different thickness of the cellular walls, as shown in Figure 21. However, other types of grading are possible to produce through FFF such as using a variety of materials with different stiffness to reduce printing time without losing mechanical properties. The authors observed that only close to max compaction and at low compression energies would improvements in energy absorption occur, whereas between the extremes, uniform density configurations outperform the ones studied. However, the authors verified that the graded configuration absorbed more energy up to densification. The strain on densification is higher, which results in a non-linear relationship between density and energy absorption.

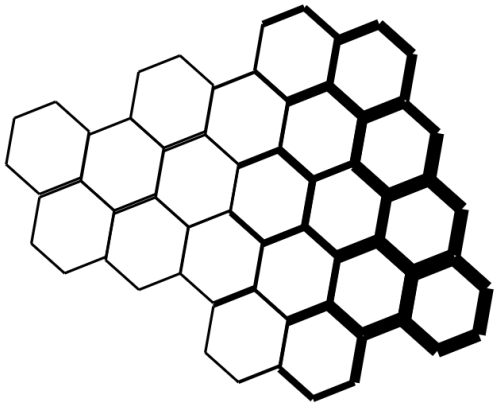

Figure 21 - Example of a density graded HC pattern.

Other studies have also shown an influence of the filler type, the fabrication route and even the printing pattern in the case of FFF and EMI shielding effectiveness (EMI SE) (Figure 22). The manner in which the printing patterns are defined should ensure that the component produced through FFF has minimal electrical resistance to the flow of charges, thereby resulting in greater volume electrical conductivity (Schmitz et al., 2018).

Ecco et al. (2018) observed that for composites of ABS loaded with CNT, GNP, or just ABS, compression molding fabrication offers the highest value of attenuation independently, due to the better compaction and lack of defects and voids. They also reported better attenuation of the ABS/CNT samples for all conditions, this being related to the higher electrical conductivity of this formulation. Research also showed that the printing pattern, Figure 22, seemed to have a higher influence on the EMI SE values, being the decreasing order of EMI SE as follows: PC, HC, H45. In the PC samples there is a continuous pathway for the charges (they go through the filament deposition direction), despite the voids and defects. For the latter samples, the charges must go through the layers and their interfaces. It was concluded that layer height of 0.1 mm, for instance resulted in lower EMI SE values, due to the presence of openings between the deposited filaments (Schmitz et al., 2018, 2021) (Ecco et al., 2018).

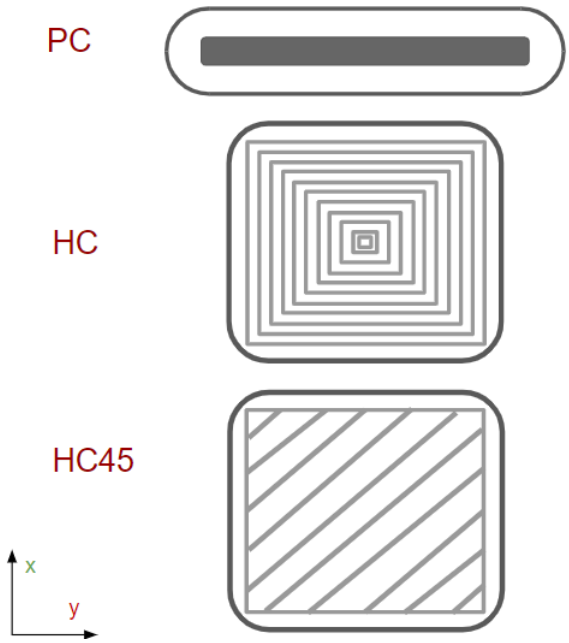

Figure 22 - Growing directions and patterns, respectively, used in the study conducted by Schmitz et al. (2021), PC - Perpendicular and Concentric; HC - Horizontal and Concentric; HC45 - Horizontal and alternate diagonal 45-degree angled raster.

Ecco et al. (2018) also observed that FFF-PC of ABS/CNT presented similar values to the same formulation produced by compression molding. Despite the lower amount of material to interact with the EM radiation, the shielding efficiencies for FFF-PC components might be higher due to the occurrence of multiple internal interactions. This justifies the need for higher EMI shielding.

Schmitz et al. (2018) reported higher values of electrical conductivity obtained for the composites with CNT followed by the hybrid systems and by the systems with CB incorporated.

This is due to the continuous conductive network formed by the CNT in the ABS matrix as well as its own higher electrical conductivity.

Ecco et al. (2018) and Schmitz et al. (2018) also reported EMI SE values lower than -20 dB (99% wave attenuation - the minimum value to ensure safety of electronic devices from interference). ABS multi-walled carbon nanotube-based polymer composite with 6 wt. % of MWCNT (Multi-Walled CNT) shows attenuation capacity of 99.9 % toward the incident EM wave. Considering the application of FFF printed structures to EMI shielding solutions, the good balance between printing configurations, material compositions and geometrical design provides an advantage of its manufacturing route in this field. Furthermore, if the limitations regarding the difficulty in processing higher filler contents were surpassed, much higher attenuations and shielding effectiveness would be easily achieved. Machines that could work at higher deposition temperatures, lower deposition rate, and lower layer height could provide new solutions.

Bertolini, Dul, Barra, et al. (2021) and Bertolini, Dul, Lopes Pereira, et al. (2021) provide more specific information regarding the incorporation of TPU in EMI shielding mechanisms, presenting the advantages and drawbacks of this option as well as analyzing furthermore the influence of filler content in the efficiency of these structures. Bertolini, Dul, Barra, et al. (2021) studied the co-blend of a PVDF and TPU polymer matrix with CB-PPy (Carbon Black-Polypyrrole) as filler to produce highly conductive but also flexible filament for FFF. In another work, Bertolini, Dul, Lopes Pereira, et al. (2021) have demonstrated a viable option of using flexible conductive polymers composed on TPU/PVDF blends filled with CB-PPy for piezoresistive pressure sensor.

The information presented above confirms the use of carbon black (CB) in multi-material products intended for electromagnetic interference (EMI) shielding structures. By strategically incorporating different material compositions and geometries, such as honeycomb patterns and density grading, these products can be optimized to efficiently minimize the impact of electromagnetic radiation. This approach leads to enhanced EMI shielding performance. Consequently, the purpose of this thesis is to investigate the adhesion strength between CB/TPU and natural TPU, with the goal of developing future EMI shielding applications.

3. Materials and Methods

The current chapter presents the methodology and materials used in the experimental work.

3.1 Materials

The polymer filaments used in the work are as follows: **A** - A cleaning filament made of PLA, which was used between prints to clean the nozzle and preventprinting failures; Two bobbins of TPU insulating grades filaments, one with a grey coloring (**D**) and one transparent (**B**); **C** - Two bobbins of conductive TPU filament composed on TPU and CB. All filaments were purchased fromthe same manufacturer. Table 3 shows the main supplier information of the filaments used inthe thesis.

Table 3 - Properties of the filaments used in the thesis.

Properties	**A**	**B**	**C**	**D**
Supplier	*Smartfil*	*Fillamentum*	*Recreus*	*Fillamentum*
Name	CLEAN	Flexfill TPU 92A “Natural”	Conductive FilaFlex	Flexfill TPU 92A “Metallic Grey”
Color	White	Transparent	Black	Grey
Filament Diameter (mm)	1.75	1.75	1.75	1.75
Glass Transition Temperature (^{o}C)	--	--	--	--
Density (g/cm3)	1.23	1.21	1.33	1.21
Melt Temperature (^{o}C)	--	--	--	--
Printing Bed Temperature (^{o}C)	--	50-60	50-60	50-60
Printing Temperature (^{o}C)	190-250	220-240	245-250	220-240
Electrical Resistivity (Ω/cm)	> 10^{12}	> 10^{12}	3.9	> 10^{12}

3.2 Methodology

Parallel to the execution of the main work, the two original filaments, “D” and “E”, the natural TPU and the CB/TPU were characterized via a FTIR analysis in order to assure the main characteristic absorption bands regarding carboxyl groups of TPU.

In order to calibrate the printing parameters to better serve the material used, a trial-and-error process was initiated based on the production of a set of five 15 mm^3 parts of each filament. The validation or recusal of the printing configuration was done through mass and dimensional assessments and a general visual inspection. Some of the specimens produced from each calibration were also 3D scanned to compare the geometry produced by the printer with the original CAD design. Furthermore, the nozzles used during this phase of the experiment were analyzed microscopically regarding their inner surface damage. To this intent, the nozzles were previously cut in half via a resin assisted process.

Considering the parametric analysis performed to determine the best printing configuration for the higher bonding strength of multi-material specimens, a set of a minimum of 48 samples were produced, visually and microscopically inspected, and evaluated via pull-out tests.

Finally, different configurations of multi-material samples with solid/honeycomb structures were produced to be used in future studies regarding EMI SE. A prototype of an EMI shielding phone case was developed to verify the capability of honeycomb multi-layered structures made on TPU and CB/TPU in attenuating radiation. Figure 23 shows the sequencing of the work performed during the dissertation’s timeline.

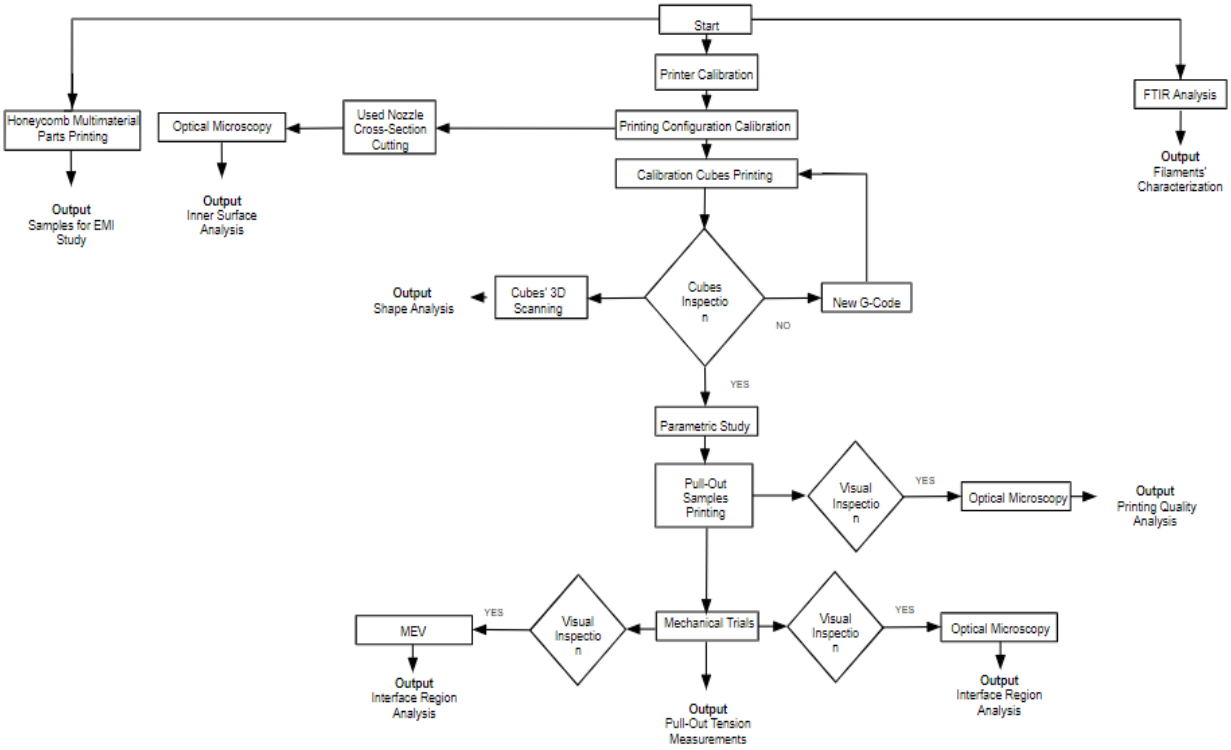

Figure 23 - Working sequence for the dissertation.

3.2.1 FTIR Analysis

The FTIR technique allows for the identification of polymeric components. One small segment of each filament was used to perform this analysis, Figure 24.

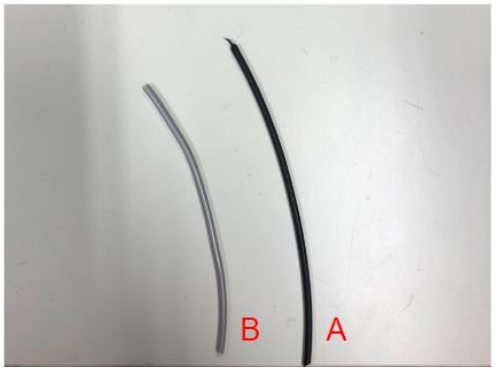

Figure 24 - Segments used for FTIR analysis: A - natural TPU; B – CB/TPU.

The tests were performed at the Lubricants Laboratory (CETRIB/INEGI) in a Cary 630 FTIR equipment from Agilent Technologies. Figure 25 shows the analysis for spectrum identification of each sample filament.

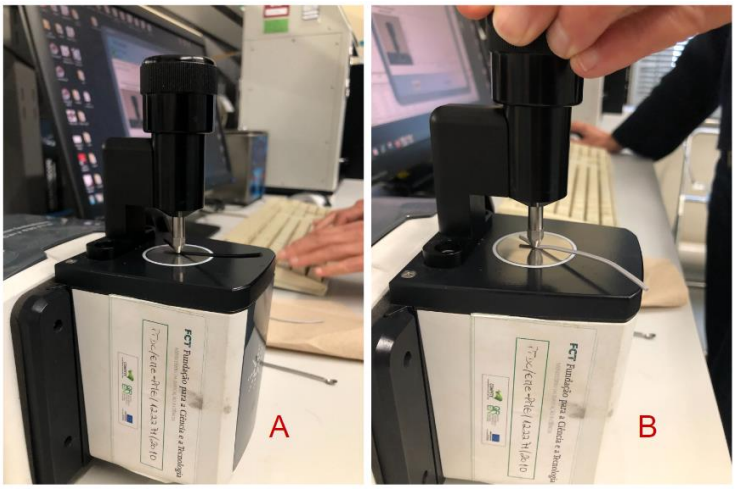

Figure 25 - FTIR analysis: A - CB/TPU segment, B - TPU segment.

3.2.2 Mass Measurement

The mass measurement was done in an electronic scale from *Scale House* (0,001 g resolution) available at the *LPDS* at *FEUP,* as shown in Figure 26. All the printed cubes were measured once.

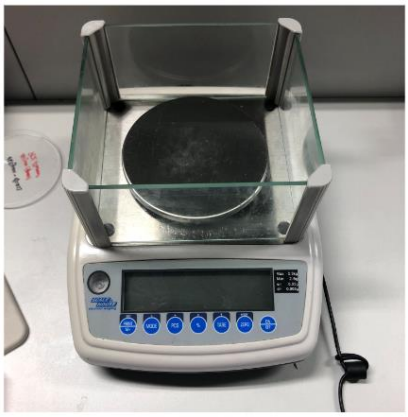

Figure 26 - Electronic scale used in the thesis.

3.2.3 Dimensional Measurements

The dimensions of the samples were assessed using a digital caliper, *Absolute Digimatic AOS* caliper by *Mitutoyo™* with a +/- 0,05 mm resolution, Figure 27.

Figure 27 - Digital caliper used in the thesis.

3.2.4 Pull-Out Test

In order to evaluate the bonding strength of the samples, mechanical trials were performed using a MultiTest2.5-dv machine by Mecmesin. The machine was software-controlled and used Vector Pro to monitor and retrieve data. A 2.5 Kn load cell and traction claws were utilized for the trials. This equipment was accessible at *FEUP* in the *LPDS* department, as shown in figure 28.

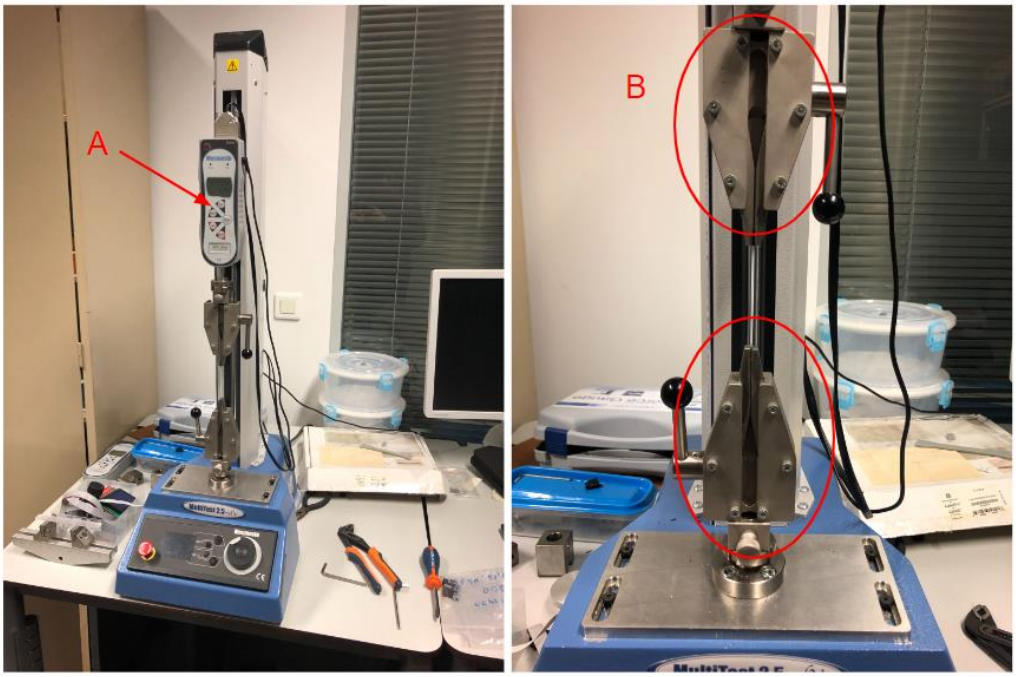

Figure 28 - Multitest machine: A - Load cell; B - Mechanical Claws.

The sample was initially fixed manually by the claws and the load cell was put to zero. The upper claw was set to move upwards at 10 mm/s speed to a maximum displacement value of 100 mm. The test was stopped manually when the fracture occurred or automatically if the maximum displacement was reached.

3.2.5 Microscopic Analysis

The samples produced for the parametric study were selected based on their visual inspection to be analyzed microscopically. Subsequently, samples which presented higher bonding strength via the pull-out test and also exhibited good surface quality were also microscopically analyzed to report the state of the interface surface post-fracture. The device used for this prospect can be seen in Figure 29. Zeiss Axiophot microscope equipped with a digital Olympus camera (El Einsatz 45 18 87) of the Materiallographic laboratory of the DEMec was also used to analyze the cross-section of cut nozzles used during the calibration phase.

Figure 29 - Zeiss Axiophot microscopy and image center used in the thesis.

3.2.6 Nozzle Analysis

Two used nozzles were analyzed, called "A" and "B", to examine their inner surface quality. Nozzle "A" was a replacement nozzle used during calibration, while Nozzle "B" was the original nozzle used at the beginning of the process. Both nozzles were removed from the printer as they were no longer needed.

Figure 30 exhibits the materials used to prepare the nozzles for optical microscopy analysis. The nozzles were positioned in a plastic mold, with the help of a clamp, to be aligned

perpendicularly to the mold lid. Next, with the help of the spoons, the resin powder was mixed with the catalyst for 1 minute with a 2:1 mass ratio, respectively. This mix was then poured on to the container, solidifying around the nozzle.

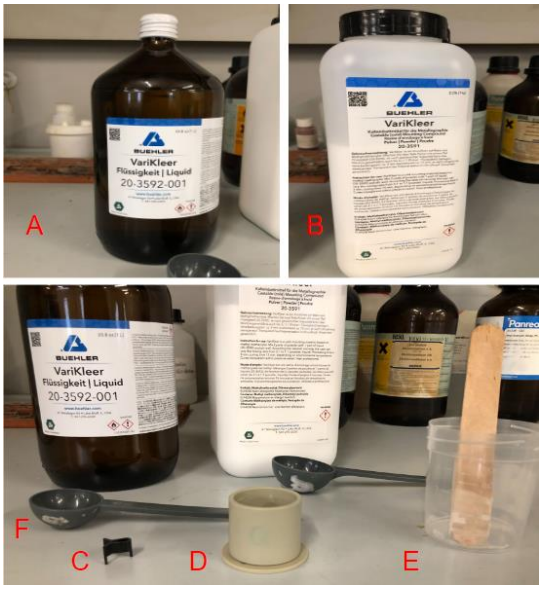

Figure 30 - Materials used for the resin production: A - Liquid Agent; B - Powder Agent; C - Support piece; D - Mold; E - Cup; F - Spoons.

A and B in figure 31 represent the catalyst and the resin powder respectively *VariKleer Liquid* and *VariKleer Powder* both commercialized by *Buehler*.

After this step, the nozzle embedded in resin was cut in half in an Accutom-5 precision cut-off machine (*Struers*) (Figure 31) using a diamond cutting wheel M1D13, figure 32. The cutted specimens are shown in Figure 33.

Figure 31 – Cutting station.

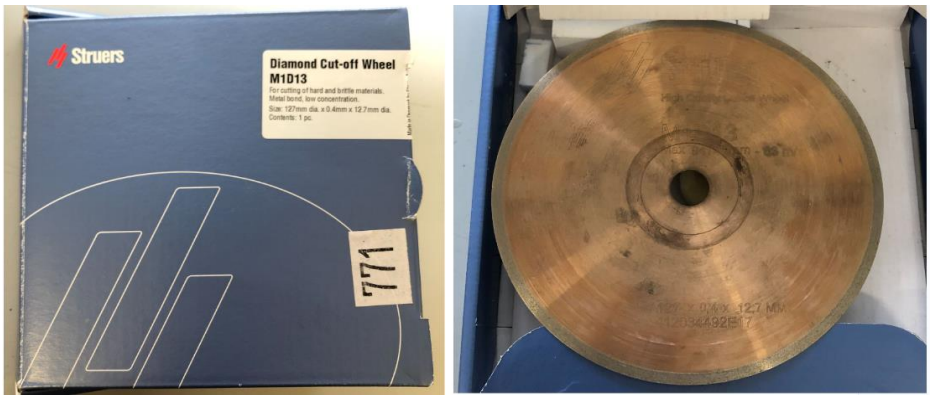

Figure 32 – Cutting disk used, 127 mm dia x 0,4 mm x 12,7 mm dia.

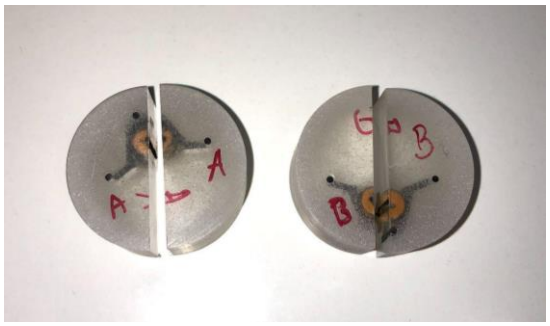

Figure 33 - Nozzle “A” and “B” after the cutting operations.

To ensure good visualization, the inner surface was further cleaned to remove the excess of polymer still present in the nozzle with soldering equipment (figure 35, A).

3.2.7 Other Materials

Adjacent to the materials used regarding the main framework of the thesis, other equipment was used for the purpose of facilitating the project. Cutting clamps, different pliers, spatula, soldering equipment, as well as hair spray that were all applied in conjunction with the printing process, either to clean, remove, or adjust and maneuver around the printer (nozzle cleaning for instance) and the printed part, as illustrated in Figure 34.

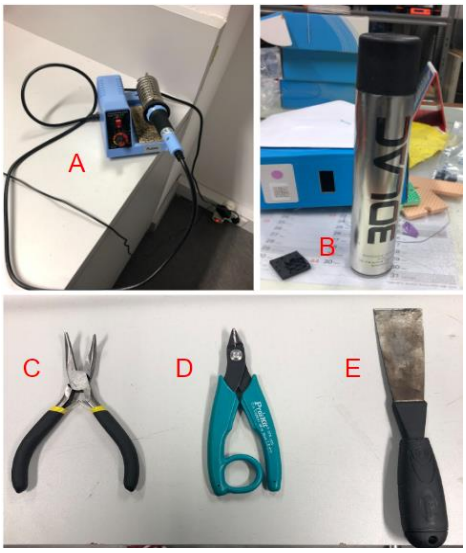

Figure 34 - A - soldering equipment; B - Hair spray; C - Plier; D - Cutting Clamp; E - Spatula.

3.3 Printer and Printing Software

The samples required to the work were printed in a Prusa i3 MK3S printer (Figure 35), using the open-source slicing software, *PrusaSlicer* version 2.7.0, allowing the conversion of the STL files provided by CAD into a G-code transmittable to the printer via a memory card, and the definition of the printing configurations. Figure 36 shows an example of a multi-material part configured with the software. The technical characterization of the printer is depicted in Table 4.

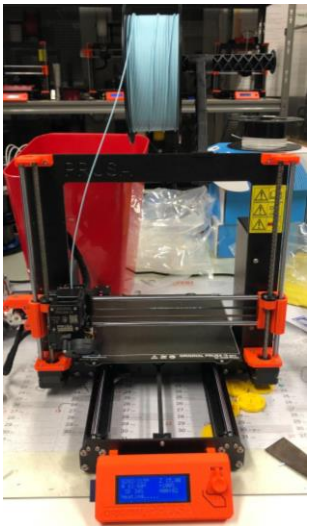

Figure 35 - Prusa i3 MK3S used during the thesis.

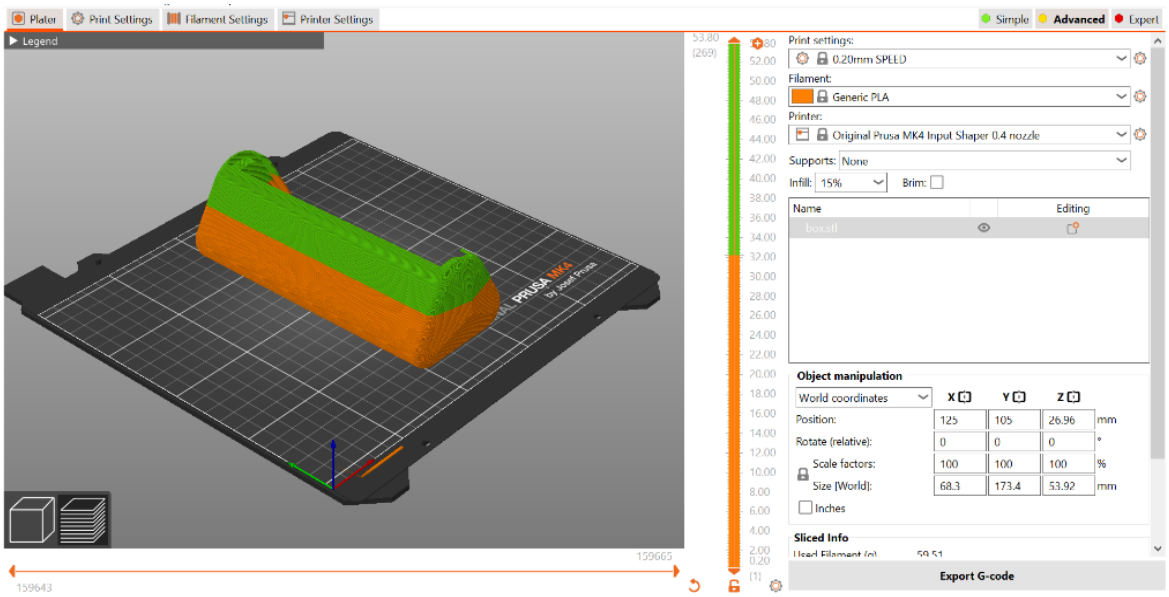

Figure 36 - Prusa's slicing software, multi-material example part.

Table 4 - Prusa i3 MK3S specifications.

Build Volume (cm)	25×21×21	**Max Nozzle Temperature (°C)**	300
Layer Height (mm)	0,05 - 0,35	**Max Heatbed Temperature (°C)**	120
Nozzle (mm)	0,4 default	**Extruder**	Direct Drive, Bondtech Gears, V6 Hotend
Filament Diameter (mm)	1.75	**Print Surface**	Removable magnetic steel sheets (*) with different surface finishes, heatbed with cold corners compensation
Supported Materials	PLA, PETG, ASA, ABS, PC (Polycarbonate), CPE, PVA/BVOH, PVB, HIPS, PP (Polypropylene), Flex, nGen, Nylon, Carbon filled, Woodfill, etc	**Printer Dimensions (kg, mm)**	7 500×550×400
Max Travel Speed (mm/s)	200	**Power Consumption (W)**	80-120

3.4 Printing Configuration Optimization

The printing configuration optimization was conducted in two steps. The first step was the calibration of the printer. An automatic calibration of the printer was performed initially. Secondly, the first layer calibration was executed (Figure 37). This was optimized for the selected filaments and represents the optimal distance between the nozzle and the bed while depositing the first layer of material. The geometry produced should present no continuity flaws and sufficient adhesion to the printer bed, squeezing the filament as observed in Figure 10 (Section 2.1.2). Theoretically this step only must be done once, and any optimization of future printed parts is executed changing the printing configurations in the slicing software.

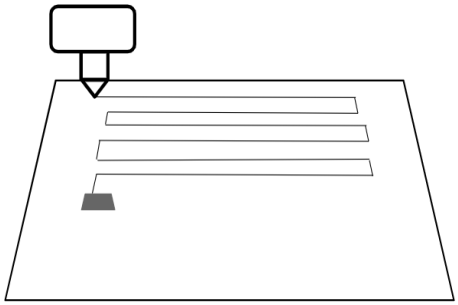

Figure 37 - First layer calibration geometry-type.

To reach the best printing parametrization of the TPU parts, as stated above in section 3.2, sets of up to five cubes were produced (Figure 38). The cubes' mass and dimensions were measured. For the statistical analysis, the width, length, and height of the cubes were measured three times. The average, standard deviation, and coefficient of variation (CV) were all calculated for the x, y, and z dimensions. The criteria for validation were a CV below 10%. The coordinate system applied was developed by the method seen below.

For each produced part, the last contact point between the nozzle and the cubic piece left a noticeable mark in the upper surface, represented by the point in Figure 38, which was always located near the corner of the piece. This reference point was used for the coordinate system.

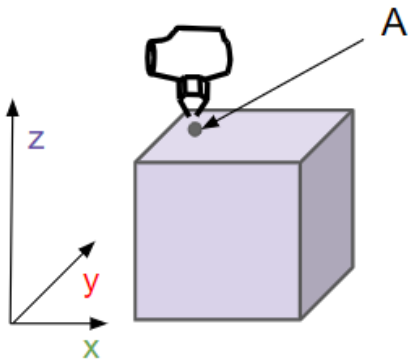

Figure 38 - Coordinate System for the cubes based on point A.

3.4.1 Cubes' 3D Scanning

Besides the visual inspection of the parts to assure good printing quality, four samples (Figure 39) were chosen to be 3D scanned (*ZEISS* Triple Scan - Atos III Rev. 02, INEGI). These samples were made of TPU and CB/TPU filament from two different configurations. During the printing calibration phase various iterations were performed to reach an optimal parametrization of the cubes produced. Version 3 corresponds to the cubes printed with the optimal parameterization reached in the calibration section and version 2 is a prior iteration. This classification will be further detailed in section 4.2.

Figure 39 - Samples chosen for the shape analysis: 2N - Version 2 natural filament; 3N - Version 3 natural filament; 2C - Version 2 CB /TPU filament; 3C - Version 3 CB/TPU filament.

Prior to the scanning, the cubes were sprayed with an anti-reflection agent, as illustrated in

Figure 40, to assure that all surfaces of the part were visible. Figure 41 shows the positioning of the part in the supports. Since the goal was to analyze the shape variability between deposited layers, the base and top of the samples were the priority. For this intent, the part was laid on its side, z axis horizontal.

Figure 40 - Spraying of the samples to be scanned.

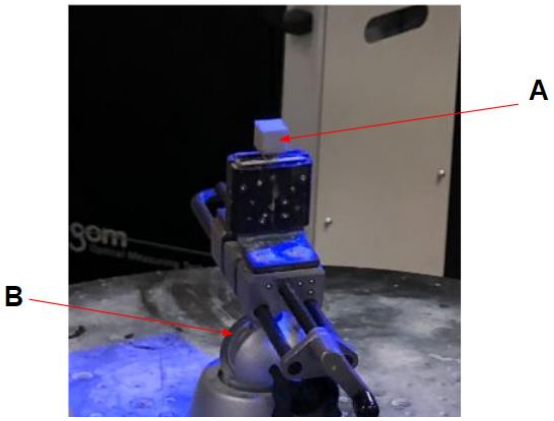

Figure 41 - Samples positioning 3D scanning: A - Bottom layer; B - Support.

Since the layer that is in contact with the support is not able to be scanned, this arrangement allowed for the important faces of the cubes to be retrieved, discarding one of the side faces in the process. After the spraying and proper placement of the cubes the scanning was executed, as shown in Figure 42.

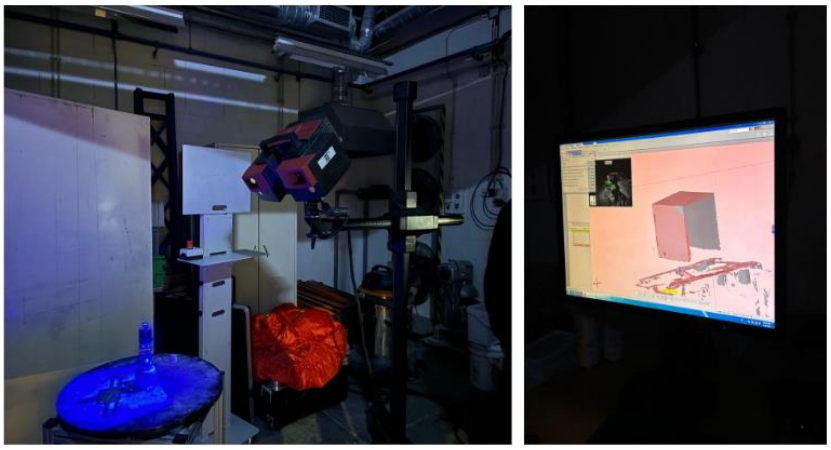

Figure 42 - 3D scanning execution.

The analysis of the samples was done using the software *GOM Inspect* from *ZEISS*.

3.5 Parametric Study

To evaluate the influence of the printing configurations on the product quality of the printed part as well as the mechanical bonding strength of the interface in multi-material samples, a parametric study was conducted. Table 5 shows the 48 configurations adopted. These configurations were defined by varying some parameters defined in the printing calibration sections of the work. Temperature, extrusion speed, retraction, cooling, and extrusion multiplier value were all altered in different combinations.

Table 5 - Printing configurations of the parametric study.

Parameter	Extrusion Temperature (°C)	Bed Temperature (°C)	Infill Speed (mm/s)	Perimeter Speed (mm/s)	Retraction (mm)	Cooling	Extrusion Multiplier (u.a)
1	210	60	5	10	0	Off	1
2	210	60	5	10	1,5	Off	1,15
3	210	60	5	20	0	On	1
4	210	60	5	20	1,5	On	1,15
5	210	60	15	10	0	On	1,15
6	210	60	15	10	1,5	On	1
7	210	60	15	20	0	Off	1,15
8	210	60	15	20	1,5	Off	1
9	210	90	5	10	0	On	1,15
10	210	90	5	10	1,5	On	1
11	210	90	5	20	0	Off	1,15
12	210	90	5	20	1,5	Off	1
13	210	90	15	10	0	Off	1
14	210	90	15	10	1,5	Off	1,15
15	210	90	15	20	0	On	1
16	210	90	15	20	1,5	On	1,15
17	230	60	5	10	0	Off	1
18	230	60	5	10	1,5	Off	1,15
19	230	60	5	20	0	On	1
20	230	60	5	20	1,5	On	1,15
21	230	60	15	10	0	On	1,15
22	230	60	15	10	1,5	On	1
23	230	60	15	20	0	Off	1,15
24	230	60	15	20	1,5	Off	1
25	230	90	5	10	0	On	1,15
26	230	90	5	10	1,5	On	1
27	230	90	5	20	0	Off	1,15
28	230	90	5	20	1,5	Off	1
29	230	90	15	10	0	Off	1
30	230	90	15	10	1,5	Off	1,15
31	230	90	15	20	0	On	1
32	230	90	15	20	1,5	On	1,15
33	245	60	5	10	0	On	1,15
34	245	60	5	10	1,5	On	1
35	245	60	5	20	0	Off	1,15
36	245	60	5	20	1,5	Off	1
37	245	60	15	10	0	Off	1
38	245	60	15	10	1,5	Off	1,15
39	245	60	15	20	0	On	1
40	245	60	15	20	1,5	On	1,15
41	245	90	5	10	0	Off	1
42	245	90	5	10	1,5	Off	1,15
43	245	90	5	20	0	On	1
44	245	90	5	20	1,5	On	1,15
45	245	90	15	10	0	On	1,15
46	245	90	15	10	1,5	On	1
47	245	90	15	20	0	Off	1,15
48	245	90	15	20	1,5	Off	1

Other parameters not specified in table 5 were kept constant and equal to those of the optimal configuration obtained in section 3.4. Table 6 shows constant parameters. These were achieved by the iterative process of the calibration phase. Some, such as fill pattern and fill angle were defined by using the standard configurations for TPU printing in *Prusa Slicer*.

Table 6 - Constant parameters for the samples of the study.

Layer Height (mm)	0,1
First Layer Height (mm)	0,3
Perimeters	3
Fill Density (%)	100
Fill Pattern	Rectilinear
Fill Angle (Degrees)	45

Considering the optimum printing configuration obtained in the calibration phase, sets of 3 samples were also printed with each of the following materials (Figure 43), for comparative purposes:

- Samples made on natural TPU denominated “bb_#”.
- Samples made on CB/TPU denominated “pp_#”.
- Multi-material samples half-printed in natural TPU and then sequentially, half-printed in “black TPU” “pb_#”.

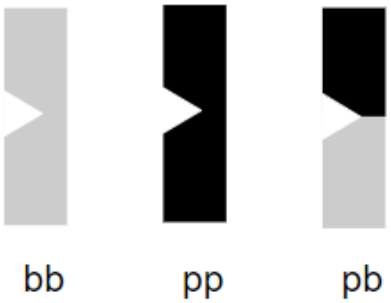

Figure 43 - Formulation of the samples printed with the default optimum parameters.

The samples were also defined as “P” samples in reference to the word *Padrão*, meaning “standard”, since the standard used for comparison in the parametric study was the parametrization achieved up to that point. For instance, the first sample printed in the standard printing configurations made entirely of natural TPU would be named “P bb_1”.

The sample’s geometry was adapted from specimens used in Charpy notch sensitivity impact tests, to induce failure in the interface region. Figure 44 and Figure 45 show the design, dimensions and the project made on *PrusaSlicer* (Tvergaard & Needleman, n.d.).

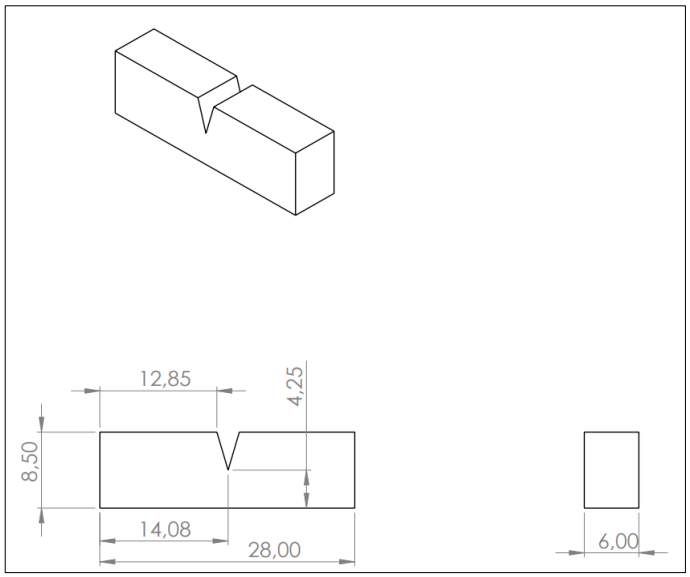

Figure 44 - Dimensions of the pull-out samples.

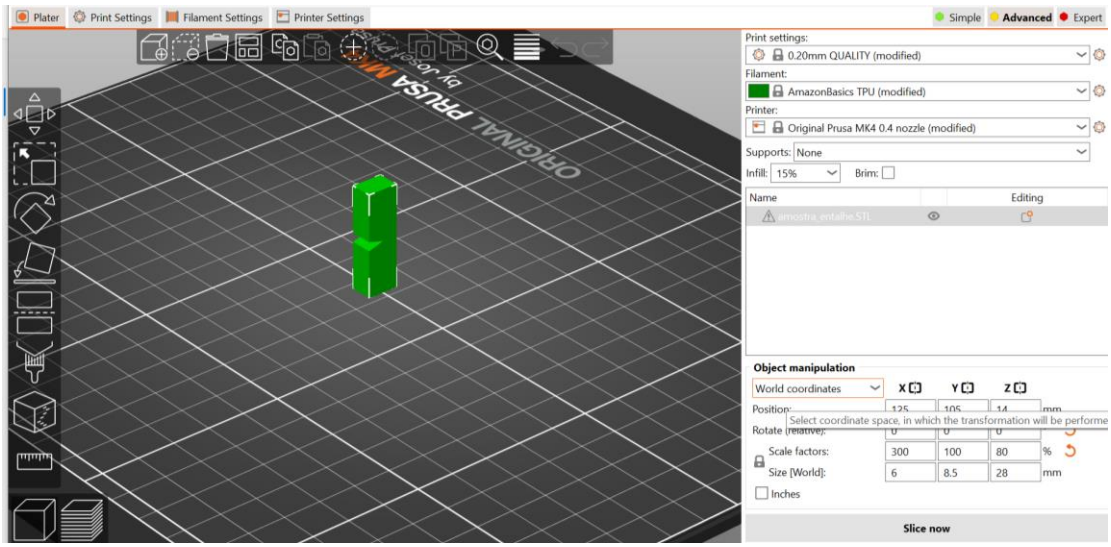

Figure 45 - PrusaSlicer window view of the project for the pull-out sample.

The printing of samples of the parametric study were all performed with the same sequencing. This means that the bottom half of the part was produced in natural TPU. When the first portion of the printing was completed, the filaments were manually switched, and the rest of the part was printed in CB/TPU. The reasons for the choice of this sequencing will be further explored in the results section.

Furthermore, it was assured that the notch in the sample was aligned with the interface region between the two materials in the specimen, defined via the slicing software (Figure 46).

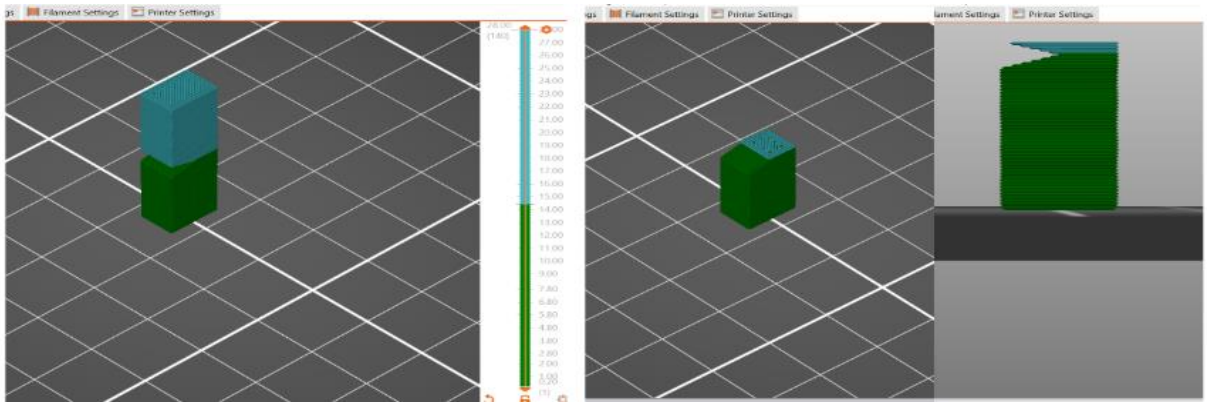

Figure 46 - Multi-material geometric division of the samples in PrusaSlicer.

After the completion of the printing of the samples, mechanical trials were performed using the equipment described in 3.2.4 in order to compare the bonding strengths of the interface region. Figure 47 illustrates one sample being fixed with the claws of the testing machine. The test results were retrieved from the device's monitoring software and the statistical analysis was conducted on Excel and *OriginLab*.

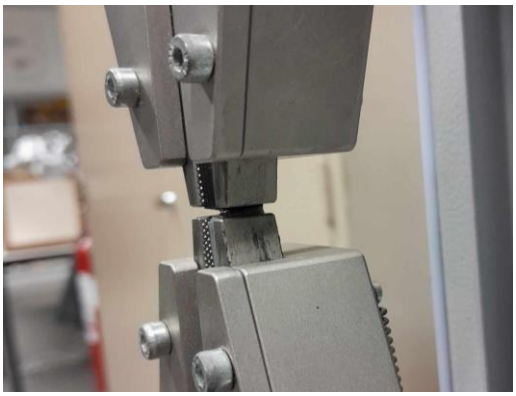

Figure 47 - Sample positioning for the mechanical trial.

3.5.1 SEM

A small subset of the samples was chosen to be analyzed by scanning electron microscopy at *CEMUP*, specifically targeting the boundary interface region.

Furthermore, to complement the FTIR analysis, a segment of each feedstock material was cryogenically fractured at *FEUP*. The segment of filament was submerged into nitrogen with the aid of pliers, Figure 48. After the material became rigid, fracture was induced manually. The natural TPU sample was named “A” and the CB/TPU sample named “B”.

Figure 48 - Cryogenic fracture of the segments.

The SEM / EDS analysis was conducted in a High resolution (Schottky) Environmental Scanning Electron Microscope with X-Ray Microanalysis and Electron Backscattered Diffraction analysis (FEI Quanta 400 FEG ESEM / EDAX Genesis X4M). Samples were coated with an Au/Pd thin film, by sputtering, using a SPI Module Sputter Coater equipment, as shown in Figure 49.

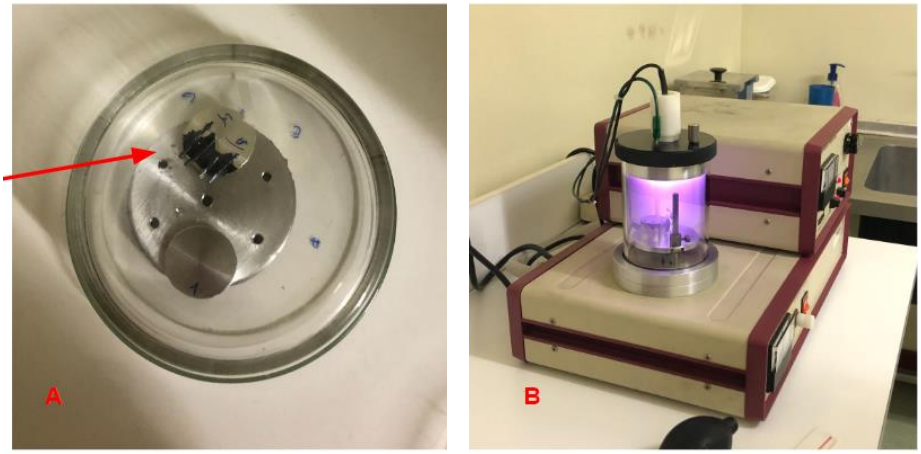

Figure 49 - Sample preparation for SEM; B - Gold and palladium coating.

The preparation of the parametric study samples followed the same procedure. However, in this case they were not fractured as it was intended to view the boundary interface surface quality in the specimens. Figure 50 shows the positioning of the samples to be viewed.

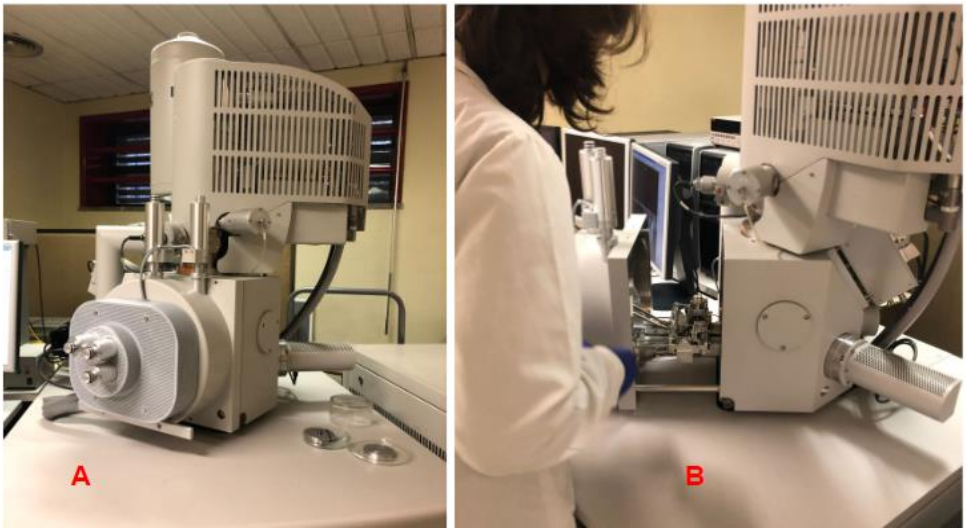

Figure 50 - A- High resolution (Schottky) Environmental Scanning Electron Microscope at CEMUP; B - Positioning of the specimens.

3.6 Case Study

As a practical introduction for future research, the feasibility of producing multi-material FFF sandwich parts with honeycomb intermediate layers was studied. As a first step, honeycomb structure parts were produced using either the natural or CB/TPU. Secondly, samples with solid-honeycomb-solid configurations were printed using factorial combinations of the natural and CB/TPU filaments. Figure 51 and Figure 52 show some examples of the different samples (50 mm^2 and 5 mm height) produced in this section of the work.

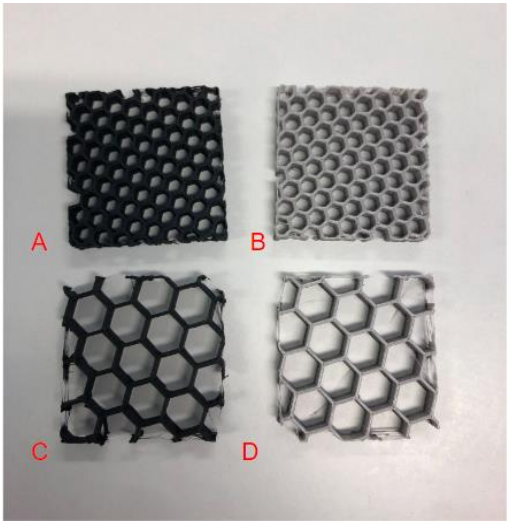

Figure 51 - Honeycomb structures: A - CB/TPU 20% density; B - TPU 20% density; C - CB/TPU 10% density; D - TPU 10% density.

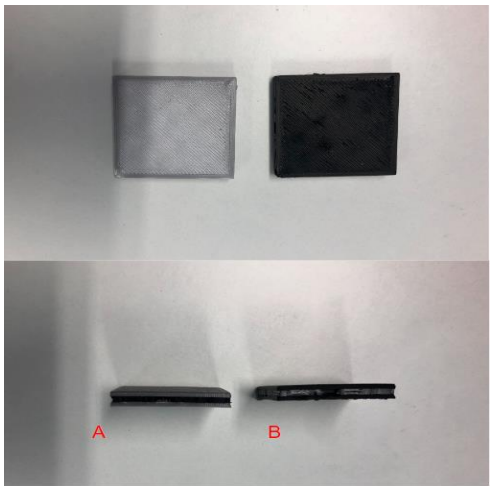

Figure 52 - Honeycomb sandwich structures: A - TPU-CB/TPU-TPU; B - CB/TPU-TPU-CB/TPU.

It was decided to compose a prototype EMI Shielding solution for simple electronic devices. With this in mind, a phone case was developed destined to attenuate external electromagnetic signals. The case was printed using solid layers of natural and CB/TPU for outer surfaces of the part and an intermediate layer of CB/TPU honeycomb structure. The construction steps of the part can be seen in Figure 53 and Figure 54.

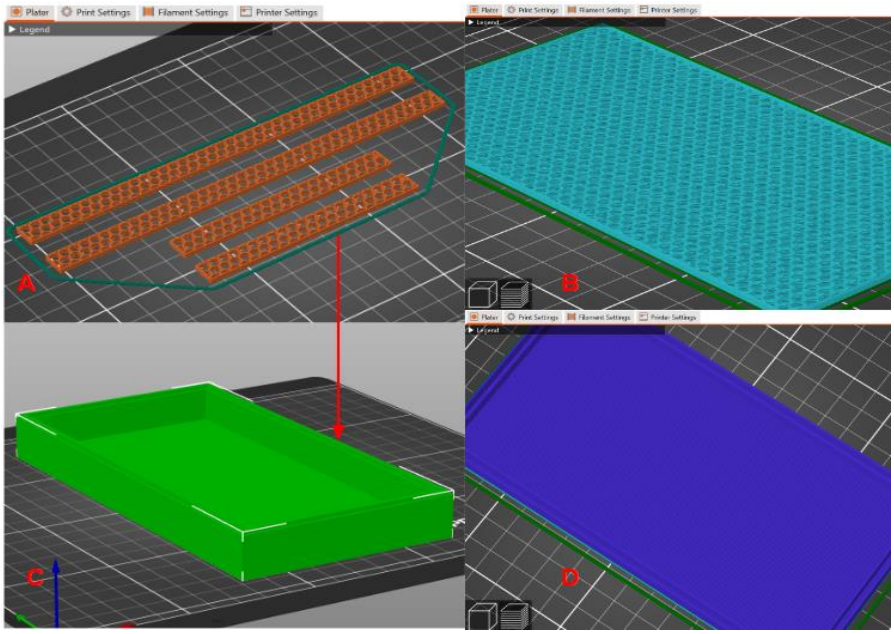

Figure 53 - Base and lateral components of the case: A - Lateral honeycomb walls; B - Honeycomb intermediate layer of the base; C - Full base geometry; D - Solid infill on the upper surface of the part.

The honeycomb lateral structures were produced separately and manually inserted in the base's side slot during its printing. The cover was done using a first solid layer on the lower surface and by using a size gradient of the honeycomb structure for the upper layers of the part with a final solid layer.

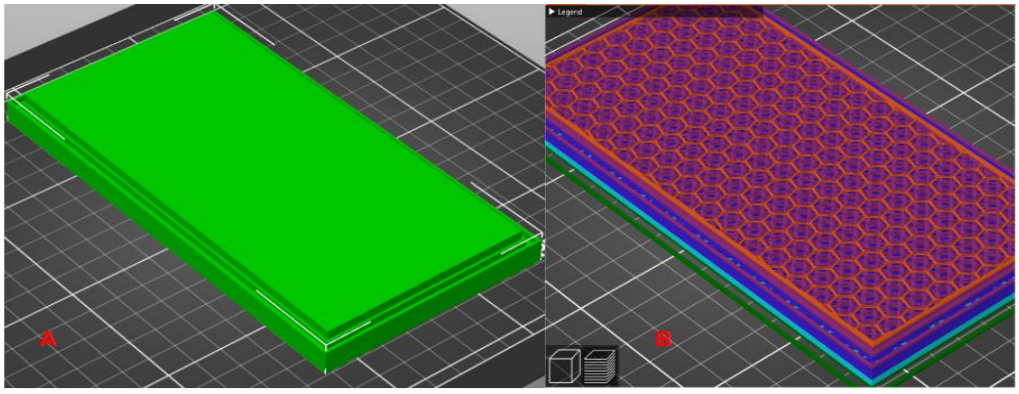

Figure 54 - Cover: A - Full cover geometry; B - Honeycomb gradient for the middle layers of the part.

The base and the cover were assembled manually with the cover positioned on top ofthe base. Regarding the materials used, for the base the following sequence was applied: firstlayer was produced in natural TPU (figure 54, D), and the remaining layers were done with CB/TPU (figure 54, B); The cover was made of natural TPU, and there were five layers. The honeycomb patterned layers were made of CB/TPU. The lateral walls were also made of honeycomb, produced in CB/TPU. The final solid layer was also made of CB/TPU. You can see the honeycomb lateral walls in figure 54, A.

Regarding the size of the part and layers' thickness, both for the case and cover, Figure 55 and Figure 56 exhibit the relevant dimensions.

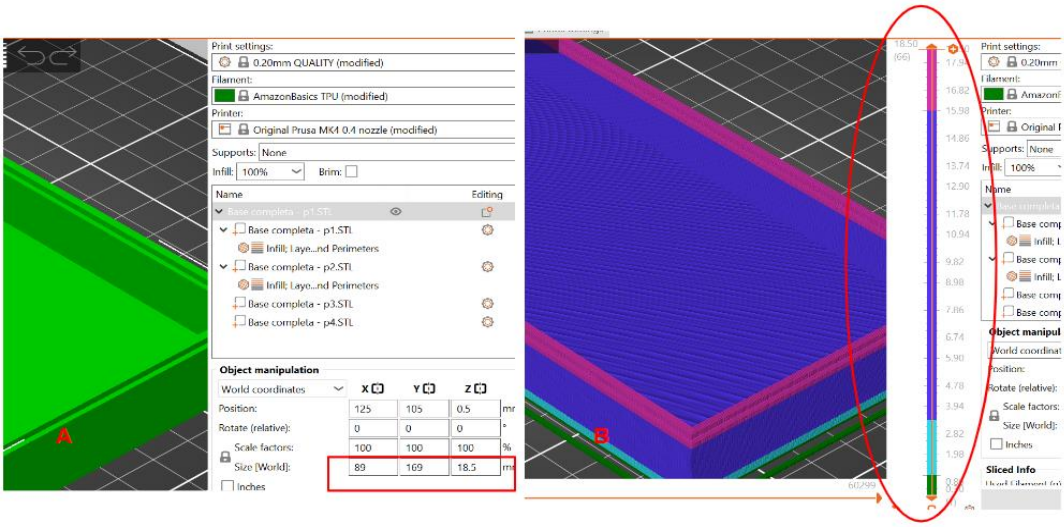

Figure 55 - Base dimensions (mm) and layers' division: A - Part dimensions; B - Layers' thickness.

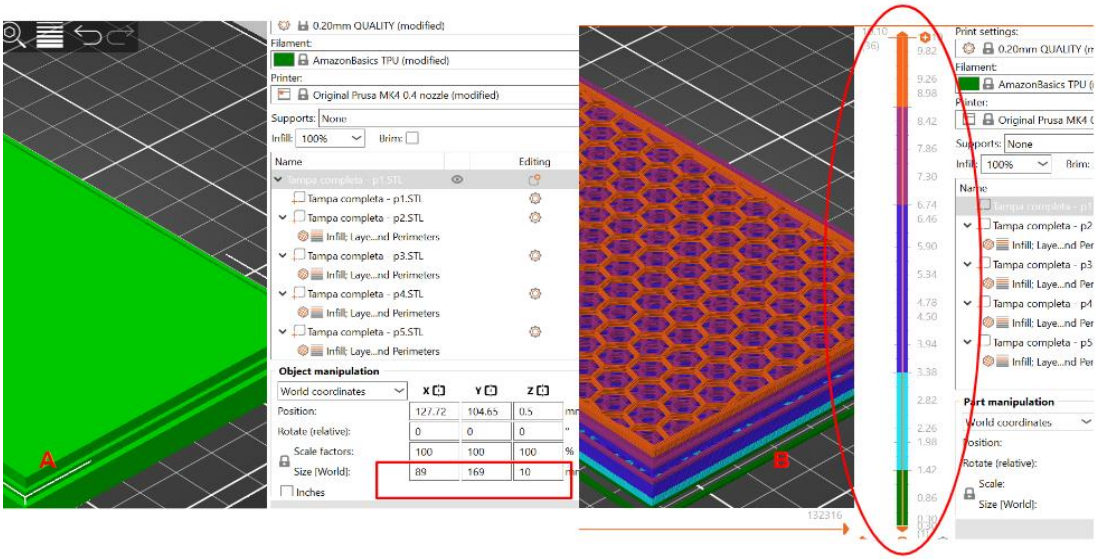

Figure 56 - Base dimensions (mm) and layers' division: A - Part dimensions; B - Layers' thickness.

4. Results and Discussion

4.1 Filament's Characterization

4.1.1 FTIR

Figure 57 shows the FTIR spectra of TPU and CB/TPU in the range of 1800 to 650 cm^{-1}. The absorption bands in 1726 and 1696 cm^{-1} (peeks 1 and 2) are assigned to the free and bonded carboxyl groups, respectively. The absorption bands at 1595 and 1415 (peeks 3 and 4) cm^{-1} are attributed to the phenyl groups, while the characteristic bands assigned to the (C-O-C) are observed at 1169, 1140 and 1068 cm^{-1} (peeks 8 and 10). As shown in Figure 57, both spectra are similar, mainly below 1100 cm^{-1}. However, a shift of the bands attributed to the carboxyl and (C-O-C) groups in the spectrum of CB/TPU filament are evidenced, probably due to the specific interaction with the function groups of the conductive filler. The findings analyzed in the spectra of both filaments reveal that the TPU used in this study is based on ester. According to the literature, the main characteristic absorption bands of TPU based on ester show a simultaneously contribution of hard and soft segments. Absorption bands of hard segments are related to the functional groups of urethanes and/or phenyl groups, while the soft segments are composed of (CH_2) and ester (C-O-C) groups. Table 7 summarizes the main absorption bands attributed to the specific functional groups in the spectra of both TPU filaments (Wang et al., 2002) (Lee et al., 2009) (Tian et al., 2016) (Haryńska et al., 2020) (Yilgor et al., 2006) (Theiler et al., 2018) (Petcharoen & Sirivat, 2013) (Y. W. Deng et al., 1994) (Kasprzyk & Datta, 2018).

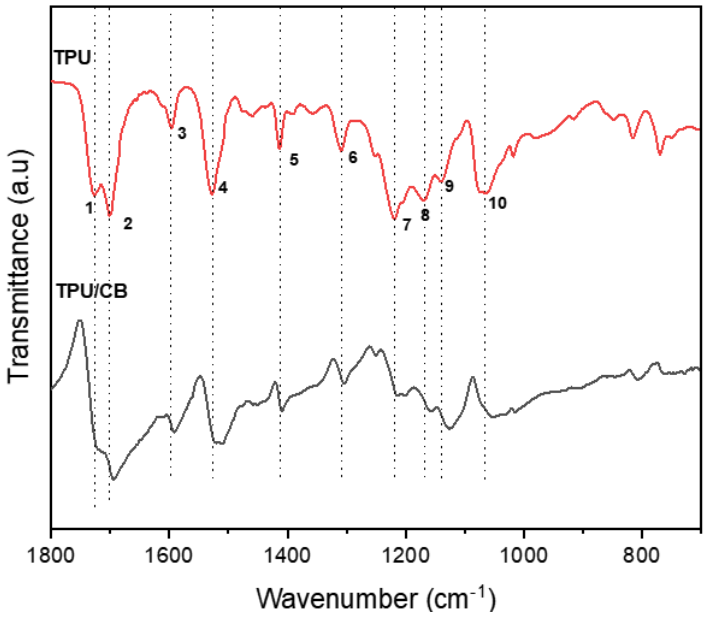

Figure 57 – FTIR-ATR spectra for TPU and CB/TPU.

Table 7 - The characteristic absorption bands associated with function groups of TPU filaments.

Peak	Wavenumber (cm^{-1})	Functional group assigned
1	1726	*v* (C=O), free
2	1696	*v* (C=O), H-bonded
3	1595	phenyl ring + *δ*(N-H), H-bonded
4	1528	*v* (C-N) + *δ* (N-H)
5	1415	phenyl ring
6	1308	*v* (C-N) + *δ* (N-H), free
7	1219	*v* (C-N) + *δ* (N-H), free
8	1169	*v* (C-O-C), H-bonded
9	1140	*v* (C-O-C), free
10	1068	*v* (C-O-C), H-bonded

4.1.2 SEM of the Feedstock Filament Segments

Figure 58 shows the SEM micrographs retrieved of the fractured filaments. Filament A and B are the natural TPU and CB/TPU filament segments respectively. In both filaments lack of pores and absence of defects are observed. Figure 58 (c) and (d) exhibit the fracture surface with more detail, highlighting the roughness of the filament B. Figure 58 (e) and (f) show a clear distinction between the two samples. Filament A presents a smooth surface while filament B exhibits particle aggregates that are dispersed evenly throughout its surface, corresponding to the carbonaceous filler, CB, present in the CB/TPU matrix. Jung & Lee (2023) obtained similar results with respect to the morphology of the CB/TPU filament cross-section upon analysis of the CB/TPU filament derived from FilaFlex. This underscores the consistency of the observed structural characteristics across different samples of CB/TPU.

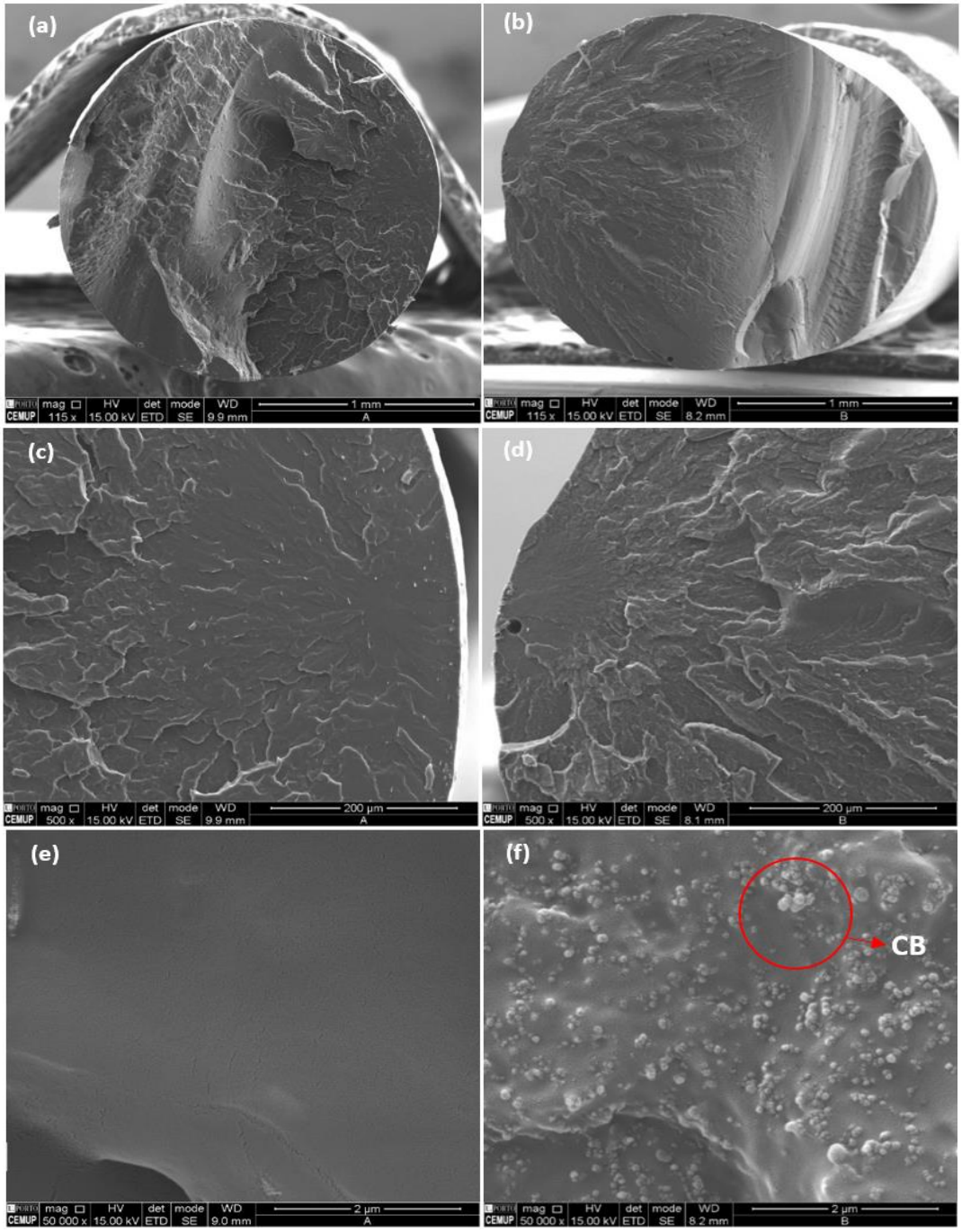

Figure 58 - Fracture surface of filament A and B at different magnifications: (a) - Filament A 115x; (b) - Filament B 115x; (c) - Filament A 500x; (d) - Filament B 500x; (e) - Filament A 50 000x; (f) - Filament B 50 000x.

4.2 Printing Configuration Optimization

As mentioned in chapter 3.4, the first step of the practical work was the definition of the optimal first layer calibration. At this moment the printer was used in its default state, meaning that initially no changes were made regarding its components. Figure 59 illustrates the successive calibrations performed to reach its optimal value. It was used as a starting point, the value -1.000. This value was recommended by a doctoral student that had experience with this printer. The use of hair spray to enhance the adherence of the strand of filament to the bed was also considered.

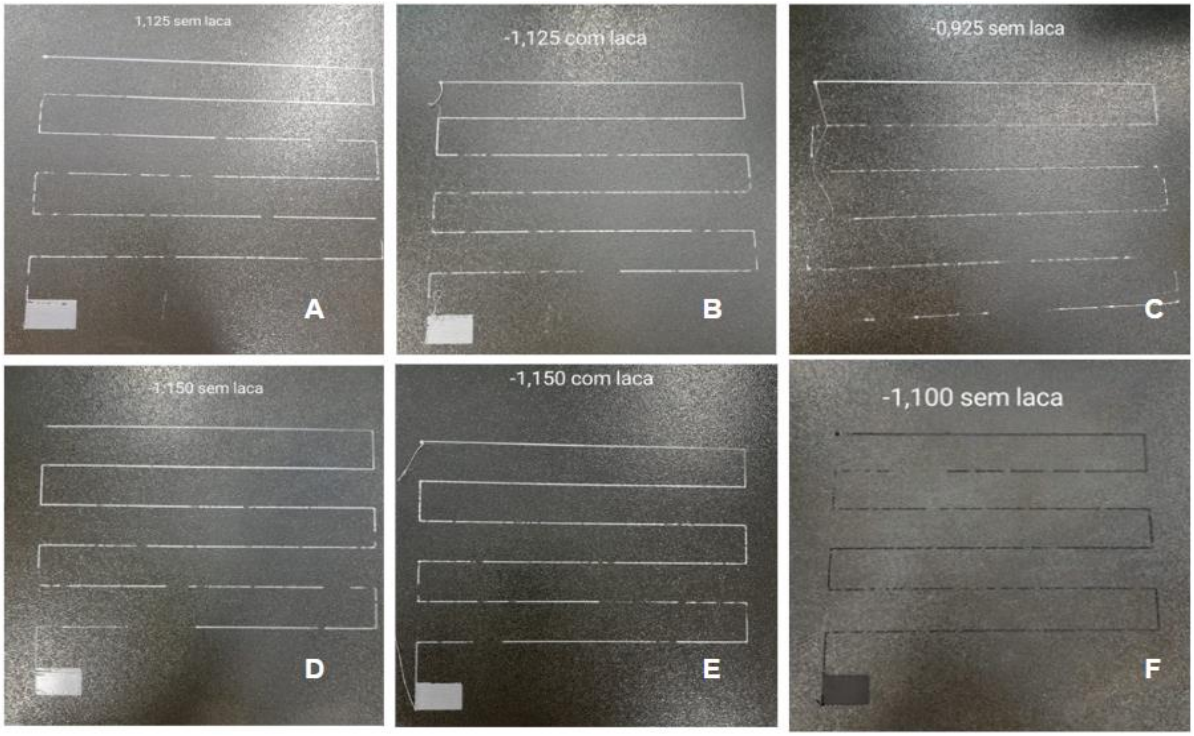

Figure 59 - First layer calibration approximations: A: -1,125 without hair spray; B: -1,125 with hair spray; C: -0,925 without hair spray; D: -1,150 without hair spray; E: -1,150 with hair spray; F: -1,100 without hair spray.

Considering the fabrication of multi-material components, the process of optimizing the first layer calibration was executed with both filaments, with priority to the natural TPU, since there is more data referring to this filament, for comparative purposes. The use of hair spray didn't appear to have a relevant effect on the first layer quality. The result shown in Figure 60 was the best regarding the starting conditions of the machine. Although the deposition of the strand of filament is not continuous, this was initially attributed to the flexibility of the filaments and highly viscous characteristics and not due to poor calibration.

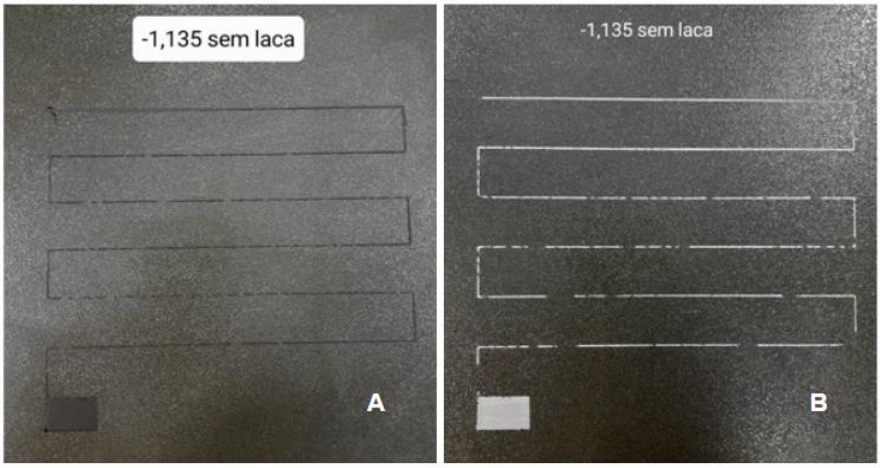

Figure 60 - Optimal first layer calibration: A: -1,135 without hair spray in natural TPU; B: -1,135 without hair spray in CB/TPU.

4.2.1 Calibration Cubes Version 1

The first layer calibration was followed by the printing of the calibration cubes to optimize the printing parameterization. The first iteration of the printing configuration is shown in Table 8 - Printing parameters of the first calibration cubes, version 1.1. and the cubes produced are shown in Figure 61. The surface quality of the cubes, by visual inspection, was found to be good with absence of defects and clear shape deviations.

Table 8 - Printing parameters of the first calibration cubes, version 1.1.

Infill Speed (mm/s)	35
Infill Angle (degrees)	45
Perimeter Speed (mm/s)	20
Skirt	3 laps
Infill Density	100 %
Layer Thickness (mm)	0,2
Perimeter	3
Extrusion Multiplier	1
Nozzle Temperature (ºC)	225
Bed Temperature (ºC)	60

To print the cubes using the CB/TPU, the extrusion multiplier value was altered to 1,1 to compensate the lower material extrusion flow rate, considering the less-than-optimal rheological properties of CB/TPU (Nijdam et al., 2022).

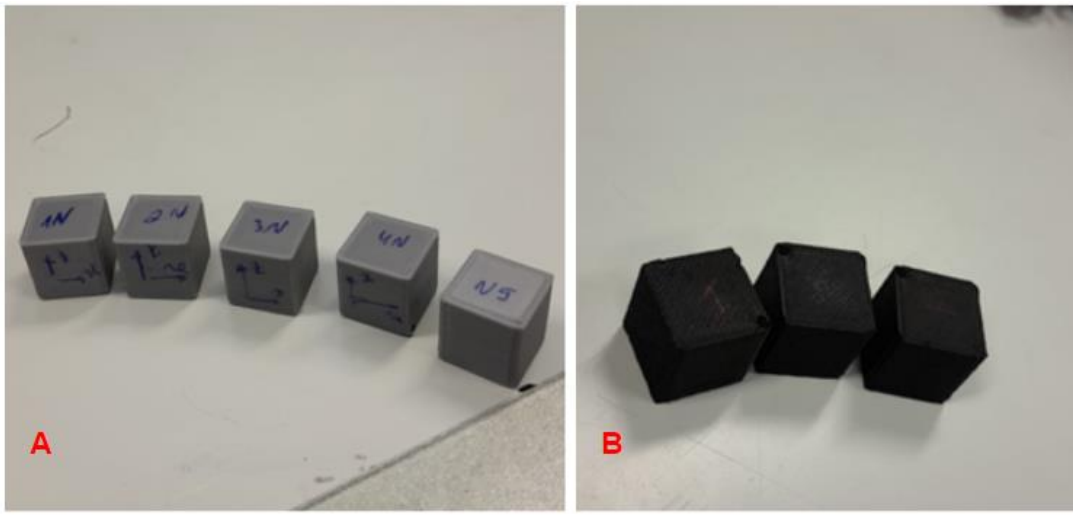

Figure 61 - Calibration cubes version 1.1: A - Natural TPU samples; B - CB/TPU samples.

The mass was measured once for each cube and each dimension measured three times along the cubes' edges. Table 9 shows the data regarding the natural TPU specimens, being that the first criteria of acceptance of the configuration is CV < 10%.

Table 9 - Dimensional Statistical Analysis of the natural TPU calibration cubes version 1.1.

Axis	**x**	**y**	**z**
Average (mm)	14,98	15,02	15,00
Standard Deviation (mm)	0,01	0,01	0,01
CV (%)	0,07	0,10	0,11

In the case of the cubes produced in CB/TPU the y edge dimension of the fourth sample was far from the theoretical value of 15 mm, (-0,15 mm). The problem persisted while printing other cubes to complete the set. Because of this issue and the time available, another change in parameters was made before the completion of this section, being that only three samples of CB/TPU in the initial configuration were printed. Their statistical analysis is shown in Table 10.

Table 10 - Dimensional Statistical Analysis of the CB/TPU calibration cubes version 1.1.

Axis	**x**	**y**	**z**
Average (mm)	14,99	15,01	14,99
Standard Deviation (mm)	0,01	0,01	0,03
CV (%)	0,03	0,09	0,18

Table 11 shows the average mass of the cube's version 1.1 and the theoretical value, showing only a small difference between the two.

Table 11 - Calibration cubes version 1.1 mass analysis.

Material	TPU	CB/TPU
Average (g)	3,94	4,26
Theoretical value (g)	4,08	4,49

Considering the problem referenced above, it was decided to first achieve a good printing calibration for the CB/TPU and then print a set of 5 samples in natural TPU, since it was found that the printability of the former was less reliable and constant than the latter. The value of the extrusion multiplier was altered to 1,15. Since the y edge dimension seemed to be well under the theoretical value it was expected that increasing the flow of material through the nozzle would overcome this difficulty. The subsequent set of cubes produced was named version 1.2, Figure 62.

Figure 62 - Calibration cubes version 1.2 in CB/TPU.

The same procedure regarding the mass and dimensional analysis was followed and the results can be seen in Table 12 and Table 13.

Table 12 - Dimensional Statistical Analysis of the CB/TPU calibration cubes version 1.2.

Axis	x	y	z
Average (mm)	15,00	15,02	14,89
Standard Deviation (mm)	0,03	0,04	0,02
CV (%)	0,22	0,27	0,15

Table 13 - Calibration cubes in CB/TPU version 1.2 mass analysis.

Material	CB/TPU
Average (g)	4,39
Theoretical Value (g)	4,49

As seen in Figure 62, the overall printing quality was maintained. The statistical analysis showed that the CV was still very close to version 1.1 as well as the mass of the specimens. Similar to the first iteration, by the fourth sample dimensional deviations were observed. Deviations of -0,1 to -0,15 mm in the z axis were observed. This persisted and the configuration used was abandoned, meaning that only 4 samples of this version were printed.

This time the nozzle temperature was increased to 230 ºC to facilitate the filament flow, reducing the viscosity to achieve the desired dimensions. One cube of natural TPU and two of CB/TPU were produced. Instantly the results were poor and the execution of the rest of the samples was aborted.

4.2.2 Calibration Cubes Version 2

Throughout the first stage of the printing calibration, successive clogging of the nozzle with buckling of the filament in the gears of the extruder was a typical occurrence. Together with the lack of positive results derived from the previous configurations, these results suggested a possible deterioration of extrusion-related components of the printer. Therefore, the brass nozzle was replaced with a new one. The first layer calibration was maintained, and the results obtained are depicted in Figure 63.

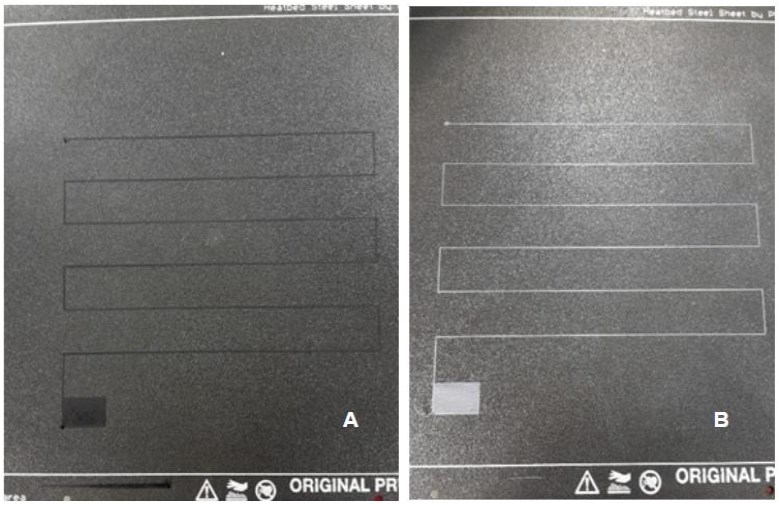

Figure 63 - Optimal first layer calibration with new brass nozzle: A: -1,135 without hair spray in CB/TPU; B: -1,135 without hair spray in natural TPU.

Comparing Figure 60, section 4.2, with Figure 63 it is clear that the continuity of the deposited strand improved significantly, validating that the old nozzle was negatively impacting the printing outcome.

For the printing of the calibration cubes, the parameters shown in Table 14 were used. The infill speed and perimeter speed values were lowered, and the temperature was increased to assure a more accurate deposition due to the TPU's viscous behavior. Two sets of five samples for each filament were produced with little to no variability in printing difficulty and challenges, Figure 64.

Table 14 - Printing parameters of the calibration cubes, version 2.

Infill Speed (mm/s)	15
Perimeter Speed (mm/s)	20
Skirt	3
Infill Density (%)	100
Layer Thickness (mm)	0,2
First Layer Thickness (mm)	0,3
Perimeter	3
Extrusion Multiplier	1,15
Nozzle Temperature (°C)	230
Bed Temperature (°C)	60

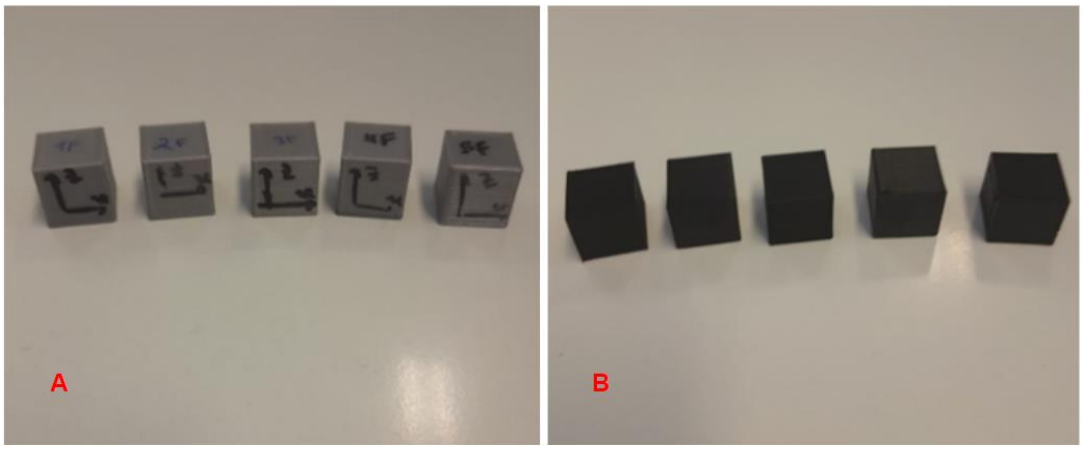

Figure 64 - Calibration cubes version 2 : A - Natural TPU samples; B – CB/TPU samples.

The statistical analysis identical to the one performed in section 4.2.1 is summarized in Table 15 and Table 16.

Table 15 - Dimensional Statistical Analysis of the natural and CB/TPU calibration cubes version 2**.**

Material	**Natural TPU**			**CB/TPU**		
Axis	**x**	**y**	**z**	**x**	**y**	**z**
Average (mm)	14,91	14,93	15,05	15,00	15,03	15,02
Standard Deviation (mm)	0,02	0,04	0,03	0,03	0,03	0,01
CV (%)	0,16	0,29	0,19	0,17	0,18	0,07

Table 16 - Calibration cubes version 2 mass analysis.

Material	**Natural TPU**	**CB/TPU**
Average (g)	3,92	4,31
Theoretical Value (g)	4,08	4,49

The deviations in dimensions were high. Despite the good surface quality and low roughness of the parts seen by visual inspection, in comparison with previous versions of the calibration parts, the shape of the specimens presented a thermal warp designated in the literature as “elephant foot”, Figure 65, a typical defect present in structures produced with FFF (Binder et al., 2022).

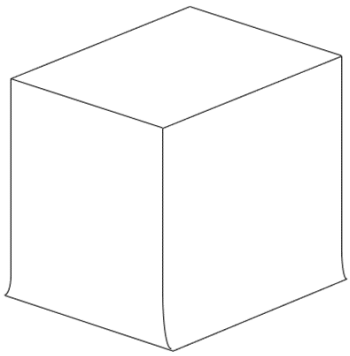

Figure 65 - Elephant foot defect on a cubic FFF part model.

The dilation on the initial layers of the part can be attributed to a thermal gradient generated during printing. This behavior is assigned to the higher nozzle temperatures and lower printing speed, causing longer printing time and longer exposure time of the bottom layers to the bed while the upper layers cool down and contract. The first layer calibration in

this phase may have also contributed to the excessive squeezing of the strands of filament during the printing of the base of the piece, leading to dilated initial layers.

The dimension deviation was also studied along the x and y axis, the affected edges of the part. Despite acceptable results seen in Table 15, regarding the average measurements of different samples, the variance in size of the edges in each sample present a deviation up to 0,13 mm along the y axis for more than one sample and up to 0,12 mm along the x axis.

4.2.3 Configuration Adjustments

As stated before, it was possible to achieve the successful printing of all the required samples. However, it was observed that extrusion path clogging and filament buckling persisted and became more frequent. In order to clean the inner surface of the extrusion channel the nozzle was removed, and PLA was extruded directly from the heating block as a cleaning strategy. The nozzle was mounted again, and it was observed that nothing changed.

The machine appeared to be clogged in various sections due to the uninterrupted use of TPU, particularly the CB/TPU variant, which seemed to be more problematic in this sense. It can be said that the higher viscosity and hardness of the CB/TPU, provided by carbonaceous filler content, decreases the filament fluidity, and creates higher chances for clogging due to the higher spread of material in the inside walls of the printer. Candal et al. (2021) have also observed that TPU/CNT exhibited higher viscosity, particularly at low shear rates, compared to neat TPU. Subsequently this also allows for the buckling of the natural TPU filament. When the former is extruded and encounters remains of CB/TPU in its way, its crossing is blocked. As the natural TPU is more flexible, the force generated by the motor in conjunction with the lower hardness of this filament cannot surpass the obstacles of CB/TPU causing buckling to occur in between the gears of the printer.

Despite this, commercial TPU is noted for its good printability due to additives that reduce viscosity and increase hardness, while 10 wt.% CB/TPU composite, for instance, exhibits similar printability characteristics. Therefore, these filaments can be printed without buckling-related issues. Possibly the filaments purchased do not present a composition as optimal as the one described (Ren et al., 2022).

Further cleaning was carried out. This involved the disassembly of a larger number of printer components. Figure 66 shows the printer used without the nozzle, heating block, temperature sensors and resistance during this stage of the process.

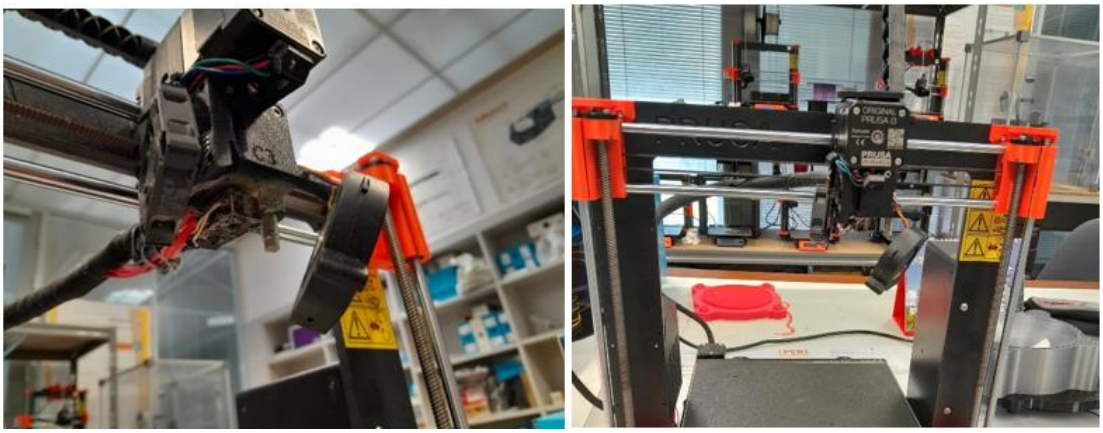

Figure 66 - Prusa i3 MK3S after component removal.

The removal of components was conducted at 280 ºC. Using the tools presented in section 3.2.7, an excess of material filament was extracted from the inner surface of the printer and the other components were cleaned separately.

To prevent further printing difficulties a PLA based cleaning filament (**Error! Reference source not found.**, A) was extruded in between all prints. Furthermore, a new brass nozzle coated with nickel was mounted on the printer, Figure 67. This nozzle is more abrasion resistant and thermally stable. It was expected that this component would better sustain the abrasive action of the particles present in the CB/TPU providing more printing reliability (Khan et al., n.d.).

Figure 67 - Nickel coated brass nozzle.

At this stage, considering that many changes had been made in comparison with the initial settings of the work, it was decided to perform a new first layer calibration and printing configuration calibration. This was, however, not possible since the effect of the new nozzle was not what was expected. The printing quality was very poor in comparison with the ones achieved with brass nozzles, either maintaining the same parametrization used in section 4.2.2 or trying new configurations.

Because of these mishaps, and the time-sensitive nature of the thesis work, a final modification was attempted to solve the existing problems and proceed with the assignment. A new brass nozzle was mounted on the printer, which with the right printing calibration already had proven to produce good results. This was accompanied by the use of the referred cleaning filament between prints as well. A new first layer calibration was executed, Figure 68.

The new optimal value reached for the approximation, -0.800, was key in preventing further nozzle clogging since it allowed for a deposition of the strand of filament with good adherence without excessively squeezing the material onto the bed, as recommended in the Prusa 3i MK3S manual. It is concluded that the first layer calibration used in sections 4.2.1 and 4.2.2 was optimal considering the first nozzle used. After the first substitution of the nozzle in section 4.4.2 a new first layer calibration should have been reached. However, since the initial results related to the printing of the calibration cubes (version 2) were satisfactory, this indicated that a new optimization of the first layer approximation was not required. There was not adequate prevention of printing difficulties related to the printing optimization.

Furthermore, it was concluded that the uninterrupted overuse of the CB/TPU in FFF printing is to be avoided and substituted by an alternate use of different material filaments to clean the extrusion path. Insufficient feed force and low Young's modulus make it difficult to push soft and flexible filaments through the nozzle smoothly. This is aggravated by the presence of CB/TPU sediments (Ren et al., 2022).

Adding to this, it was observed that a correct first layer calibration is a crucial step in optimizing the printing of flexible filaments, since these are more susceptible to buckle induced clogging and this step has a major effect on this occurrence. If the nozzle is too close to the bed when depositing the strand of material, the filament will tend to roll upwards, and the print will be compromised. This is, as stated, even more pronounced when using materials such as TPU and CB/TPU.

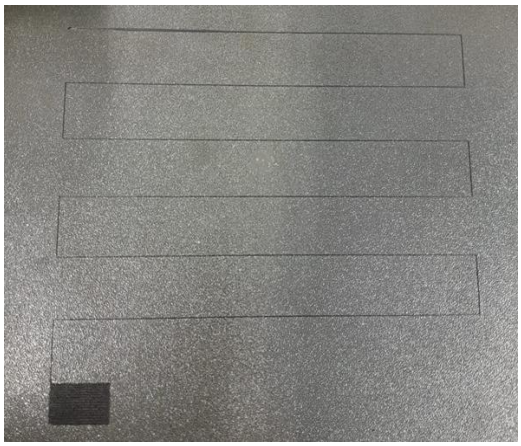

Figure 68 - First layer calibration with a -0.800 approximation, CB/TPU.

The modifications executed and final parametrization achieved in this portion of the project are detailed in Table 17. The layer thickness value was altered to 0,1 mm to improve the reproducibility of the piece's geometry.

Table 17 - Final Printing Configurations.

Nozzle	Brass
Cleaning Filament	PLA used in between prints
First Layer Calibration	-0.800
Skirt	3
Final Printing Parametrization	----------
Infill Speed (mm/s)	15
Perimeter Speed (mm/s)	20
Infill Density	100
First Layer Thickness (mm)	0,3
Layer Thickness (mm)	0,1
Extrusion Multiplier	1,15
Perimeter	3
Nozzle Temperature (°C)	230
Bed Temperature (°C)	60

4.2.4 Calibration Cubes Version 3

Next followed the production of 4 calibration cubes for each filament to validate the iterations performed in section 4.2.3, Figure 69.

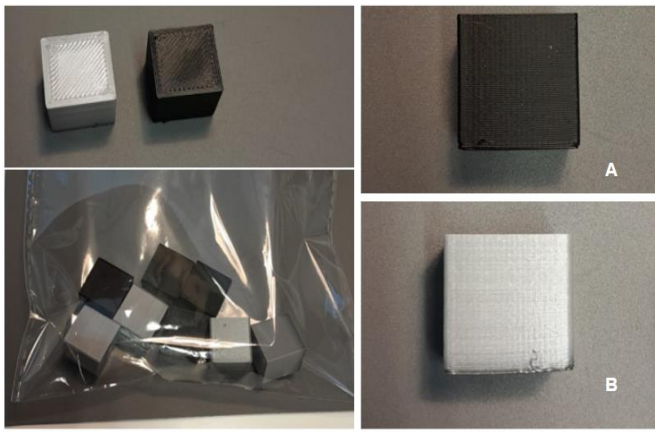

Figure 69 - Calibration cubes version 3: A - CB/TPU sample; B - TPU sample.

The third iteration of the calibration cubes showed great results in terms of surface quality and overall appearance. During the printing of these specimens the clogging problems were reduced to a minimum, which supports the decisions made. The statistical analysis of the mass and dimensions of these samples is presented in Table 18. Some deviations in size between the z and the other axis were detected. However, because the standard deviation and CV are very low, it is concluded that there is very good replicability in the samples. This means that future changes can be made to compensate for the over dilation of the z edge.

Table 18 - Dimensional Statistical Analysis of the natural and CB/TPU calibration cubes version 3.

Material	**Natural TPU**			**CB/TPU**		
Axis	**x**	**y**	**z**	**x**	**y**	**z**
Average (mm)	14,92	14,96	15,09	14,93	14,99	15,16
Standard Deviation (mm)	0,03	0,04	0,05	0,03	0,05	0,02
CV (%)	0,18	0,27	0,30	0,22	0,31	0,11

Positive results were obtained from the mass analysis, with the average mass values of the samples closely matching the theoretical values, Table 19.

Table 19 - Calibration cubes version 3 mass analysis.

Material	**Natural TPU**	**CB/TPU**
Average (g)	3,96	4,27
Theoretical Value (g)	4,08	4,49

The difficulty in transitioning from the CB/TPU to the natural TPU was always present when loading the material to initiate a new print, despite its attenuation by the use of the PLA cleaning filament. As detailed in section 4.2.3, the use of natural TPU after printing with the CB/TPU leads to buckling due to the physical nature of these feedstock materials, even when the printing calibration is optimal. In fact, it was clear that the cleaning filament, while useful, had its limitations. It was observed that the purge executed by removing the CB/TPU with the PLA was incomplete. After a short period of purging, the strand exiting the nozzle became white, indicating that the extrusion path is clear of the CB/TPU. However, when loading the natural TPU to execute further prints, it would be expected that the transition observed from the strand of filament would be of a white color (indicating the presence of the cleaning

filament inside the printer) to a gray one, characteristic of the natural TPU. In fact, the color progressed from white to black and only after a larger time period did it transition to the color of the loaded material. It is concluded that the cleaning filament can be extruded even with CB/TPU sediments present in the extrusion pathway, due to its higher stiffness and lower compatibility with the former. The natural TPU, however, presents much more affinity to CB/TPU and less fluidity. It means that the natural filament must completely push out the excess of its CB/TPU completely to be extruded correctly. Having stated this, the correct purge of the CB/TPU has to be executed primarily with the natural TPU, with the cleaning PLA as a secondary tool.

Furthermore, it was observed that the inversion of the purge produced very different results. When transitioning from either the cleaning filament or the natural TPU to the CB/TPU, this change occurred almost instantly and without buckling or clogging. It is recommended that when printing multi-material parts or successive parts with these filaments, the standard TPU should be used first and then the filler added TPU, to prevent defects, print delays and incomplete printings.

The final calibration samples produced exhibited a slight deviation in shape. The first layers of the parts are rounded, Figure 70. Thermoplastic deposition typically takes place at high temperatures in a setting that causes some deformation and residual stresses to occur while printing. As the outside region cools off more rapidly its contraction leads to peeling off from the bed creating a rounded shape (Duty et al., 2018).

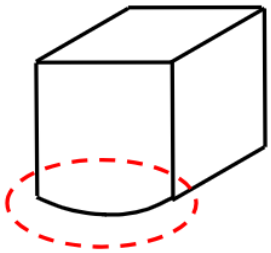

Figure 70 - Rounded base defect on model part.

Regarding the overall printing configurations, it was concluded that, for the TPU 3D printing filaments used, the parameters that most affected the quality of the parts were nozzle temperature and infill speed. 230 ºC and 15 mm/s, respectively, produced the best results after visual inspection and statistical analysis. This is in accordance with literature that mentions, for instance that 230°C was found to be a favorable extrusion temperature for achieving desirable mechanical properties in TPU samples (Gumus et al., 2022)

Another study analyzing the effect of printing parameters on TPU samples verified that for extrusion speeds ranging from 15 mm/s to 30 mm/s defects appeared at higher printing speeds, with dramatic decrease of the mechanical properties. This further suggests 15 mm/s as suitable for printing of TPU (Kasmi et al., 2022).

It was also concluded that the first layer calibration and nozzle deterioration had major effects on the printing success. The former in conjunction with good printing parametrization is key to assure optimal printability, especially when working with flexible thermoplastics, which present high variability in outcome when changing even slightly the printing configuration.

4.2.4.1 Cubes' 3D Scanning Results

4.2.4.1.1 Version 2 Samples

Figure 71 and Figure 72 show the digital images of the samples produced with the version 2 configuration detailed in chapter 4.2.2.

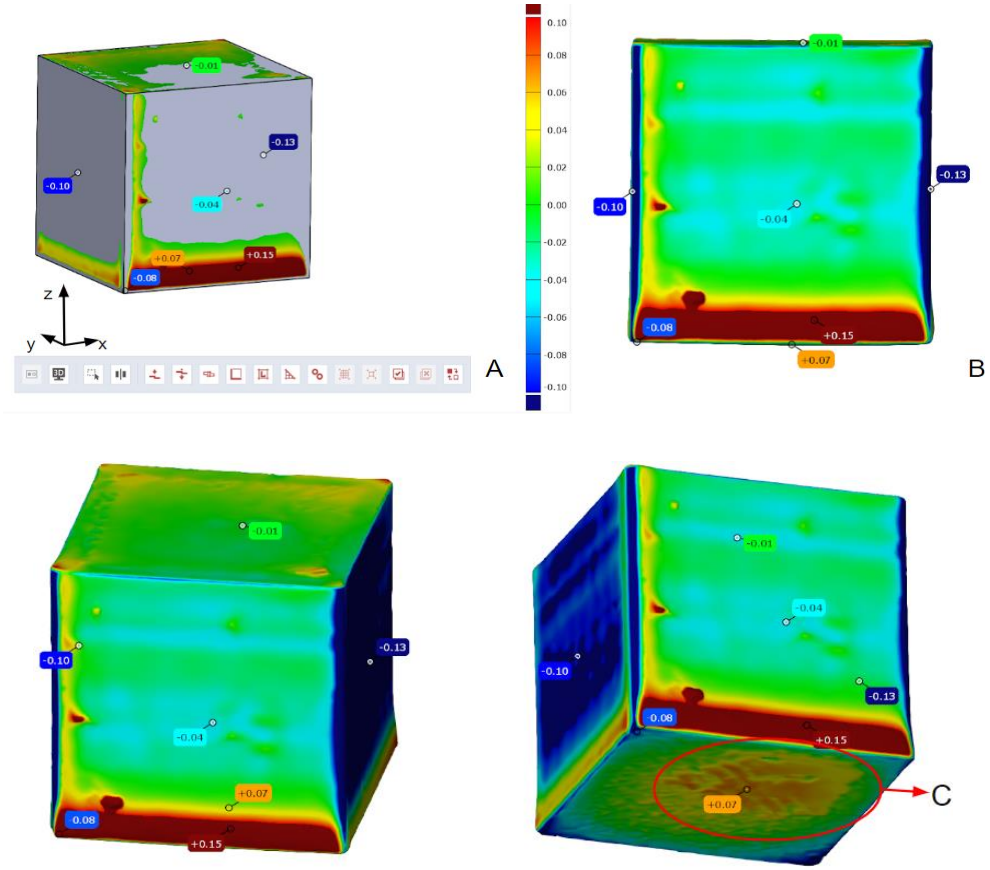

Figure 71 - V2 Natural TPU sample: A - CAD file overlapping the 3D scan file; B - 3D scan file with shape deviations; C - Base defect.

Both the CAD file of the cube and the STL file provided by the 3D scan operation were opened in *GOM Inspect*. To ensure a good analysis, the two geometries had to be aligned. This procedure was executed equally for all the projects. A first automatic pre-alignment was

executed and then a translation was performed. The latter was done considering the positioning of point A of Figure 38 in section 3.4 as well as the respective coordinate system.

Regarding the natural TPU sample chosen of version 2 of the calibration cubes, it is clear by Figure 71 the “elephant foot” defect characterized by a higher expansion (up to + 0.15 mm) of the lower layers and a shrinkage of the sides part (down to -0.13 mm). Both the top and the front and back of the sample have practically no deviation from the theoretical dimensions. The last contact point between the nozzle and the part leaves a mark and a clear over extrusion defect seen on the upper left corner of Figure 71, A. The base defect, Figure 71, C, was caused by a dent in the printer bed. Theoretically the base of the samples should have 0 or negative deviations considering a contraction (seen in the corners of the base of the samples). The middle of the pieces all had, however, a slight dilation corresponding to the area where the dent in the printer bed is located. This will be observed in all the samples further presented.

The sample produced in CB/TPU presented the “elephant foot” defect, although less pronounced. The deviation of the lower base reached + 0,15 mm as the natural TPU sample, but the high contraction of the sides was not observed. The base defect was also less visible although its existence is clear. The part was dimensionally more accurate. The upper surface, Figure 72, B, showcases the defect caused by the nozzle, mentioned above. Its deviation reached + 0,21 mm.

Regarding both samples of version 2 and 3, the corners of the lateral faces of the samples present slight deviations. This is because the nozzle cannot reproduce perpendicular features since the strand of filament deposited is cylindrical in its shape. *Prusa Slicer* constructs the print geometry with rounded corners.

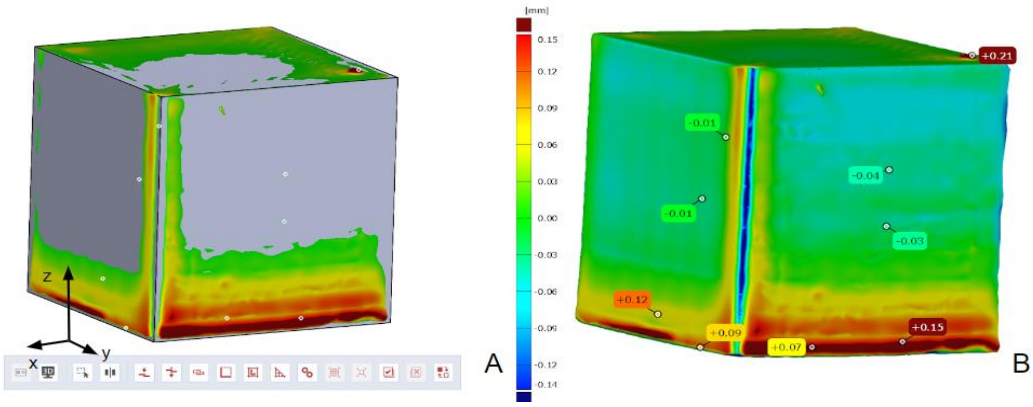

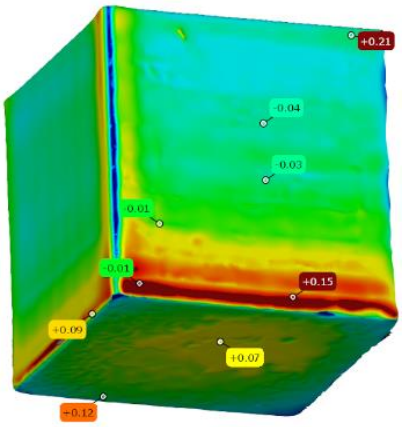

Figure 72 - V2 CB/TPU sample: A - CAD file overlapping the 3D scan file; B - 3D scan file with shape deviations shown.

4.2.4.1.2 Version 3 Samples

Figure 73 and Figure 74 depict the results reached for the samples produced with the final printing configuration reached in section 4.2.4.

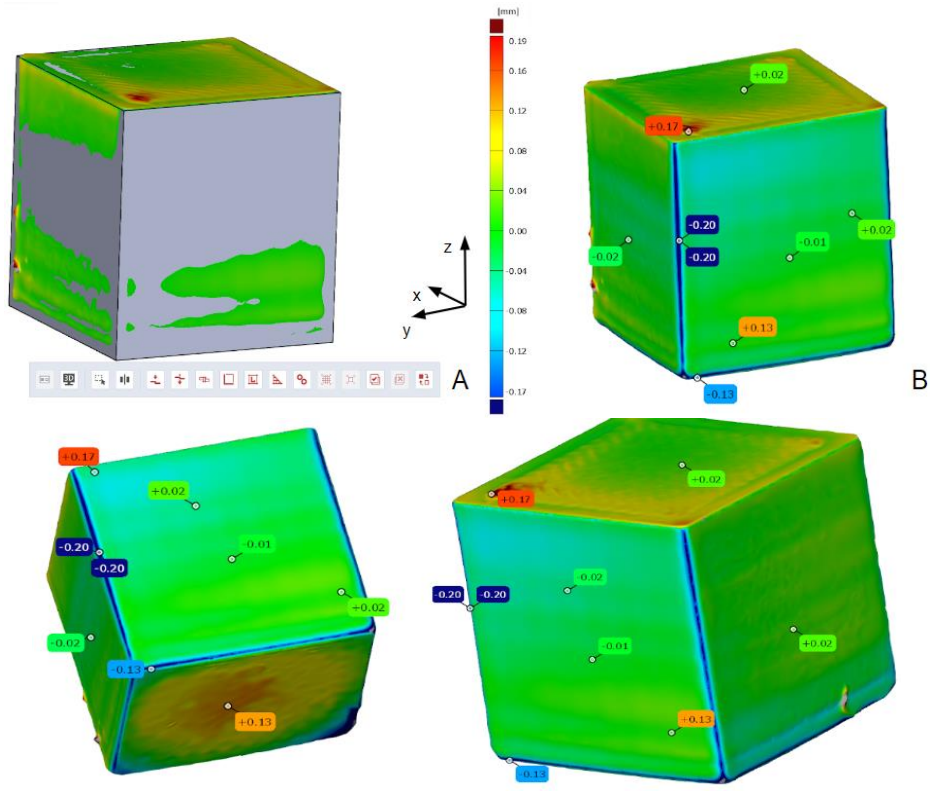

Figure 73 - V3 Natural TPU sample: A - CAD file overlapping the 3D scan file; B - 3D scan file with shape deviations shown.

The samples produced in natural TPU with the final version of the printing calibration present little to no deviations in shape regarding the CAD file. Most surfaces, Figure 72, have minimal digressions. The contact point of the nozzle with the upper surface related defect and the printer bed defect were the only instances that caused size divergences, respectively + 0,17 mm and + 0,13 mm.

It has been noticed that the CB/TPU samples exhibit an overall improvement compared to the previous configuration. There is minimal deviation from the CAD dimensions across all surfaces. However, the same defects noted in the natural samples were observed again, resulting in digressions of +0.15 mm (nozzle contact point) and +0.11 mm (base defect). In this sample however it is clear the thermal warp detailed in section 4.2.4, Figure 74, represented by the blue area in the lower surface of the piece. This shows the contraction of the corners of the base of the specimen, producing rounded edges, with down to - 0,40 mm in the lower right corner.

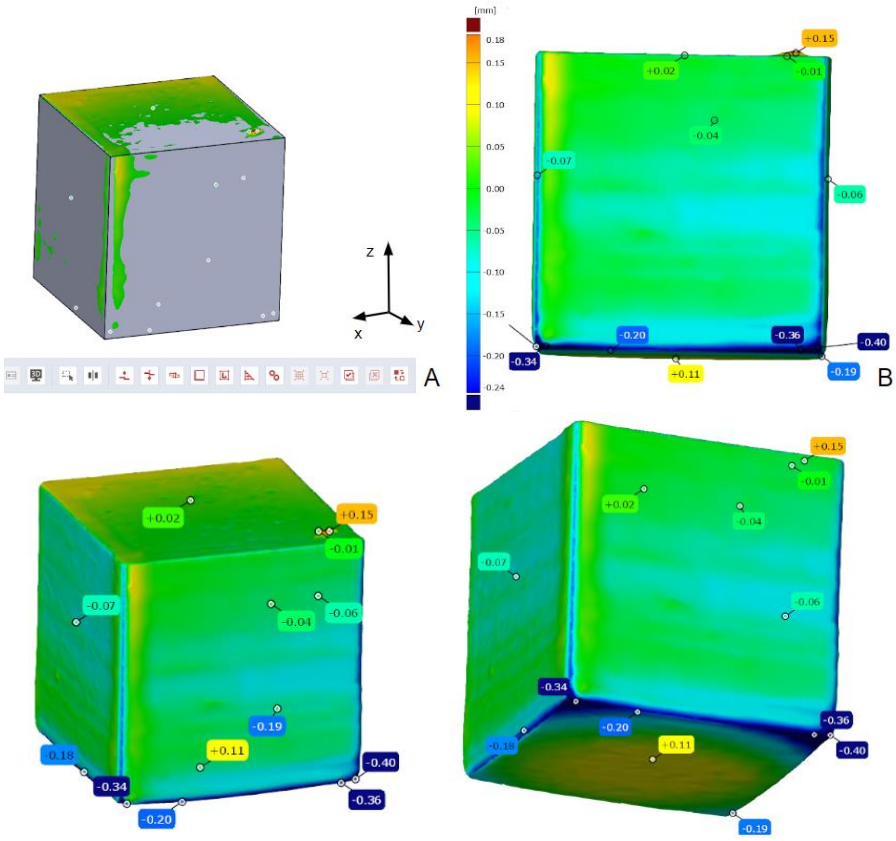

Figure 74 - V3 CB/TPU sample: A - CAD file overlapping the 3D scan file; B - 3D scan file with shape deviations shown.

Overall, the version 3 printing configuration produced optimal results with a clear improvement from its predecessor. The natural TPU sample had a slightly better result regarding its shape and dimensions than its counterpart. Interestingly, the contrary was

observed in a study on interlayer adhesion of TPU and TPU/CNT where Neat TPU exhibited slight warpage in the print bed, which was not observed in the TPU/CNT sample. This absence of warpage in the nanocomposite was attributed by the authors to the presence of CNT nanoparticles, which hindered the entropic contraction motion of polymer chains and increased thermal conductivity, thereby homogenizing temperature (Candal et al., 2021).

4.3 Parametric Study

In order to compare the results from the printing of the samples and the mechanical trials that followed, an evaluation was developed. The samples that were produced via the optimal configuration defined in section 4.2.3 were defined as the standard of comparison in terms of their print quality. Figure 75, Figure 76, and Figure 77 show the “P” samples produced to this extent.

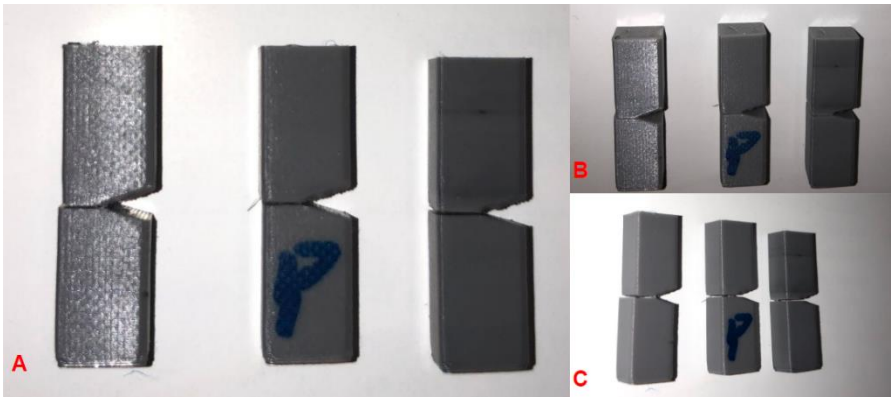

Figure 75 - P_bb samples: A - front view; B – front and top view; C – Front and side view.

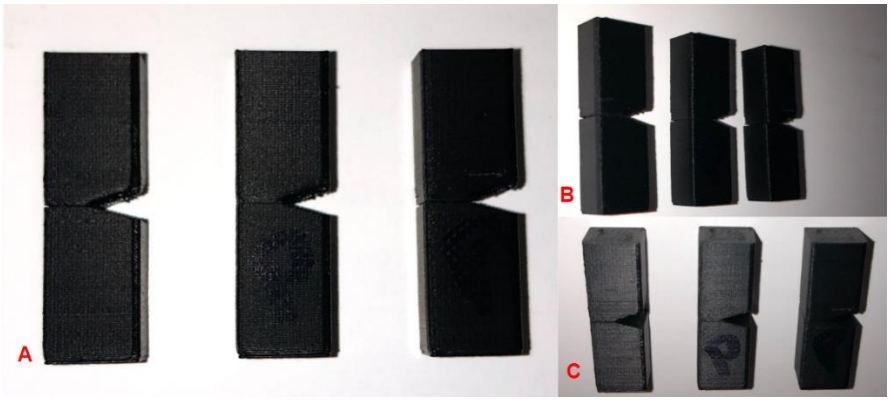

Figure 76 - P_pp samples: A - front view; B – front and top view; C – Front and side view.

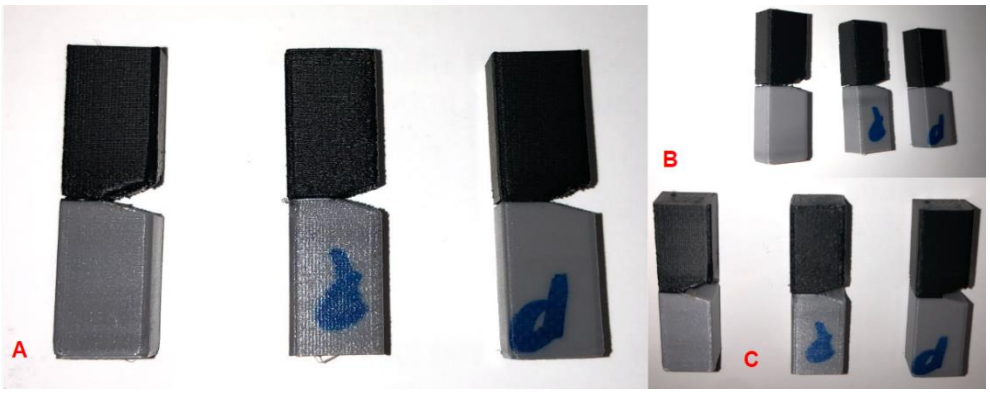

Figure 77 - P_bp samples: A - front view; B – front and top view; C – Front and side view.

The samples were photographed after the fracture and placed as they were printed. The samples presented smooth surface, accurate shape, and good deposition in the interface boundary with absence of defects. Table 20 describes the results of the printed samples related to deposition associated defects. Figure 78 shows the images of the defects mentioned present in samples with poor quality.

Table 20 - Defects present in the samples produced, adapted from (Loh et al., 2020).

Samples	Unable to Print	Inconsistent Extrusion	Poor or Rough Surface	Uneasy Support Removal	Warping
1...16	X				
17					X
18			X		X
19		X	X	X	X
20		X	X	X	
21		X	X	X	
22...24					
25			X		
26		X	X	X	X
27					
28		X			X
29					
30					
31		X			
32		X			

33			X		
34					X
35		X	X	X	X
36		X	X	X	X
37			X		X
38			X		X
39			X		X
40					
41			X	X	X
42			X	X	X
43				X	X
44		X	X	X	X
45					
46					X
47		X	X	X	X
48		X	X	X	X

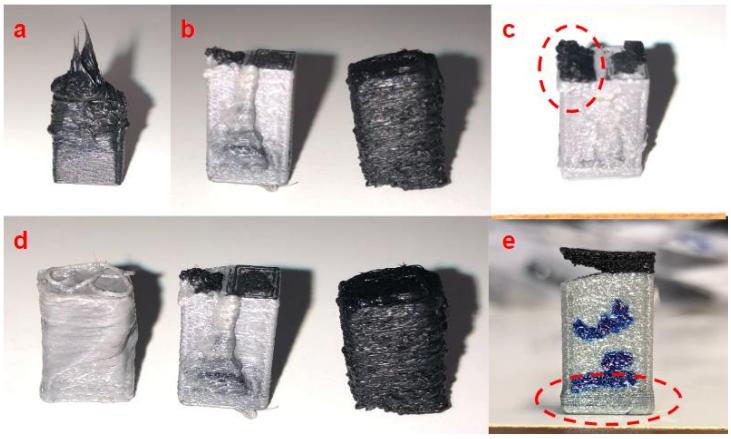

Figure 78 - Printing defects: a – Unable to print, sample 16; b – Poor or rough surface, sample 26; c – Uneasy support removal, sample 44; d – Inconsistent extrusion, samples 26 and 14; e – Warping, sample 34.

The samples that correspond to empty lines in Table 20 didn´t present noticeable defects. Table 21 shows a comparison analysis of the best surface quality of the standard configuration sample with those specimens produced by parametric study. Based on visual inspection the following standard was applied: “G” for good surface quality and “VG” for very good surface quality, the latter being close to indistinguishable from the quality produced by

the configuration of the “P” specimens. Since the parametrization for the natural TPU may not be the optimum for the CB/TPU, two columns will be used to refer to the surface quality of each portion of the sample.

Table 21 - Surface quality of the samples produced by parametric study.

Sample	Surface Quality TPU	Surface Quality CB/TPU
17	VG	G
22	G	G
23	VG	G
24	VG	VG
27	G	G
29	G	VG
30	VG	G
40	G	G
45	G	G

Figure 79 highlights the difference between the quality standard defined in Table 21. The 3D printed sample 27 produced a slightly rougher surface. The surface of sample 24 is more accurate and smoother. The reflection of the light on this area shows a clearer and well-defined geometry. This is more evident comparing the CB/TPU portions of the samples.

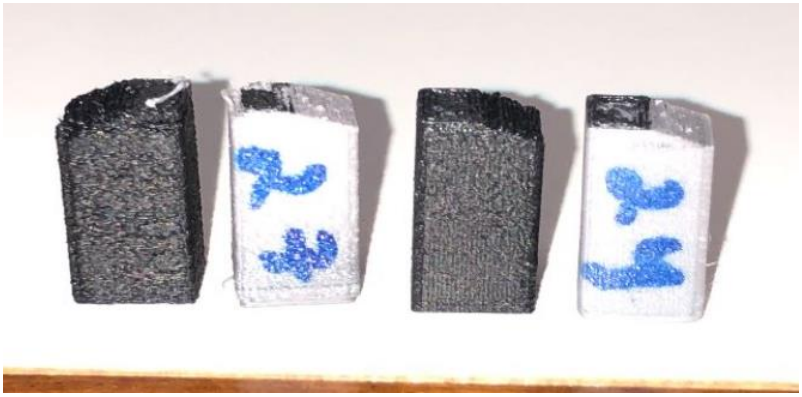

Figure 79 - Good surface quality and very good surface quality respectively, samples 27 and 24 respectively.

4.3.1 Microscopic Analysis

4.3.1.1 Optical Microscopy

Prior to the mechanical trials, samples were selected to be analyzed via optical microscopy. The goal was to obtain detailed images of the outer surface of the samples, as well as the interface region. Figure 80 to Figure 91 show the relevant PNG files retrieved of a few samples of Table 21: 17, 29, 40. The specimen P_bp_1 (natural TPU) was also chosen to be visualized in order to have a benchmark for comparison.

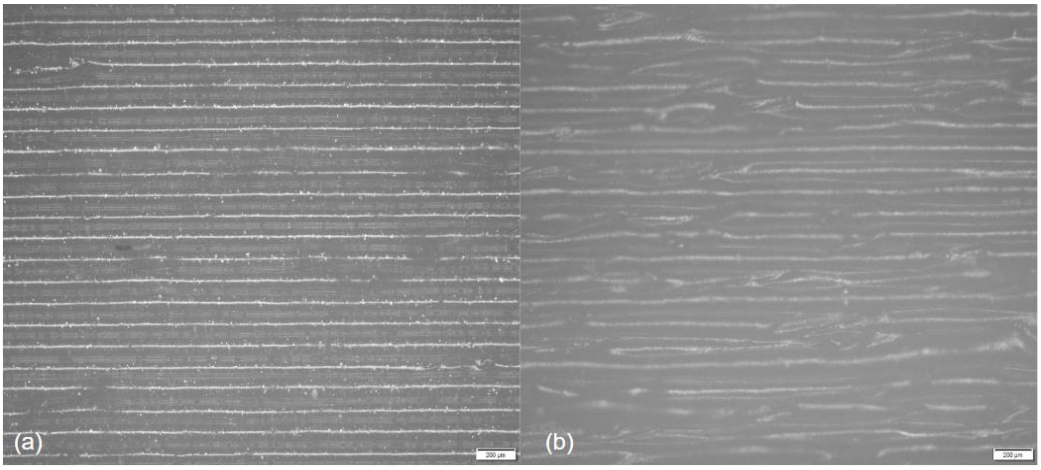

Figure 80 - Sample 17 lateral surface: a – TPU 5x mag; b – CB/TPU 5x mag.

Figure 80 of sample 17 exhibits a clear difference between the printing of natural and CB/TPU. The deposition of the natural strand is much more continuous in size and shape. Figure 82 (b) shows that the rasters of CB/TPU are deposited more irregularly and mixed with one another. The interface boundary in this specimen shows good adherence between the two materials without visible voids and pores. The transition is smooth despite the slight irregularity of the lines in this region, Figure 81.

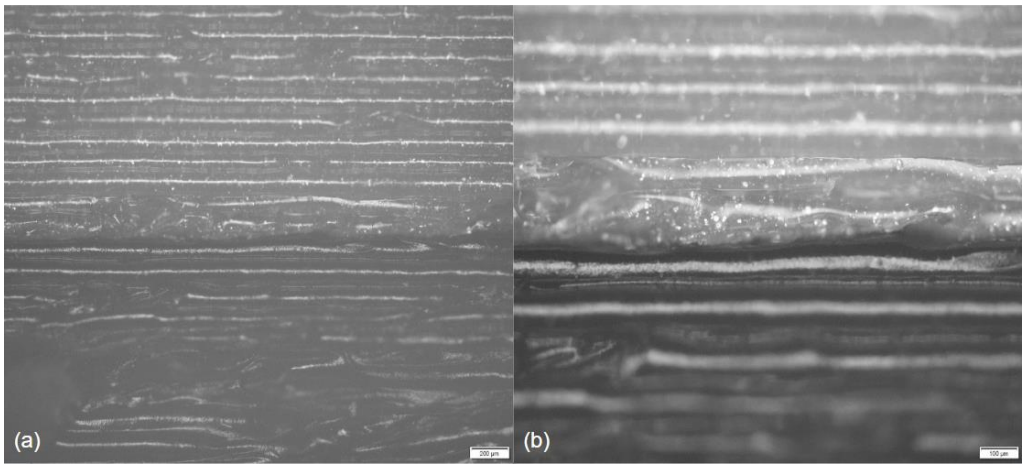

Figure 81 - Sample 17 interface boundary region: a – 5x mag; b – 10x mag.

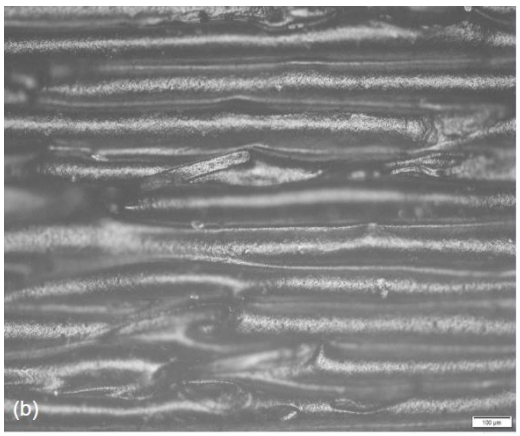

Figure 82 - CB/TPU surface in sample 17, 10x mag.

Figure 83 and Figure 84 of sample 29 show that the deposition of the of CB/TPU layers are more consistent and regular than the natural TPU layers.

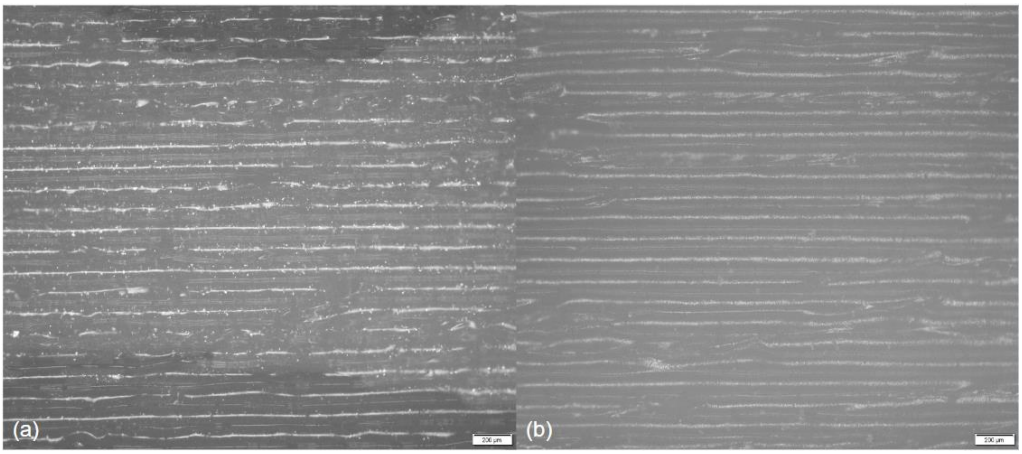

Figure 83 -Sample 29 lateral surface: a – TPU 5x mag; b – CB/TPU 5x mag.

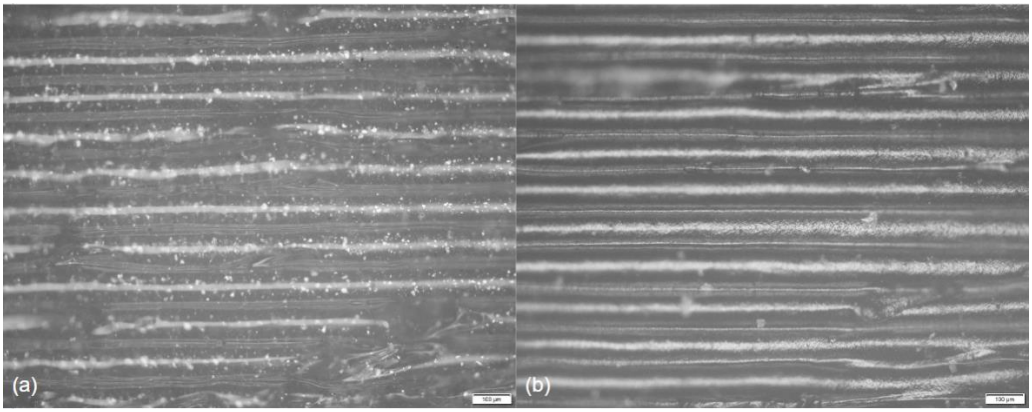

Figure 84 - Sample 29 lateral surface: a – TPU 5x mag; b – CB/TPU 10x mag.

The interface boundary region of sample 29, Figure 85, appears more delimited and clearer than in sample 17. The deposition is smooth, and the transition does not show signs of defects, voids, and lack of adherence.

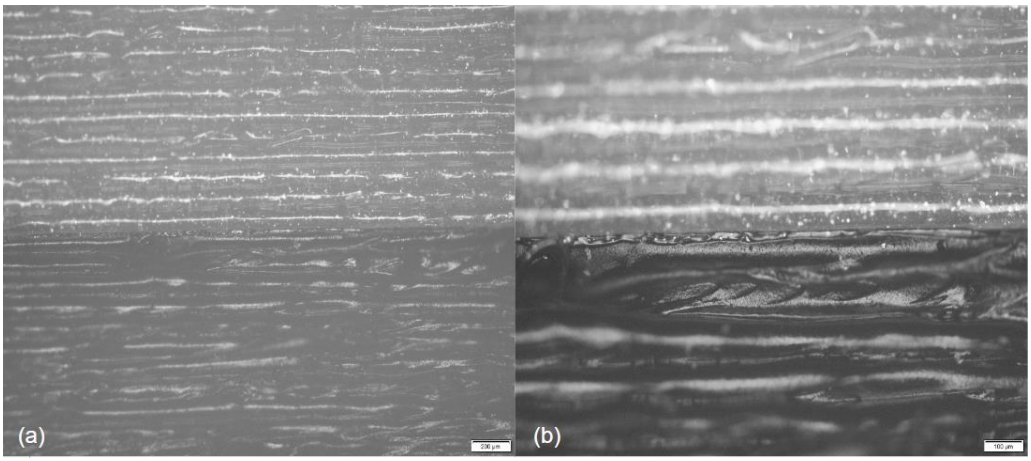

Figure 85 - Sample 29 interface boundary region: a –5x mag; b –10x mag.

In sample 40, Figure 86 and Figure 87 it is observed a similar layer quality in both materials. There is some irregularity, namely, a wave like deposition of the strands of filaments. The interface boundary region, Figure 88, also showcases a smooth transition with no layer deposition imperfections.

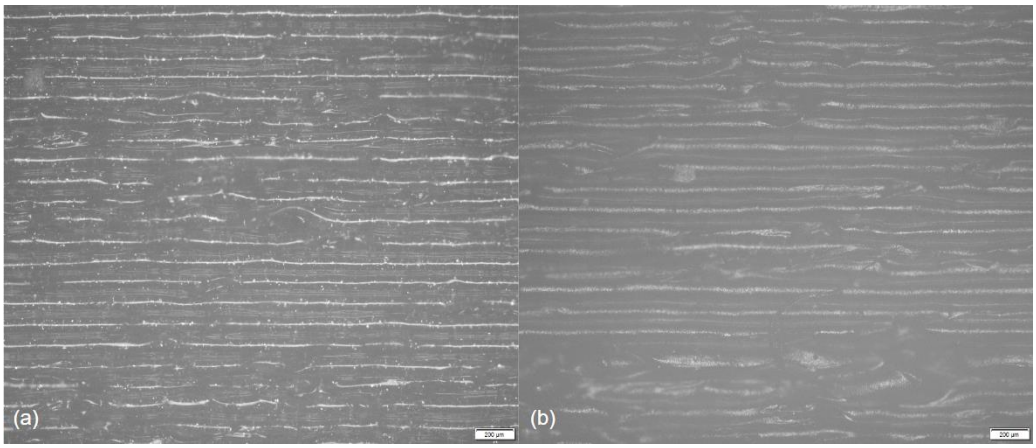

Figure 86 - Sample 40 lateral surface: a – TPU 5x mag; b – CB/TPU 5x mag.

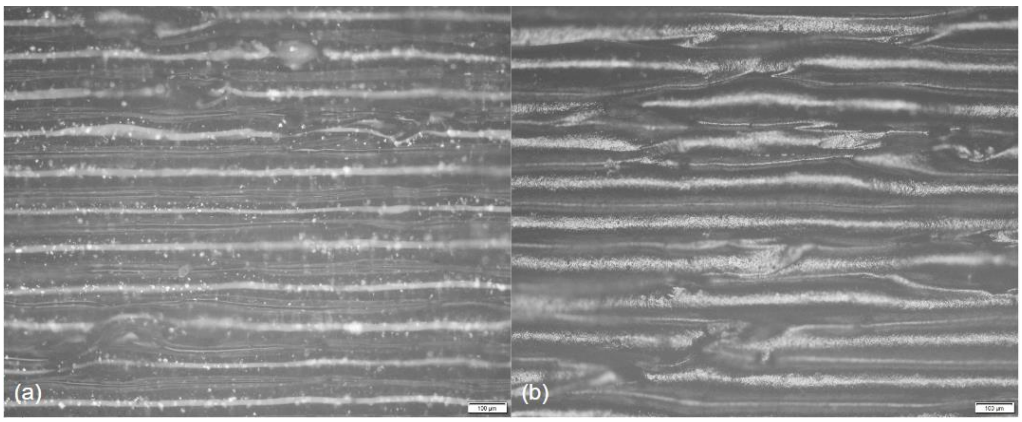

Figure 87 - Sample 40 lateral surface: a – TPU 10x mag; b – CB/TPU 10x mag.

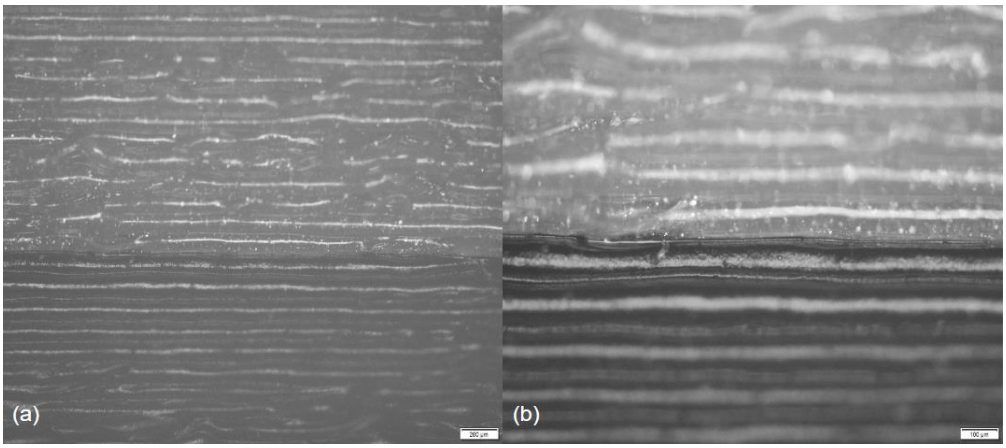

Figure 88 - Sample 40 interface boundary region: a –5x mag; b –10x mag.

Figure 89 and Figure 90 show the lateral surface of the standard configuration sample for both materials. It is clear that the parametrization achieved in the previous chapter produces very good results. For both the natural and CB/TPU the layer deposition quality is the best seen of all the samples. The strands are dimensionally and positionally consistent. The rectilinear pattern is reproduced perfectly in both instances. In a preliminary manner it can be concluded that, with respect to the print quality of TPU and CB/TPU specimens, the

predefined standard configuration is the optimal one. The study of the other samples is, nonetheless, relevant to determine the most influential parameters to the print quality.

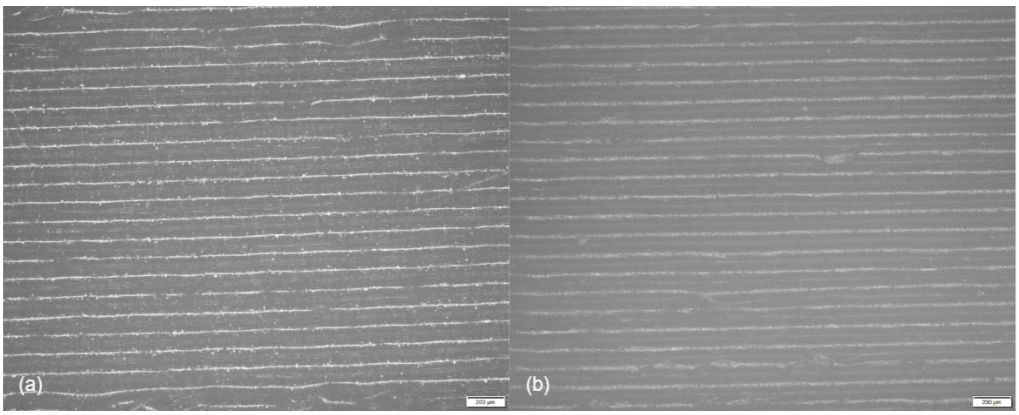

Figure 89 -Sample P_bp_1 lateral surface: a – TPU 5x mag; b – CB/TPU 5x mag.

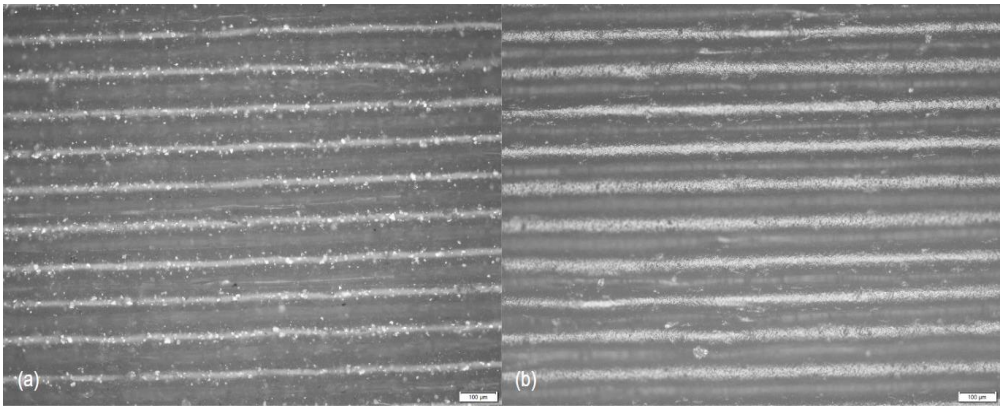

Figure 90 - Sample P_bp_1 lateral surface: a – TPU 10x mag; b – CB/TPU 10x mag.

For all the samples there is a clear distinction in the deposition of the CB/TPU directly on the interface surface following the switch of filaments, and in the upper layers of the sample, Figure 81, Figure 85, Figure 88 and Figure 91. It can be concluded from the microscopic analysis that the extrusion of the CB/TPU progressively improves in quality, being minimal in the interface region, possibly due to temperature and topographic differences and pieces of filament, generated during the switch that are dragged to the region by the nozzle movement. Factors like the drooling of the thermoplastic at high temperatures during the switch can contribute to the poorer quality of the layers in the interface (Lopes et al., 2018).

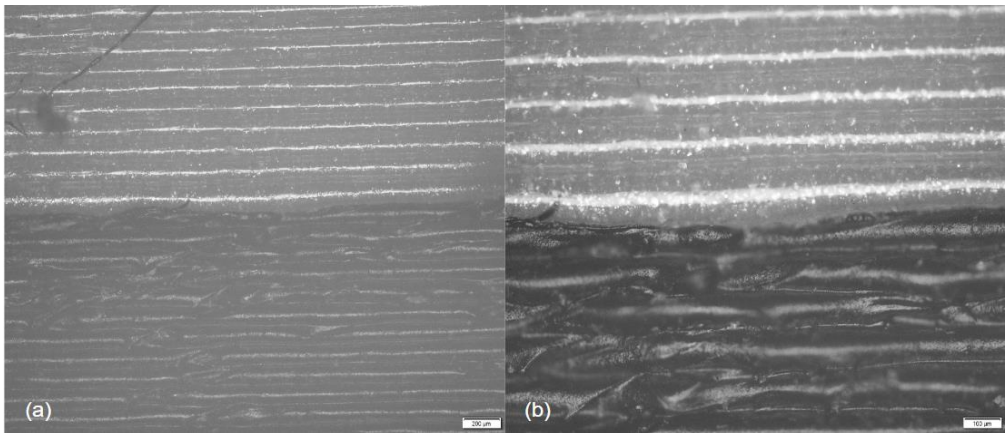

Figure 91 -Sample P_bp_1 interface boundary region: a –5x mag; b –10x mag.

4.3.1.2 SEM

The SEM files reinforce what was observed in the optical microscopy analysis. For the samples referred, the deposition of the layers of filament in the interface region is good, presenting a smooth transition between materials without any clear boundary and adherence difficulties. The standard multi-material sample presents interface quality as good as the standard samples composed of only one material. This highlights the good adhesion between the two feedstock filaments. The interface in samples 29, 40 and 45 also exhibits the quality seen for the samples above mentioned.

It is also observed through this analysis the difference in surface appearance of the CB/TPU and the natural TPU. CB/TPU's strand, Figure 92, is rougher, while the natural TPU's surface is smoother and contains dispersed particles. These are not CB aggregations as the one observed in the CB/TPU filament. They are possibly additives that give the natural feedstock TPU filament its grey color. Lastly, it is also possible the particles are contaminants. The last may have been deposited during the handling of the samples or due to exposure to different elements while in the laboratory.

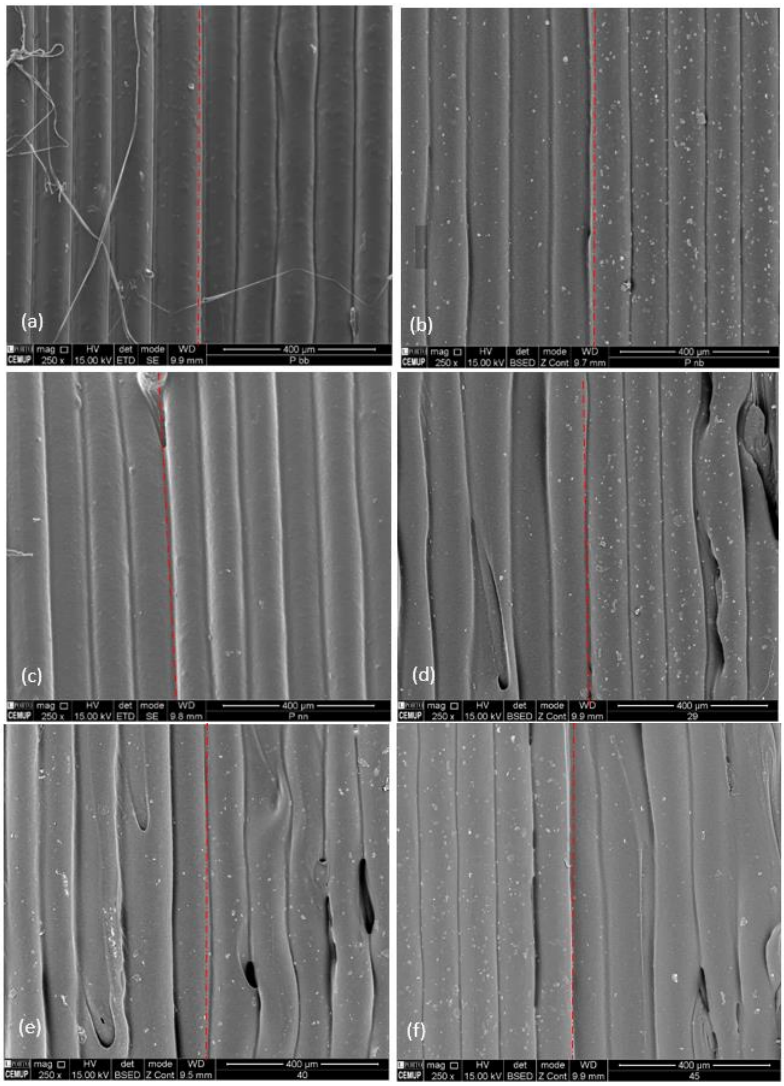

Figure 92 - Samples ' Interface Region MEV images: a - P_bb; b - P_pb; c - P_pp; d - 29; e - 40; f - 45.

4.3.2 Mechanical Testing

Despite the execution of the mechanical trials for all the samples produced regarding the parametric study, only the results of the best samples are presented, as observed in Table 21. The rest of the specimens did not present acceptable printing quality, therefore, the use of their printing configurations for future applications is not recommended. Table 22 shows the max strength and stress and the correspondent values of displacement and deformation retrieved from the pull-out tests. To have a more solid ground for analysis these samples were doubled, and the results correspond to the average values for each configuration. The value for the interface stress was calculated dividing the strength by the surface area of the interface

region (25,5 mm^2). The deformation value was calculated dividing the displacement by the initial unloaded length of the samples, corresponding to the distance between the extremities of the claws of the testing machine (0,88 mm).

Table 22 - Mechanical trials results of the best samples.

Sample	Load (N)	Displacement (mm)	Stress (MPa)	Strain ()
17	164.50	8.25	6.45	9.33
22	231.50	8.01	9.08	9.10
23	152.70	8.60	6.11	9.77
24	184.30	7.91	7.37	8.99
27	133.10	8.18	5.32	9.29
29	179.50	8.35	7.17	9.49
30	171.10	9.01	6.84	10.24
40	149.27	5.31	5.97	6.03
45	196.50	8.60	7.71	9.77

Figure 93 exhibits the representative curves of the mechanical trials performed on the sets of standard samples. Each curve belongs to the test of the sample that produced values for stress closest to the average value of the set of samples defined.

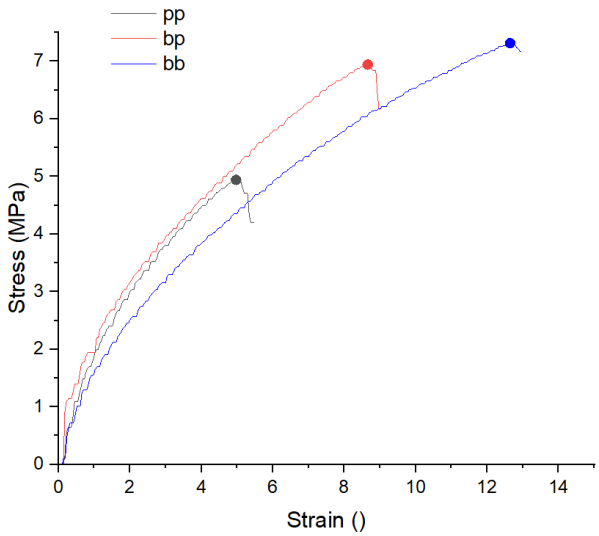

Figure 93 - Stress/Strain representative curves of the standard samples.

The maximum stress values are represented by dots in figure 94 and are, respectively, 126 N and 4,94 MPa for the pp (CB/TPU) sample; 177 N and 6,94 MPa for the bp (multi-material) sample; and 186,5 N and 7,29 MPa for the bb (natural TPU) sample. It is clear that the mechanical behavior of the interface region in the multi-material sample, derived from

the interaction of different materials results in a compromise between these two. The natural TPU is stronger and less rigid than the CB/TPU, possibly due to the addition of the filler that reduces the mechanical properties. Candal et al. (2021) have also observed that TPU/CNT nanocomposite demonstrated lower interlayer adhesion, as measured by the tearing experiment, compared to neat TPU.

This negative impact could be related to the concentration of CB added to the TPU matrix. Halim et al. (2024) observed that increasing the loading of CB led to a decrease in tensile strength and elongation at break of PP/CB composites. Other literature shows that tensile properties of the PVC composites increased up to a certain loading of CB (15 wt. %), and then decreased. This highlights the trade-off between electrical conductivity and mechanical properties in CPCs as influenced by the addition of CB (Islam et al., 2018).

All the samples deformed considerably, due to their flexible nature. The use of a notch enhanced stress concentrations at the interface region and promoted quick failure of the part.

The combination of these specific filaments allows for a mechanical adhesion that is much stronger than in the case of the purely CB/TPU sample. The application of multi-material parts with these filaments is therefore possible regarding interlayer mechanical integrity.

Regarding the values for load and stress in Table 22, the six of the best samples' results were chosen to be compared with the P_bp representative sample, via a graphic analysis, as shown in Figure 94. The curves present the average values of stress for each parametrization. Sample 22 was discarded since the printing of another specimen with this configuration was impossible to execute. This, in conjunction with the high value of interface strength and stress reached (231.5 N and 9.08 MPa respectively) lead to consider sample 22 as an outlier.

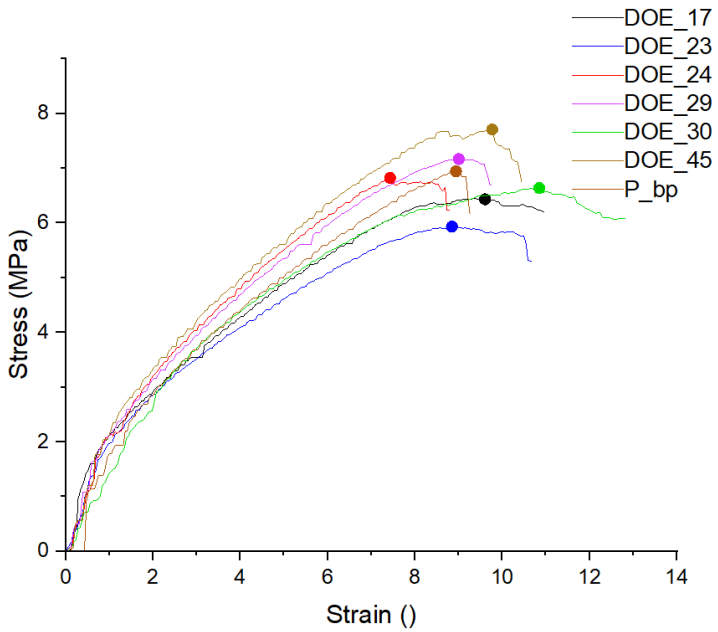

Figure 94 - Stress/Strain curves of the best doe samples vs standard bp sample.

The progression of the stress/strain curves of the samples are very similar between each other and to the standard sample curve. The first slope of the curves represents the elastic behavior of the samples, dominated by the deformation in the regions above and below the interface where the material presents high flexibility. The portion of the curve after the max stress is reached and just before failure occurs corresponds to the progressive pull-out of the interface region. Stress drops slightly since the ability of the notch to withstand the load is rapidly decreased as the material is being torn apart until ultimately the stress drops suddenly when the sample is completely fractured. Sample 45 presented the highest stress value of all the configurations in figure 95. Sample 30 reached the highest value for strain during the test out of the referenced specimens.

Overall, similar strains were obtained to reach the same stresses. The max stress of the samples did not vary excessively. The interface boundary stress average is 6.65 MPa and the average strain is 8.97. Table 23 shows the printing configurations of the samples in figure 95.

Table 23 - Configurations of the samples in graph 2.

Sample	Nozzle Temperature (°C)	Bed Temperature (°C)	Infill Speed (mm/s)	Perimeter Speed (mm/s)	Filament Retraction (mm)	Cooling	Extrusion Multiplier
P_bp	230	60	15	20	1.5	On	1.15
17	230	60	15	10	0	Off	1
23	230	60	15	20	0	Off	1.15
24	230	60	15	20	1.5	Off	1
29	230	90	15	10	0	Off	1
30	230	90	15	10	1.5	Off	1.15
45	245	90	15	10	0	On	1.15

Sample 45 was printed at a temperature of 245 °C, notably higher than the other samples. Despite similar settings to the standard sample, the elevated temperature resulted in the highest stress levels observed. While this could be an outlier, it is possible that the higher temperature allowed for improved deposition and mechanical adhesion between the layers, despite the less-than-perfect surface quality. Cheung & Choi (2023) demonstrated that higher temperature printing of TPU resulted in higher surface roughness, due to over-extrusion causing flow unevenness from the nozzle, according to Freund et al. (2019). A rougher surface is often viewed as a detriment to print quality, but it can actually enhance adhesion by creating better mechanical interlocking between materials.

Sample 24 presents the best surface finish and appearance, while also achieving a stress value which is nearly on par with that of the standard sample. Its configuration closely resembles that of the optimal P_bp sample, with the exception of the cooling and extrusion

multiplier parameters. The slightly better layer deposition and surface quality of the standard specimen could be related to the higher value of extrusion multiplier which causes the nozzle to extrude with more material volume and accurately produce the wanted geometry. Additionally, insufficient cooling can lead to deformation, being crucial maintaining consistent cooling throughout the printing process to create reproducible residual stress in deposited filaments in all layers. The fact that the standard sample had cooling “ON” could be another reason for the difference in surface quality (Nijdam et al., 2022) (Pivar et al., 2022).

Regarding parameters like nozzle temperature and infill speed, the best results were observed for the samples printed at 230 °C and 15 mm/s respectively, in concordance with referenced studies that show similar results (Gumus et al., 2022) (Kasmi et al., 2022).

Bed temperature and filament retraction exert lower effect to the printing quality and mechanical properties since the parts with the best visual appearance and high interface boundary stress did not share a clear correlation in these parameters. However, a parametric study performed trough the printing of TPU cubes shows that lower bed temperatures in natural TPU 3D printed samples contribute to higher dimensional accuracy, with the optimal value determined to be 45 °C. Despite the different filaments used, 95 A in the study and 92 A in the thesis, it can be concluded that bed temperature did not have a significant impact because both values used in the thesis work were above 45 °C (Bhardwaj et al., 2021).

In the work conducted, a discrete interface with no interlocking mechanism was used. The strength of the boundary interface in TPU and CB/TPU parts can be further improved by other strategies such as mechanical interlocking at the interface and continuous gradient interface (García-Collado et al., 2022) (Ribeiro et al., 2019)

It can be concluded that natural TPU and CB/TPU have good adhesion properties. Regarding multi-material flexible joints, Harris et al. (2019) have also demonstrated that TPU exhibits notable adhesion properties, thus rendering it a viable candidate for deployment in multi-material 3D printing applications.

4.3.2.1 Microscopic Analysis of Fractured Samples

Some of the samples were selected to be viewed at the optical microscope to analyze the fracture region. Ideally the fracture would happen directly between the last deposited layer of natural TPU and the first layer of CB/TPU. A significant number of samples printed for the parametric study did not present this fracture type, Figure 95, and thus the mechanical trials of those specimens did not fully represent the interface boundary adhesion.

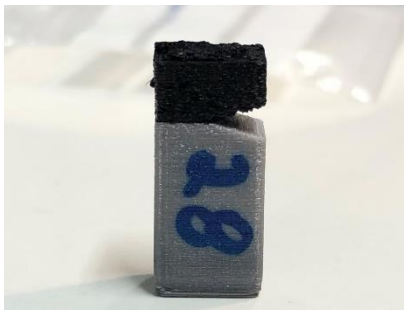

Figure 95 - Fracture occurring above the interface region, sample 28.

Samples P_bp_1, 23, 24, 29, 30, 40, and 45 were analysed. Visually, and mechanically they represent good results. This was consistent with the fracture type they exihbited. The good printing quality, observed by the lack of defects and shape deviations in the parts' structures resulted in a fracture well defined in the interface boundary, Figure 96.

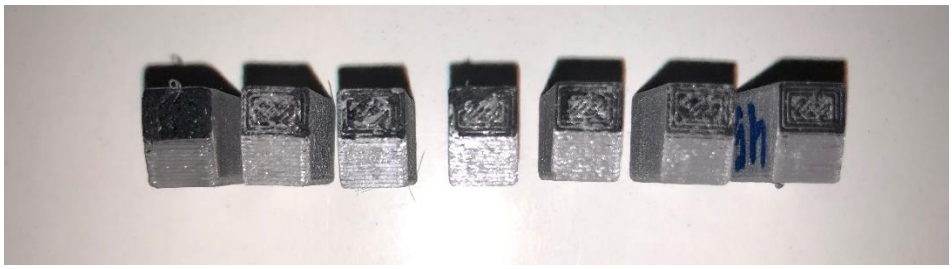

Figure 96 - From left to right: Fracture region of samples P_bp_1, 23, 24, 29, 30, 40, and 45.

A preliminary analysis highights the diference in the fracture region of the standard sample from the others, which are more similar to one another. The optimal printing configuration produces a very high adhesion which promotes fracture always above its area in the CB/TPU layers, a more rigid and fragile surface. This behavior was observed for all the standard bp samples. Considering the rest of the samples, the fracture type was similar. It ocurred in the notch region, altough, generally, it left residues of the CB/TPU filament on its surface. This also showcases the high adhesion between these two type of filaments when printed with suitable parametrization. The construction of the parts also seems to have an effect on the interface fracture. It is obvserved that the constrcution of the perimeter becomes very influential on the surface when the dimensions are decreased. For the samples analysed, the perimeter of CB/TPU is very noticeable on the interface surface, Figure 96. The infill, however, was more easily pulled out since its anysotropic disposition was not favourable considering the perpendicular direction of the loads in action. The perimeter in the interface likely dominated the behavior of the samples during the mechanical trials. It is known that the perimeter improves the structural integrity of parts. However, it is not possible to analyse its influence on the the obtained results. Further interlayer adhesion studies on CB/TPU-TPU samples without perimeter could be conducted (Bruère et al., 2023).

Figure 97 shows micrographs of the fracture region of the standard multi-material sample 1 observed at the optical microscope. Figure 97 is very representative and therefore is the only one exposed. The black sections are the strand of CB/TPU deposited. The perimeter occupies a large surface area of this section, which is not true for the remaining layers of the part. The infill, in 45°, is less present. The ideal fracture would not contain any CB/TPU portions to have a mechanically accurate trial. However, the fracture type observed is the optimal one for the samples tested, and the values for stress and strain retrieved were considered to be a good representation of the interface boundary resistance.

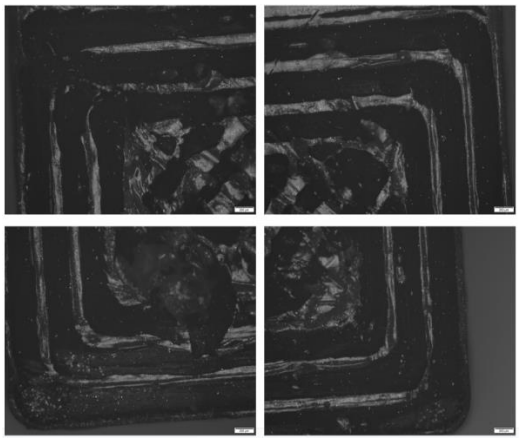

Figure 97 - Composed image of the fracture region in sample P_bp.

4.4. Case study

The image displayed in Figure 98 showcases the printed case. The printing process of the base and the cover was met with several challenges. Successive clogging and buckling were observed, which occurred either during the filament switch or closer to the end of the process. The parametrization used was optimized, considering previous results for similar parts. However, the use of TPU and CB/TPU still posed frequent risks of failure due to the filament's tendency to buckle in the gears. To mitigate this limitation, it is recommended using these filaments for printing small parts with shorter printing times. While this may not completely eradicate the possibility of errors, it may help reduce the number of instances it occurs.

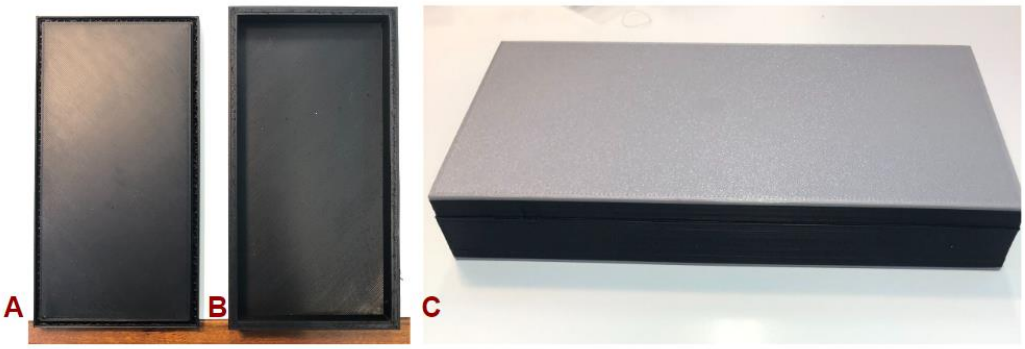

Figure 98 - EMI shielding case: A – Cover; B – Base; C - Assembly.

The case was fitted with a mobile phone and successfully received six incoming calls. Additionally, a Bluetooth headphone was able to connect to the phone. The experiment ultimately failed due to potential issues with the frequency bands used (LTE: 0.7-3.5 GHz). It is unclear what level of attenuation the printed case provided. Furthermore, the surface quality of the FFF may not have allowed for proper insulation, with the lack of a closed surface between the case and cover contributing to the failure. Finally, the design may not have been optimal, as the wall thickness of the solid and honeycomb regions of CB/TPU may not have provided sufficient reflection of electromagnetic waves.

5. Conclusions

The FTIR spectra analysis shows that both TPU and CB/TPU filaments have similar chemical compositions. However, the CB/TPU filament shows noticeable shifts in absorption bands associated with carboxyl and (C-O-C) groups due to interactions with the conductive filler. These results suggest that the TPU filaments used in this study may have had some imperfections, specifically in the case of the CB/TPU filament. It is important to consider the potential impact of filament quality on the outcome of the research.

Achieving successful TPU printing requires meticulous attention to nozzle calibration and material handling. Utilizing a nozzle with good conditions, along with proper calibration and implementing cleaning filaments between prints, proved essential in preventing nozzle clogging issues. Precise first layer calibration is crucial for ensuring smooth extrusion and preventing filament buckling, particularly with flexible materials like TPU. It is recommended to avoid uninterrupted overuse of CB/TPU in FFF printing and alternate the use of different material filaments for cleaning the extrusion path to maintain optimal printing conditions and prevent sediment buildup that can impede filament flow. These observations highlight the significance of fine-tuning printing parameters and implementing appropriate maintenance practices to optimize TPU printing performance and ensure consistent, high-quality results.

Based on the optical microscopy and SEM analysis, it can be concluded that the quality of the interface region between the two different feedstock filaments is good and there are no adherence difficulties. The multi-material sample presents the same quality as the samples composed of only one material, indicating good adhesion between the two filaments. Additionally, the surface appearance of CB/TPU and natural TPU was seen to be different, with CB/TPU being rougher and presenting CB aggregates and natural TPU being smoother while presenting dispersed particles, possibly additives or contaminants.

The study revealed that the TPU-CB/TPU multi-material parts possess mechanical properties that fall in between those of natural TPU and CB/TPU samples. This suggests that there is a balance between strength and rigidity. The inclusion of conductive filler in TPU led to a decrease in mechanical properties when compared to natural TPU, which is likely attributed to the concentration of filler required for electrical conductivity.

The interface region of the multi-material samples exhibited significant strength and deformation, indicating that the specific filaments work together to facilitate strong mechanical adhesion (6.65 MPa average maximum stress and average maximum strain of 8.97). The stress-strain curves of the samples from the parametric study were similar to those of the standard sample, indicating comparable mechanical responses. Previous studies have shown that nozzle temperature and infill speed are critical factors in achieving optimal printing quality and mechanical properties, which was also observed in this study. The effects on performance were less significant for bed temperature and filament retraction, likely because

the values tested were far from optimal. In conclusion, the multi-material TPU-CB/TPU parts demonstrated promising mechanical integrity, suggesting their potential suitability for various engineering applications.

6. Future Work

Considering the case study, the product was specifically designed to provide protection against electromagnetic radiation that is emitted by other phones and Bluetooth devices. However, due to several reasons that are outlined in chapter 4.4, the wanted level of protection was not achieved. Therefore, it is recommended to conduct specific electromagnetic tests in future works to test the range of attenuation of the case. To facilitate this, collaboration between the mechanical and electronics departments of the faculty of engineering could be initiated.

Apart from this, to determine the optimal wall thickness for EMI SE for the CB/TPU filament used in this thesis, further studies could be conducted. Furthermore, it would be beneficial to investigate the optimal thickness of the Honeycomb layers of CB/TPU to attenuate electromagnetic waves.

Even though a satisfactory printing calibration was achieved in this study for the filaments used, it would be interesting to optimize this calibration through a more detailed parametric study. It is recommended to produce at least three samples of each configuration to provide a more robust data foundation. Moreover, a cross-study could be conducted using the ANOVA method and Taguchi method to analyze the data.

Bibliography

Abilgaziyev, A., Kulzhan, T., Raissov, N., Hazrat Ali, M., Ko, W. L., & Mir-Nasiri, N. (n.d.). *Design and Development of Multi-Nozzle Extrusion System for 3D Printer*.

Arifvianto, B., Nur Iman, T., Tulung Prayoga, B., Dharmastiti, R., Agus Salim, U., & Mahardika, M. (n.d.). *Tensile properties of the FFF-processed thermoplastic polyurethane (TPU) elastomer*. https://doi.org/10.1007/s00170-021-07712-0/Published

Arifvianto, B., Satiti, B. E., Salim, U. A., Suyitno, Nuryanti, A., & Mahardika, M. (2022). Mechanical properties of the FFF sandwich-structured parts made of PLA/TPU multi-material. *Progress in Additive Manufacturing*, *7*(6), 1213–1223. https://doi.org/10.1007/s40964-022-00295-6

Balderrama-Armendariz, C. O., MacDonald, E., Espalin, D., Cortes-Saenz, D., Wicker, R., & Maldonado-Macias, A. (2018). Torsion analysis of the anisotropic behavior of FDM technology. *International Journal of Advanced Manufacturing Technology*, *96*(1–4), 307–317. https://doi.org/10.1007/s00170-018-1602-0

Bates, S. R. G., Farrow, I. R., & Trask, R. S. (2016). 3D printed polyurethane honeycombs for repeated tailored energy absorption. *Materials and Design*, *112*, 172–183. https://doi.org/10.1016/j.matdes.2016.08.062

Bates, S. R. G., Farrow, I. R., & Trask, R. S. (2019). Compressive behaviour of 3D printed thermoplastic polyurethane honeycombs with graded densities. *Materials and Design*, *162*, 130–142. https://doi.org/10.1016/j.matdes.2018.11.019

Bertolini, M. C., Dul, S., Barra, G. M. O., & Pegoretti, A. (2021). Poly(vinylidene fluoride)/thermoplastic polyurethane flexible and 3D printable conductive composites. *Journal of Applied Polymer Science*, *138*(17). https://doi.org/10.1002/app.50305

Bertolini, M. C., Dul, S., Lopes Pereira, E. C., Soares, B. G., Barra, G. M. O., & Pegoretti, A. (2021). Fabrication and characterization of piezoresistive flexible pressure sensors based on poly(vinylidene fluoride)/thermoplastic polyurethane filled with carbon black-polypyrrole. *Polymer Composites*, *42*(12), 6621–6634. https://doi.org/10.1002/pc.26327

Bhardwaj, T., Jain, P., & Singh, D. (2021). Experimental study on dimensional accuracy of freeform fabricated thermoplastic polyurethane. *IOP Conference Series: Materials Science and Engineering*, *1136*(1), 012060. https://doi.org/10.1088/1757-899x/1136/1/012060

Binder, L., Rackl, S., Scholz, M., & Hartmann, M. (2022). Linking Thermal Images with 3D Models for FFF Printing. *Procedia Computer Science*, *217*, 1168–1177. https://doi.org/10.1016/j.procs.2022.12.315

Brancewicz-Steinmetz, E., Sawicki, J., & Byczkowska, P. (2021). The influence of 3d printing parameters on adhesion between polylactic acid (Pla) and thermoplastic polyurethane (tpu). *Materials*, *14*(21). https://doi.org/10.3390/ma14216464

Bruère, V. M., Lion, A., Holtmannspötter, J., & Johlitz, M. (2023). The influence of printing parameters on the mechanical properties of 3D printed TPU-based elastomers. *Progress in Additive Manufacturing*, *8*(4), 693–701. https://doi.org/10.1007/s40964-023-00418-7

Candal, M. V., Calafel, I., Fernández, M., Aranburu, N., Aguirresarobe, R. H., Gerrica-Echevarria, G., Santamaría, A., & Müller, A. J. (2021). Study of the interlayer adhesion and warping during material extrusion-based additive manufacturing of a carbon nanotube/biobased thermoplastic polyurethane nanocomposite. *Polymer*, *224*. https://doi.org/10.1016/j.polymer.2021.123734

Chen, T., Xie, Y., Wang, Z., Lou, J., Liu, D., Xu, R., Cui, Z., Li, S., Panahi-Sarmad, M., & Xiao, X. (2021). Recent Advances of Flexible Strain Sensors Based on Conductive Fillers and Thermoplastic Polyurethane Matrixes. *ACS Applied Polymer Materials*, *3*(11), 5317–5338. https://doi.org/10.1021/acsapm.1c00840

Cheung, T. C., & Choi, S. Y. (2023). Evaluation of the influence of three-dimensional printing conditions on peel resistance and surface roughness of flexible polymer-textile composites. *Textile Research Journal*, *93*(7–8), 1531–1550. https://doi.org/10.1177/00405175221133841

de León, A. S., Domínguez-Calvo, A., & Molina, S. I. (2019). Materials with enhanced adhesive properties based on acrylonitrile-butadiene-styrene (ABS)/thermoplastic polyurethane (TPU) blends for fused filament fabrication (FFF). *Materials and Design*, *182*. https://doi.org/10.1016/j.matdes.2019.108044

Deng, X., Zeng, Z., Peng, B., Yan, S., & Ke, W. (2018). Mechanical properties optimization of poly-ether-ether-ketone via fused deposition modeling. *Materials*, *11*(2). https://doi.org/10.3390/ma11020216

Deng, Y. W., Yu, T. L., & Ho, C. H. (1994). Effect of Aging under Strain on the Physical Properties of Polyester-Urethane Elastomer. In *Polymer Journal* (Vol. 26, Issue 12).

Desai, S. M., Sonawane, R. Y., & More, A. P. (2023). Thermoplastic polyurethane for three-dimensional printing applications: A review. In *Polymers for Advanced Technologies* (Vol. 34, Issue 7, pp. 2061–2082). John Wiley and Sons Ltd. https://doi.org/10.1002/pat.6041

Duty, C., Ajinjeru, C., Kishore, V., Compton, B., Hmeidat, N., Chen, X., Liu, P., Hassen, A. A., Lindahl, J., & Kunc, V. (2018). What makes a material printable? A viscoelastic model for extrusion-based 3D printing of polymers. *Journal of Manufacturing Processes*, *35*, 526–537. https://doi.org/10.1016/j.jmapro.2018.08.008

Ecco, L. G., Dul, S., Schmitz, D. P., Barra, G. M. de O., Soares, B. G., Fambri, L., & Pegoretti, A. (2018). Rapid prototyping of efficient electromagnetic interference shielding polymer composites via fused deposition modeling. *Applied Sciences (Switzerland)*, *9*(1). https://doi.org/10.3390/app9010037

Ermolai, V., Sover, A., Boca, M. A., Hriţuc, A., Slătineanu, L., Nagîţ, G., & Stavarache, R. C. (2022). Mechanical Behaviour of Macroscopic Interfaces for 3D Printed Multi-material Samples. *MATEC Web of Conferences*, *368*, 01004. https://doi.org/10.1051/matecconf/202236801004

Freund, R., Watschke, H., Heubach, J., & Vietor, T. (2019). Determination of influencing factors on interface strength of additively manufactured multi-material parts by material extrusion. *Applied Sciences (Switzerland)*, *9*(9). https://doi.org/10.3390/app9091782

García-Collado, A., Blanco, J. M., Gupta, M. K., & Dorado-Vicente, R. (2022). Advances in polymers based Multi-Material Additive-Manufacturing Techniques: State-of-art review on properties and applications. In *Additive Manufacturing* (Vol. 50). Elsevier B.V. https://doi.org/10.1016/j.addma.2021.102577

Garg, N., Rastogi, V., & Kumar, P. (2022). Process parameter optimization on the dimensional accuracy of additive manufacture Thermoplastic Polyurethane (TPU) using RSM. *Materials Today: Proceedings*, *62*, 94–99. https://doi.org/10.1016/j.matpr.2022.02.309

Gumus, O. Y., Ilhan, R., & Canli, B. E. (2022a). Effect of Printing Temperature on Mechanical and Viscoelastic Properties of Ultra-flexible Thermoplastic Polyurethane in Material Extrusion Additive Manufacturing. *Journal of Materials Engineering and Performance*, *31*(5), 3679–3687. https://doi.org/10.1007/s11665-021-06510-9

Gumus, O. Y., Ilhan, R., & Canli, B. E. (2022b). Effect of Printing Temperature on Mechanical and Viscoelastic Properties of Ultra-flexible Thermoplastic Polyurethane in Material Extrusion Additive Manufacturing. *Journal of Materials Engineering and Performance*, *31*(5), 3679–3687. https://doi.org/10.1007/s11665-021-06510-9

Halim, K. A. A., Tee, H. W., Badrul, F., Salleh, M. A. A. M., Osman, A. F., Omar, Mohd. F., & Zakaria, M. S. (2024). The effect of compatibiliser on the mechanical properties and electrical properties of polypropylene/carbon black (PP/CB) conductive polymer composites (CPCs). *Materials Today: Proceedings*. https://doi.org/10.1016/j.matpr.2024.01.015

Harris, C. G., Jursik, N. J. S., Rochefort, W. E., & Walker, T. W. (2019). Additive Manufacturing With Soft TPU – Adhesion Strength in Multimaterial Flexible Joints. *Frontiers in Mechanical Engineering*, *5*. https://doi.org/10.3389/fmech.2019.00037

Haryńska, A., Carayon, I., Kosmela, P., Brillowska-Dąbrowska, A., Łapiński, M., Kucińska-Lipka, J., & Janik, H. (2020). Processing of polyester-urethane filament and characterization of fff 3d printed elastic porous structures with potential in cancellous bone tissue engineering. *Materials*, *13*(19), 1–22. https://doi.org/10.3390/ma13194457

Hohimer, C., Christ, J., Aliheidari, N., Mo, C., & Ameli, A. (2017). 3D printed thermoplastic polyurethane with isotropic material properties. *Proc.SPIE*, *10165*, 1016511. https://doi.org/10.1117/12.2259810

Islam, I., Sultana, S., Kumer Ray, S., Parvin Nur, H., Hossain, Md., & Md. Ajmotgir, W. (2018). Electrical and Tensile Properties of Carbon Black Reinforced Polyvinyl Chloride Conductive Composites. *C*, *4*(1), 15. https://doi.org/10.3390/c4010015

Jung, I., & Lee, S. (2023). Three-dimensional printed re-entrant strain sensor using various carbon types/thermoplastic polyurethane filaments. *Textile Research Journal*. https://doi.org/10.1177/00405175231213998

Kasmi, S., Ginoux, G., Labbé, E., & Alix, S. (2022). Multi-physics properties of thermoplastic polyurethane at various fused filament fabrication parameters. *Rapid Prototyping Journal*, *28*(5), 895–906. https://doi.org/10.1108/RPJ-08-2021-0214

Kasprzyk, P., & Datta, J. (2018). Effect of molar ratio [NCO]/[OH] groups during prepolymer chains extending step on the morphology and selected mechanical properties of final bio-based thermoplastic poly(ether-urethane) materials. *Polymer Engineering and Science*, *58*, E199–E206. https://doi.org/10.1002/pen.24874

Kechagias, J. D., Vidakis, N., & Petousis, M. (2021). Parameter effects and process modeling of FFF-TPU mechanical response. *Materials and Manufacturing Processes*. https://doi.org/10.1080/10426914.2021.2001523

Khan, M. A., Winowlin, J. T., & Editors, J. (n.d.). *Innovations in Additive Manufacturing Springer Tracts in Additive Manufacturing*. https://link.springer.com/bookseries/16694

Kim, N. P. (2020). 3D-printed conductive carbon-infused thermoplastic polyurethane. *Polymers*, *12*(6). https://doi.org/10.3390/POLYM12061224

Krishnanand, Soni, S., & Taufik, M. (2020). Design and assembly of fused filament fabrication (FFF) 3D printers. *Materials Today: Proceedings*, *46*, 5233–5241. https://doi.org/10.1016/j.matpr.2020.08.627

Laur, V., Maalouf, A., Chevalier, A., & Comblet, F. (2021). Three-Dimensional Printing of Honeycomb Microwave Absorbers: Feasibility and Innovative Multiscale Topologies. *IEEE Transactions on Electromagnetic Compatibility*, *63*(2), 390–397. https://doi.org/10.1109/TEMC.2020.3006328

Lee, Y.-H., Kang, B.-K., Kim, H.-D., Yoo, H.-J., Kim, J.-S., Huh, J.-H., Jung, Y.-J., & Lee, D.-J. (2009). Effect of Hot Pressing/Melt Mixing on the Properties of Thermoplastic Polyurethane. In *Macromolecular Research* (Vol. 17, Issue 8).

Li, W., Xu, L., Zhang, X., Gong, Y., Ying, Y., Yu, J., Zheng, J., Qiao, L., & Che, S. (2020). Investigating the effect of honeycomb structure composite on microwave absorption properties. *Composites Communications*, *19*, 182–188. https://doi.org/10.1016/j.coco.2020.04.003

Lin, X., Coates, P., Hebda, M., Wang, R., Lu, Y., & Zhang, L. (2020). Experimental analysis of the tensile property of FFF-printed elastomers. *Polymer Testing*, *90*. https://doi.org/10.1016/j.polymertesting.2020.106687

Loh, G. H., Pei, E., Gonzalez-Gutierrez, J., & Monzón, M. (2020). An overview of material extrusion troubleshooting. In *Applied Sciences (Switzerland)* (Vol. 10, Issue 14). MDPI AG. https://doi.org/10.3390/app10144776

Lopes, L. R., Silva, A. F., & Carneiro, O. S. (2018). Multi-material 3D printing: The relevance of materials affinity on the boundary interface performance. *Additive Manufacturing*, *23*, 45–52. https://doi.org/10.1016/j.addma.2018.06.027

Lv, Q., Tao, X., Shi, S., Li, Y., & Chen, N. (2022). From materials to components: 3D-printed architected honeycombs toward high-performance and tunable electromagnetic interference shielding. *Composites Part B: Engineering*, *230*. https://doi.org/10.1016/j.compositesb.2021.109500

Manganiello, C., Naso, D., Cupertino, F., Fiume, O., & Percoco, G. (2019). Investigating the potential of commercial-grade carbon black-filled TPU for the 3D printing of compressive sensors. *Micromachines*, *10*(1). https://doi.org/10.3390/mi10010046

Nace, S. E., Tiernan, J., Holland, D., & Ni Annaidh, A. (2021). A comparative analysis of the compression characteristics of a thermoplastic polyurethane 3D printed in four infill patterns for comfort applications. *Rapid Prototyping Journal*, *27*(11), 24–36. https://doi.org/10.1108/RPJ-07-2020-0155

Nijdam, J. J., Agarwal, D., & Schon, B. S. (2022). An experimental assessment of filament-extrusion models used in slicer software for 3D food-printing applications. *Journal of Food Engineering*, *317*. https://doi.org/10.1016/j.jfoodeng.2021.110711

Nordin Mohamad Norani, M., Ilman Hakimi Chua Abdullah, M., Fadzli Bin Abdollah, M., Amiruddin, H., Redza Ramli, F., Tamaldin, N., Kejuruteraan Mekanikal, F., Teknikal Malaysia Melaka, U., Tuah Jaya, H., Tunggal, D., & Teknologi Kejuruteraan Mekanikal dan Pembuatan, F. (2021). Mechanical and tribological properties of FFF 3D-printed polymers: A brief review. In *Jurnal Tribologi* (Vol. 29).

Petcharoen, K., & Sirivat, A. (2013). Electrostrictive properties of thermoplastic polyurethane elastomer: Effects of urethane type and soft-hard segment composition. *Current Applied Physics*, *13*(6), 1119–1127. https://doi.org/10.1016/j.cap.2013.03.005

Pivar, M., Gregor-Svetec, D., & Muck, D. (2022). Effect of printing process parameters on the shape transformation capability of 3D printed structures. *Polymers*, *14*(1). https://doi.org/10.3390/polym14010117

Pratama, J., Cahyono, S. I., Suyitno, S., Muflikhun, M. A., Salim, U. A., Mahardika, M., & Arifvianto, B. (2021). A review on reinforcement methods for polymeric materials processed using fused filament fabrication (Fff). In *Polymers* (Vol. 13, Issue 22). MDPI. https://doi.org/10.3390/polym13224022

Rathaur, A. S., Patel, V. K., & Katiyar, J. K. (2020). Tribo-mechanical properties of graphite/talc modified polymer composite bearing balls. *Materials Research Express*, *7*(1). https://doi.org/10.1088/2053-1591/ab58db

Ren, H., Yang, X., Wang, Z., Xu, X., Wang, R., Ge, Q., & Xiong, Y. (2022). Smart structures with embedded flexible sensors fabricated by fused deposition modeling-based multimaterial 3D printing. *International Journal of Smart and Nano Materials*, *13*(3), 447–464. https://doi.org/10.1080/19475411.2022.2095454

Ribeiro, M., Sousa Carneiro, O., & Ferreira da Silva, A. (2019). Interface geometries in 3D multi-material prints by fused filament fabrication. *Rapid Prototyping Journal*, *25*(1), 38–46. https://doi.org/10.1108/RPJ-05-2017-0107

Rodríguez, L., Naya, G., & Bienvenido, R. (2021). Study for the selection of 3D printing parameters for the design of TPU products. *IOP Conference Series: Materials Science and Engineering*, *1193*(1), 012035. https://doi.org/10.1088/1757-899X/1193/1/012035

Sable, P. A., Neel, C. H., & Borg, J. P. (2020). Dynamic strength and friction behavior of thermosetting polyurethane and epoxy. *AIP Conference Proceedings*, *2272*. https://doi.org/10.1063/12.0001029

Schmitz, D. P., Dul, S., Ramoa, S. D. A. S., Soares, B. G., Barra, G. M. O., & Pegoretti, A. (2021). Effect of printing parameters on the electromagnetic shielding efficiency of ABS/carbonaceous-filler composites manufactured via filament fused fabrication. *Journal of Manufacturing Processes*, *65*, 12–19. https://doi.org/10.1016/j.jmapro.2021.02.051

Schmitz, D. P., Ecco, L. G., Dul, S., Pereira, E. C. L., Soares, B. G., Barra, G. M. O., & Pegoretti, A. (2018). Electromagnetic interference shielding effectiveness of ABS carbon-based composites manufactured via fused deposition modelling. *Materials Today Communications*, *15*, 70–80. https://doi.org/10.1016/j.mtcomm.2018.02.034

Schmitz, D. P., Soares, B. G., Barra, G. M. O., & Santana, L. (2023). Sandwich structures based on fused filament fabrication 3D-printed polylactic acid honeycomb and poly(vinylidene fluoride) nanocomposites for microwave absorbing applications. *Polymer Composites*, *44*(4), 2250–2261. https://doi.org/10.1002/pc.27240

Theiler, G., Wachtendorf, V., Elert, A., & Weidner, S. (2018). Effects of UV radiation on the friction behavior of thermoplastic polyurethanes. *Polymer Testing*, *70*, 467–473. https://doi.org/10.1016/j.polymertesting.2018.08.006

Tian, Q., Krakovský, I., Yan, G., Bai, L., Liu, J., Sun, G., Rosta, L., Chen, B., & Almásy, L. (2016). Microstructure changes in polyester polyurethane upon thermal and humid aging. *Polymers*, *8*(5). https://doi.org/10.3390/polym8050197

Tvergaard, V., & Needleman, A. (n.d.). *Analysis of the Charpy V-notch test for welds*. www.elsevier.com/locate/engfracmech

Wang, H., Aubuchon, S. R., Thompson, D. G., Osborn, J. C., Marsh, A. L., Nichols, W. R., Schoonover, J. R., & Palmer, R. A. (2002). Temperature-dependent dynamic mechanical analysis-Fourier transform infrared study of a poly(ester urethane) copolymer. *Macromolecules*, *35*(23), 8794–8801. https://doi.org/10.1021/ma012135a

Xiao, J., & Gao, Y. (2017). The manufacture of 3D printing of medical grade TPU. *Progress in Additive Manufacturing*, *2*(3), 117–123. https://doi.org/10.1007/s40964-017-0023-1

Yilgor, I., Yilgor, E., Guler, I. G., Ward, T. C., & Wilkes, G. L. (2006). FTIR investigation of the influence of diisocyanate symmetry on the morphology development in model segmented polyurethanes. *Polymer*, *47*(11), 4105–4114. https://doi.org/10.1016/j.polymer.2006.02.027